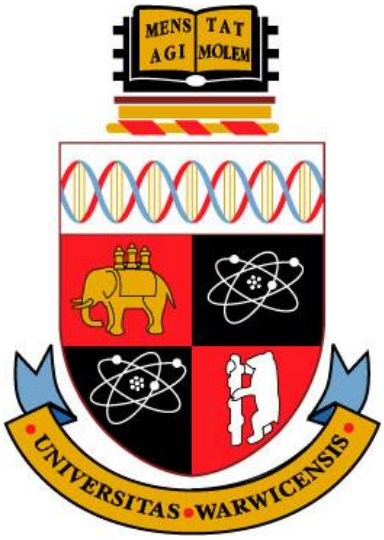

Development of Electrochemical Methods for the Determination of Pharmaceutical Impurities

Robert Barry Channon

A thesis submitted for the degree of Doctor of Philosophy

Department of Chemistry

September 2015

To my wonderful wife and parents

Table of Contents

Acknowledgments

Firstly, I would like to acknowledge my supervisor Prof. Julie Macpherson. That I have progressed from a bundle of wayward ideas and directionless enthusiasm into the scientist I am today is largely due to your patience, encouragement, criticism and guidance – thank you.

I am grateful to Element Six for providing me with top-notch diamond to investigate and to the EPSRC and AstraZeneca for funding my PhD, in particular to Tony Bristow and Andy Ray: You have always made me feel very welcome in Macclesfield and our 'duck meetings' were always enlightening and inspiring.

I have been lucky to work with many gifted scientists on different projects - Laura, James, Mark, Eleni, Max, Jon, Liz and Sophie. I would especially like to single out Jon Newland; we have been through something spending years together working on hydrazine, I don't know what, but definitely something!

Many thanks go to the Warwick Electrochemistry Group members past and present. I feel very privileged to have rubbed shoulders with many intellects and eccentric characters. Particular mention must go to the members of A105 especially James, Laura, Liz, Tania, Jenny, Zoë and Sophie; your friendship and our scientific or often not-so-scientific discussions have been a lifeline these past four years.

I am very fortunate to have such supportive family and friends who have kept me sane, happy and motivated all these years. Mum and Dad, I could never have made it this far in life or achieved this document without your constant support, love and encouragement – thank you always. Cat, you are my rock: Thank you for putting up with my scientific ramblings these past four years, feeding and clothing me throughout the generation of this document and picking me up each time I felt like throwing in the towel.

List of Figures

List of Tables

Declaration

The work contained in this thesis is my own original work except where outlined below. I confirm that this thesis has not been submitted for a degree at any other university.

The AFM images in chapter 3 (Figure 3.2) and the photographs of the BDD, flow cell, reference and counter electrodes and tubing in chapter 4 (Figure 4.8) were taken by Jon Newland (Electrochemistry and Interfaces Group, University of Warwick). The flow cells used in chapter 4 and 5 were fabricated by Frank Courtney (School of Engineering, University of Warwick). The illustration of MEMED (Figure 5.17) was created with assistance from Liz Oseland (Electrochemistry and Interfaces Group, University of Warwick) and all FE-SEM images in chapter 2 and 5 (Figure 2.4, 5.7) were recorded with assistance from Lingcong Meng (Electrochemistry and Interfaces Group, University of Warwick). Finally, the microfluidic mould used for microfluidics chip fabrication, and the Au sputtered bands described in chapter 5 were fabricated by Jon Newland.

Parts of this thesis have been published as detailed below:

R. B. Channon, J. C. Newland, A. W. T. Bristow, A. D. Ray, and J. V. Macpherson, *Selective detection of hydrazine in the presence of excess electrochemically active pharmaceutical ingredients, using Boron Doped Diamond Metal Nanoparticle Functionalised Electrodes*, *Electroanalysis*, **2013**, 25 (12), 2613–2619.

R. B. Channon, M. B. Joseph, E. Bitziou, A. W. T. Bristow, A. D. Ray and J. V. Macpherson, *Electrochemical Flow Injection Analysis of Hydrazine in an Excess of an Active Pharmaceutical Ingredient: Achieving Pharmaceutical Detection Limits Electrochemically, Anal. Chem.*, 2015, 87 (19), 10064–10071

Also, all finite element modelling in the following work was conducted by myself, as a side project:

L. A. Hutton, J. G. Iacobini, E. Bitziou, R. B. Channon, M. E. Newton, and J. V. Macpherson, *Examination of the Factors Affecting the Electrochemical Performance of Oxygen Terminated Polycrystalline Boron Doped Diamond Electrodes, Anal. Chem.*, **2013**, 85(15), 7230–7240

Abstract

This thesis is concerned with the development of electrochemical approaches for the determination of carcinogenic genotoxic impurities in pharmaceuticals. Investigations focus on the genotoxic impurity hydrazine as it is a particularly challenging species for current methodologies used in the pharmaceutical industry.

A metal nanoparticle functionalised polycrystalline boron-doped diamond macroelectrode is utilised for hydrazine determination in stationary solution, in the presence of two important electrochemically active, inner sphere, active pharmaceutical ingredients, namely acetaminophen and promazine. It is shown that this sensor can be tuned for the application by simply changing the chemical identity of the nanoparticles.

A new design of flow cell for flow injection analysis is then developed, in order to exploit a hydrodynamic approach for the electrochemical determination of genotoxic impurities. The bespoke flow cell is combined with an inlaid boron doped diamond microband electrode and the flow injection analysis response is analysed numerically and against various models of dispersion to demonstrate the quality of the method.

Finally, this flow injection analysis sensor is employed for the trace detection of hydrazine in a large excess of acetaminophen. Quantitation is demonstrated down to 0.274 parts per millions with respect to the amount of acetaminophen - surpassing the required safe guidelines set by the pharmaceutical industry for the quantitation of genotoxic impurities.

Abbreviations

ACM	Acetaminophen
AFM	Atomic force microscopy
API	Active pharmaceutical ingredient
BDD	Boron doped diamond
CAD	Computer-aided design
CE	Capillary electrophoresis
CLND	Chemiluminescent nitrogen detection
CNT	Carbon nanotube
CPE	Carbon paste electrode
CV	Cyclic voltammetry / voltammogram
CVD	Chemical vapour deposition
CZE	Capillary zone electrophoresis
DPV	Differential pulse voltammetry / voltammogram
EC	Electrochemical detection
ET	Electron transfer
FIA	Flow injection analysis
GC	Gas chromatography
GCE	Glassy carbon electrode
GI	Genotoxic impurity
HILIC	Hydrophilic interaction chromatography
HPLC	High pressure liquid chromatography
HZ	Hydrazine
IC	Ion chromatography
ID	Inner diameter
IHP	Inner Helmholtz plane
IPD	Indirect photometric detection
ITO	Indium tin oxide
LLE	Liquid-liquid extraction
LOD	Limit of detection
MEKC	Micellar electrokinetic chromatography

MEMED	Microelectrochemical measurements at expanding droplets
MOF	Metal organic frameworks
MS	Mass spectrometry
MSL	Microsteriolithography
MWCNT	Multiwall carbon nanotubes
NDC	Non-diamond carbon
NP	Nanoparticle
OD	Outer diameter
OHP	Outer Helmholtz plane
PDMS	Polydimethylsulphoxide
PEEK	Polyetheretherketone
ppm	Parts per million
PTFE	Polytetrafluoroethylene (Teflon)
PZ	Promazine
RDE	Rotating disk electrode
RDS	Rate determining step
SCE	Saturated calomel electrode
SEM	Scanning electron microscopy
SWV	Square wave voltammetry
TEM	Transmission electron microscopy
TLC	Thin layer chromatography
XRD	X-ray diffraction

Glossary of Symbols

$\bar{\mu}$	Mean of background response (for LOD)
$2b$	Channel height
A	Electrode area
a	(a) Electrode radii
	(b) Radii of a tube
	(c) Activity
A'	Cross sectional area
C	Concentration
C*	Bulk concentration
C^0	Initial plug concentration (FIA)
C_D	Double layer capacitance
C^{max}	Maximum plug concentration at peak signal (FIA)
Cs	Surface concentration
D	Diffusion coefficient
D_c	Dispersion coefficient
D_h	Hydraulic diameter
D_{ox}	Diffusion coefficient of oxidised species
D_{red}	Diffusion coefficient of reduced species
E	Potential
E^0	Standard electrode potential
E^0'	Formal Potential
$E_{1/2}$	Half wave potential
E_f	(a) Fermi level
	(b) Final potential (CV)
E_p	Peak potential
E_{pa}	Anodic peak potential
E_{pc}	Cathodic peak potential
E_s	Starting potential (CV)
F	Faradays constant
H_{ads}	Hydrogen adsorption peak

H_{des}	Hydrogen desorption peak
i	Current
i_{lim}	Limiting current (steady state current)
i_p	Peak current
j	Flux
k_0	Standard rate constant
k_b	Rate constant for oxidation
k_f	Rate constant for reduction
k_r	Electron transfer coefficient
k_t	Mass transport coefficient
l	Length of a channel flow cell
l_e	Entry length in a channel flow cell
n	Number of electrons
O	Oxidised form of a species
P_e	Peclet number
Q	Charge
R	Reduced form of a species
R	(a) Molar gas constant
	(b) Resistance of a solution
r	Radial coordinate
Re	Reynolds number
R_S	Solution resistance
$SD_{baseline}$	Standard deviation of baseline (FIA)
T	Temperature
t	Time
$\bar{U}$	Mean fluid velocity
u_0	Maximum velocity at centre of channel (FIA)
u_z	Velocity at a channel height of z in a flow cell
V_f	Flow rate
v_x	Velocity in the 'x' direction
w	Channel width
x	Distance along electrode in direction of flow (FIA)
x_e	Band electrode width
z	(a) Charge on a species

	(b) Co-ordinate in channel height direction (FIA)
δ	Diffusion layer thickness
Δi	Differential current
η	Overpotential
κ	(a) Conductivity
	(b) Inverse double layer thickness
ν	Scan rate
ν'	Kinematic viscosity
σ	(a) DPV constant
	(b) Background variance of a blank injection in FIA
τ	Time before potential step (DPV)
τ'	End of potential step time (DPV)
τ_d	Dimensionless time (FIA)
φ	Rotational co-ordinate

Chapter 1 Introduction

1.1 Overview

This thesis explores the application of electrochemical analysis for the determination of the pharmaceutical impurity hydrazine (HZ). Several approaches are investigated with an aim to develop versatile electrochemical methods for trace level detection of HZ in aqueous and non-aqueous solvents and in the presence of an excess of an active pharmaceutical ingredient (API). This chapter introduces the key themes of the work and explores the main experimental tools namely voltammetry, boron doped diamond (BDD) and flow injection analysis (FIA).

1.2 Analytical Approaches for the Determination of Pharmaceuticals

From drug discovery right through to post-launch surveillance, it is critical to be able to assess the safety, quality and efficacy of new medicines. This could involve pharmacokinetic modelling in drug design,[1] dissolution studies of polymorphs of an API[2] or the discovery of the importance of drug chirality through tragedy's like thalidomide.[3] Therefore, analytical science is critical in supporting drug design and manufacture. Furthermore this field is constantly developing as industry and academic researchers strive to make new, faster, cheaper, cleaner, simpler and smaller methods with better sensitivity, lower detection limits and simpler output.[4]

1.2.1 Genotoxic Impurities

Genotoxic impurities (GIs) are carcinogenic or mutagenic compounds which modify DNA and are therefore harmful to human health.[5] A variety of chemicals exhibit genotoxic

activity and are classified according to key functional groups, resulting in a list of structural alerts as shown in Figure 1.1.

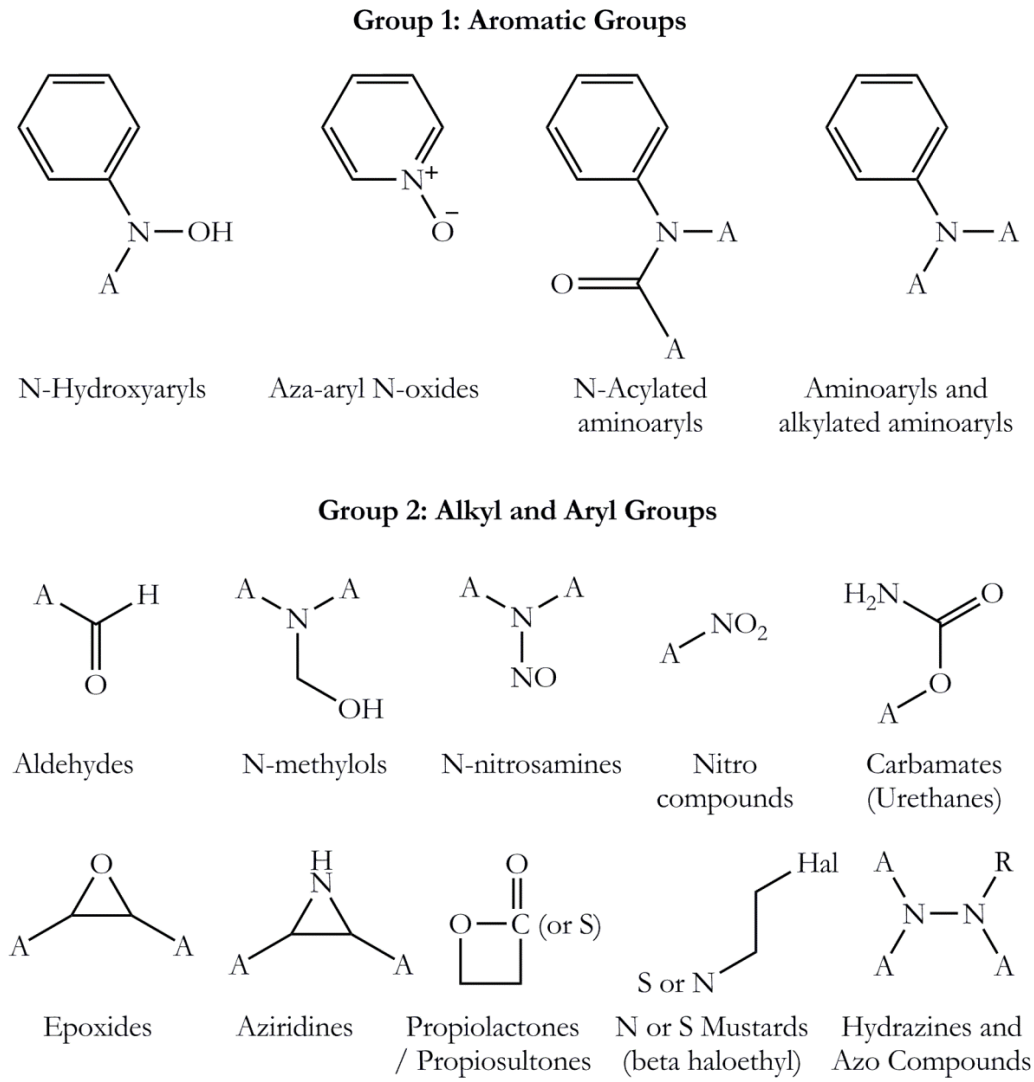

Figure 1.1: Structural alerts for GIs.[6]

In a pharmaceutical process, GIs can be starting materials, intermediates, reaction by-products or degradation products from the API.[7] Typically, the API and any expected or observed impurities are checked against the structural alerts in Figure 1.1. They are then classified into known mutagens and carcinogens (class 1), mutagens that may be carcinogens (class 2), species with possible mutagenicity or carcinogenicity based on the structural alert (class 3), species with alerting structures closely related to the API (class 4 and species with no alerting structure (class 5).[6] Class 5 requires no testing and class 4 often is tested through normal API testing procedures. Class 2 and 3 require testing for carcinogenicity, which is carried out via the Ames test, involving a bacterial mutation assay with Salmonella typheimurium and Escherichia coli.[8,9]

When a GI is discovered, usually either i) the synthesis is altered to avoid the GI, or ii) process parameters are adjusted to reduce the amount of GI. If neither are successful and the GI cannot be removed to safe levels, the process is scrapped.[5] Clearly quantification of the GI is important, both to understand where and how it occurs as well as to what levels. The safe exposure levels of GIs are rigorously controlled and the most common approach is the threshold of toxicological concern (TTC)[6] as shown in Table 1.1.

Duration of exposure / months	≤1	1-3	3-6	6-12	>12
Allowable daily intake (μg/day)	120	40	20	10	1.5

Table 1.1: Threshold of toxicological concern - safe levels of GI contact based on the exposure period.[6]

The most stringent limits (i.e. for long term exposure) have a threshold of 1.5 μg/day. This equates to roughly 1 part per million (ppm), relative to the API as given in equation 1.1.

$$ppm = \frac{\text{mass GI (mg)}}{\text{mass API (kg)}} \tag{1.1}$$

Depending on the GI and system, a wide variety of analytical approaches are used to quantify the GIs: Gas chromatography – mass spectrometry (GC-MS) is common, particularly for alkyl halides, sulfonate esters and chloroformates.[10] Separation approaches such as High pressure liquid chromatography (HPLC) are also very common (usually employing UV, MS or electrochemical detection – EC), especially for epoxides, N-nitroso and aromatic amines.[10] There are however a vast number of alternate methods employed such as ion chromatography (IC), capillary electrophoresis (CE), thin layer chromatography (TLC), micellar electrokinetic chromatography (MEKC), hydrophilic interaction chromatography (HILIC), EC and capillary zone electrophoresis (CZE) as well as hybrid's such as HPLC-MS.[9] The vast number of methods is clearly advantageous in that for any GI, there will always be a documented method that can be used. Conversely, this means often several expensive (to buy and or run) pieces of equipment with trained technicians are required to regulate GI levels in pharmaceutical drug development effectively.

Depending on the occurrence of the GI in the process (e.g. as a starting material or degradation of the final product), quantification is required in often complex media i.e. containing starting materials, intermediates, an excess of the target molecule, various solvents, stabilisers etc. In order to simplify detection, the GI is sometimes separated from the matrix via liquid-liquid extraction (LLE).[11] This takes advantage of the different solubility of species in different media to separate the GI. Furthermore, some GIs are not ideally amenable to detection using common detection techniques for example; due to a small molecular weight (MS) or lack of chromophore (for UV detection). Here derivatization can be employed whereby the GI is reacted with another species yielding a product that is much easier to detect than the original GI.[12]

One drawback several methods suffer is that of on/off-line detection. On-line detection involves detection in or by the reaction vessel and allows for real-time quantitation of the GI as it is formed / consumed, thus allowing in-situ detection or removal of the GI. This also avoids the issue of quenching the reaction and the possibility that GI levels may change between generation and measurement. However, many of the aforementioned methods are not applicable or easy to adapt to on-line analysis.

1.2.2 Strategies for Hydrazine

HZ and its derivatives are well documented mutagens and carcinogens.[13] Despite its toxicity, HZ is also a very useful chemical, for example as a reducing agent,[14-16] pharmaceutical precursor[17,18] and as a direct liquid fuel cell.[19] HZ is particularly difficult to quantify due to its high volatility, high polarity, low molecular weight and lack of chromophore, which is exacerbated in the presence of non-volatile, high-molecular weight APIs.[20] A wide variety of techniques have been evaluated for HZ quantitation,[9] as shown in Table 1.2, with the resulting limits of detection (LOD) displayed in ppm versus the amount of API present.

Technique	Application	Derivatization	LOD / ppm	Ref.
GC-MS	Analysis with API	acetone-d6	0.03[a]	21
HPLC-LLE	Analysis in a range of excipients	benzaldehyde	0.04[b]	22
HPLC	Analysis in hydralazine	benzaldehyde	0.27[b]	23
GLC	Analysis in hydralazine and isoniazid	benzaldehyde	3	24
Fluorimetric detection	Analysis in isoniazid formulations	2-hydroxy-1-naphthaldehyde	6.4	25
Fluorescence detection	Analysis in water, plasma and isoniazid	3,6-diacetoxyfluoran	2340	26

CE-IPD	Analysis with API	n/a	2	[27]
CE-EC	Analysis in a range of excipients	n/a	29	[28]
IC-EC	Analysis with API	n/a	50	[29]
HILIC-CLND	Analysis with API	n/a	200	[30]
CE-EC	Analysis in a range of excipients	n/a	233	[31]

Table 1.2: Example methods for HZ detection in the presence of APIs, LOD's are quoted with respect to mass of API, IPD: indirect photometric detection and CLND: chemiluminescent nitrogen detection. [a]Based on quoted limit of quantitation. [b]Smallest ppm of HZ detected for a range of batches of different APIs.

Derivatization is often employed in the HZ analysis process with derivatizing agents such as such as acetone[21] or benzaldehyde[22-24] to enable detection. However, the yields of the derivatization reaction are varied (~85-95%), leading to uncertainty in the amount of HZ present. LLE is also employed to aid quantitation, sometimes in addition to derivatization.[22] Many of the methods shown in Table 1.2 require long analysis times, high cost of instrumentation and are difficult to operate in-line which adds to the overall cost of drug development. Furthermore, many of these approaches do not reach the optimum TTC LOD (~1 ppm). Clearly, none of these methods are optimal for HZ detection in the presence of an excess of API and there is certainly scope for new inexpensive, on-line, simple, quick and adaptive methods.

1.3 Electrochemical Analysis

Electrochemistry is a 200 year old discipline† which in its origins entailed the electrolysis of water (Nickolson and Carlisle), the amalgamation of static, magnetic and voltaic electricity as one force (Faraday) and the re-animation of a dead frog (Galvani).[32,33]

†Some definitions indicate 400 years,[34] whilst others suggest 2265 years as a better estimate.[35]

In its modern form, electrochemistry is a wide ranging discipline involved with for example; battery technologies,[36] solar cells,[37] glucose monitors for diabetes,[38] fuel cells,[39] supercapacitors[40] and pH sensors[41] to name but a few. One area which receives considerable attention is electrochemical analysis. In comparison to other analytical techniques, electrochemical sensors are typically fast, cheap, capable of low level detection and high sensitivity as well as being easily adaptable for on line analysis.

1.3.1 Dynamic Electrochemistry

Consider a simple one electron redox reaction of a species between its reduced R and oxidised O form,

$$\mathrm{R} \underset{k_\mathrm{b}}{\overset{k_\mathrm{f}}{\rightleftharpoons}} \mathrm{O} + ne^- \tag{1.2}$$

where k_f is the forward rate constant and k_b is the backward rate constant. With no external driving force, the forward (reduction) and backward (oxidation) reactions occur at the same rate and the species are at equilibrium.[42] In this case the forward and backwards rate constants are equal i.e.

$$k_\mathrm{f} = k_\mathrm{b} = k^0 \tag{1.3}$$

where k^0 (cm s^{-1}) is the standard rate constant and represents the kinetic facility of the redox couple to undergo electron transfer (ET) at the electrode-solution interface. In dynamic electrochemistry, we perturb this equilibrium by application of energy in the form of an applied potential, thus driving the reaction in one direction and simultaneously measuring the resulting transfer of electrons in the form of a faradaic current. For a more detailed description of electrochemical kinetics, refer to the Butler-Volmer model.[42]

1.3.1.1 Three Electrode Electrolytic Cells

A standard, three-electrode, electrolytic cell is formed of the following basic components: working electrode, reference electrode, counter electrode, potentiostat and solution which usually contains solvent, redox active species and background electrolyte. This cell is illustrated in Figure 1.2.

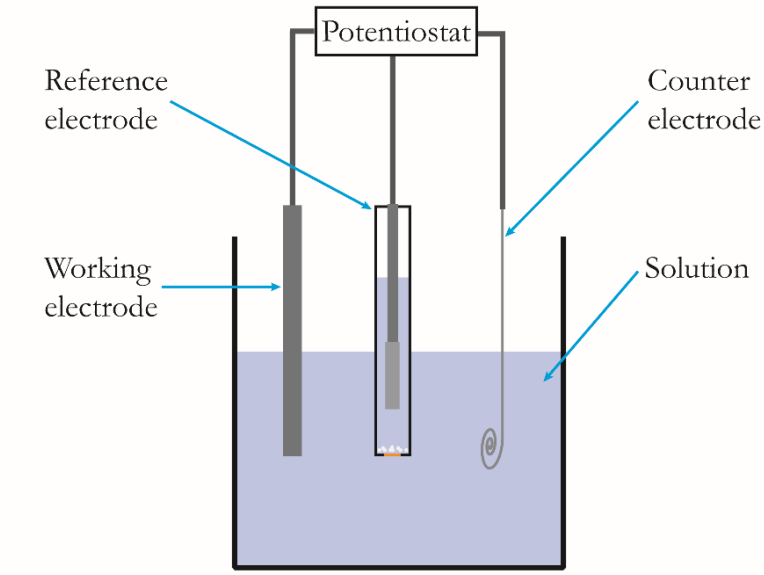

Figure 1.2: Illustration of a typical three electrode electrolytic cell.

Let us consider the components. The potentiostat acts as the power source for the process. A potential is applied between the working and reference electrodes in order to drive an electrochemical reaction at the surface of the working electrode, resulting in a current (i). The potentiostat then applies a current of equal size and opposite magnitude ($-i$) to the counter electrode, such that the current flow in the cell occurs between the working and counter electrodes.[42]

The working electrode, particularity its surface, is the key component of an electrochemical cell. The electrode material, geometry, pretreatment, history, even crystalline facet can have a dramatic effect on the electrochemical response.[43] Commonly, metal or carbon based electrodes are utilised, however a wide variety of materials have

been employed depending on the nature of the experiment. Similarly, whilst disk shaped electrodes are common, a range of sizes (from macro to nanoelectrodes)[44] and shapes (disk, hemisphere, band, ring etc.)[45] are employed.

The reference electrode serves to maintain a constant potential irrespective of the solution conditions. To appreciate this, let us consider a general reaction of the form,

$$\mathrm{aA} + \mathrm{bB} \rightleftharpoons \mathrm{cC} + \mathrm{dD} \tag{1.4}$$

where a is the number of moles of species A and so on. The Nernst equation, which describes the electrode potential with respect to the solution conditions is then given by,[42]

$$E = E^0 - \frac{RT}{nF} ln \left(\frac{a(\mathrm{C})^{\mathrm{c}}.a(\mathrm{D})^{\mathrm{d}}}{a(\mathrm{A})^{\mathrm{a}}.a(\mathrm{B})^{\mathrm{b}}} \right) \tag{1.5}$$

where E^0 is the standard rate constant, R (J K^{-1} mol^{-1}) is the molar gas constant, T (K) is the temperature, n is the number of electrons transferred, F is Faradays constant (96495 C mol^{-1}) and a is the activity of the substance, given by,

$$a = \gamma C \tag{1.6}$$

where γ is the activity coefficient and C is the concentration. E^0 (V) represents the intrinsic thermodynamic potential of the corresponding redox couple and occurs at k^0 (equation 1.3). For convenience, the E^0 and the γ of all species are often combined into a new constant known as the formal potential, $E^{0'}$, such that the Nernst equation (equation 1.5) now becomes,[42]

$$E = E^{0'} + \frac{2.303RT}{nF} log \left(\frac{[\mathrm{A}]^a.[\mathrm{B}]^b}{[\mathrm{C}]^c.[\mathrm{D}]^d} \right) \tag{1.7}$$

where $E^{0'}$ is given by,

$$E^{0\prime} = E^{0} + \frac{RT}{nF} log\left(\frac{\gamma_A^a.\gamma_B^b}{\gamma_C^c.\gamma_D^d}\right) \quad (1.8)$$

Common reference electrodes include the metal/sparingly soluble metal halide system, such as silver/silver chloride (Ag/AgCl) and mercurous chloride (Hg/Hg_2Cl_2) also known as the saturated calomel electrode (SCE). For example, the Ag/AgCl reference electrode has cell equation and Nernst equation given by,

$$AgCl_{(s)} + e^{-} \rightleftharpoons Ag_{(s)} + Cl^{-}_{(aq)} \quad (1.9)$$

$$E = E^{0} + \frac{RT}{F} ln\left(\frac{a(Ag_{(s)}).a\left(Cl^{-}_{(aq)}\right)}{a(AgCl_{(s)})}\right) \quad (1.10)$$

where E^0, R and F are all constants and T is kept constant. All solids by definition have unit activity, therefore the potential of the electrode is only dependant on the activity of chloride ions. The Ag/AgCl reference electrode commonly comprises an Ag wire which is chlorodised to form a layer of AgCl on the surface. Often, the reference electrode is housed in a glass container containing an excess of chloride containing background electrolyte i.e. 3 M KCl and a ceramic frit. This allows the passage of current via a liquid-liquid junction as depicted in Figure 1.2 and maintains a constant chloride activity. The use of a membrane and reservoir of controlled chloride activity is however not always possible, depending on the constraints of the system, e.g. in microfluidics where electrode size and placement are critical factors. Under these conditions, often a Ag/AgCl wire is used; although AgCl is sparingly soluble the kinetics of dissolution are rapid enabling a pseudo constant chloride activity to be maintained at the electrode/electrolyte interface.[46] This electrode is often referred to as a quasi-reference electrode and small shifts (10 - 20 mV) in potential can be observed experimentally.[47]

Within electrochemical cells, there are often several resistances, *R*, present as a result of passing a current through the electrodes, wiring, through solution and through the electrode-solution interface. If a current is passed between the working and reference electrodes, an ohmic drop *(iR*) occurs whereby some of the applied potential is used to pass the current and thus the applied potential and the potential felt at the working electrode-solution interface are not equal. For this reason, high concentrations of inert salt (background electrolyte) are added to solution, to decrease the solution resistance (R_s) and/or a counter electrode added to the circuit so that no current passes through the reference electrode. Commonly, Pt wire or gauze counter electrodes are employed with a large surface area.

However, when the working electrode surface area is small (e.g. in the micron and smaller range) and/or the faradaic current passed is small (e.g. μA and smaller), *iR* is small and hence ohmic drop is negligible. In this case, the electrochemical cell can be operated in a two electrode setup (working and reference only), where the potential is applied and the current is measured between the working and reference electrodes.

1.3.1.2 Mass Transport

The faradaic current that passes in an electrochemical circuit is directly proportional to the rate of the reaction, expressed as a flux, *j*, as shown in equation 1.11.[42]

$$i = nAFj \tag{1.11}$$

where *n* is the number of electrons transferred in the faradaic process, *A* is the working electrode surface area (cm^{-2}) and *j* is the flux (mol cm^{-2} s^{-1}). *j* can be broken down into several processes as shown in Figure 1.3.

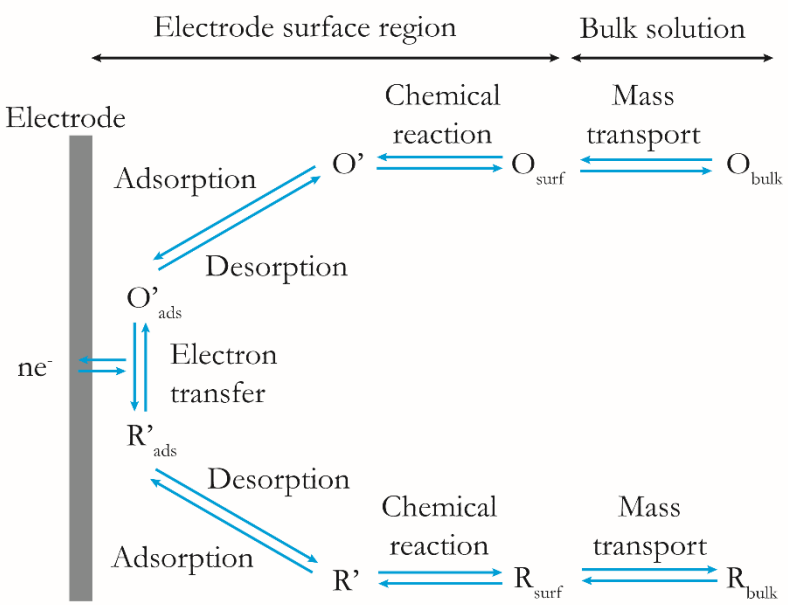

Figure 1.3: Illustration of heterogeneous ET and mass transport.[42]

Faradaic species reach the electrode surface by mass transport and then may undergo chemical reaction and or adsorption before transferring electrons at the working electrode surface. The rate constant which describes mass transport, the mass transport coefficient, is denoted k_t (cm s^{-1}) and that which describes ET is denoted the ET coefficient k_r (cm s^{-1}). Mass transport to the electrode surface can occur by one or a combination of diffusion, convection and migration.

1.3.1.3 Diffusion

Specifically, diffusion is the movement of species down a concentration gradient. When a redox reaction occurs at the surface of the working electrode, the surface concertation of the faradaic species *C*s is lowered compared to the bulk concentration *C**. Material then diffuses from bulk to the surface to balance this concentration gradient. Over time a diffusion layer δ develops as depicted in Figure 1.4, with steeper gradients and smaller δ observed for shorter timescales.

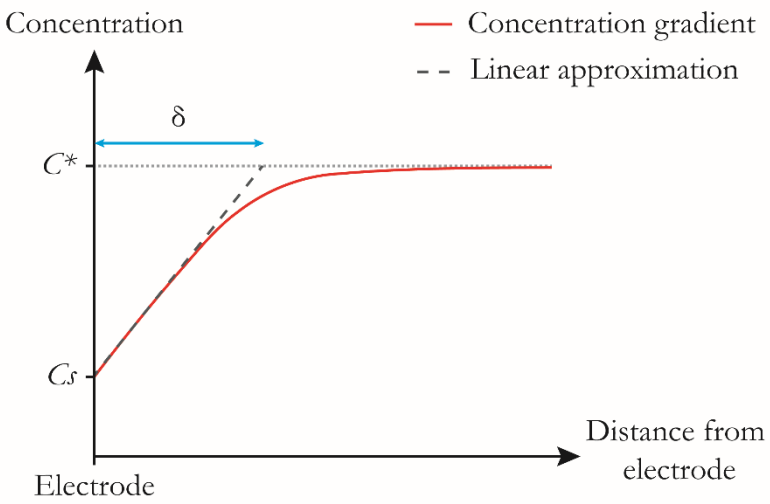

Figure 1.4: Diffusion layer near an electrode surface in 1D.

Fick's first law of diffusion states that for a diffusion controlled process, the flux of species is dependent on the concentration gradient as follows;[42]

$$j = -D\frac{\partial C^*}{\partial x} \tag{1.12}$$

for a one-dimensional system (x co-ordinate), where D is the diffusion coefficient ($cm^2\ s^{-1}$) and $\delta C^*/\delta x$ is the concentration gradient. It follows that,

$$j = -\frac{D}{\partial}C^* \tag{1.13}$$

where D/δ equates to k_t under diffusion-controlled reaction conditions i.e.

$$j = -k_t C^* \tag{1.14}$$

Fick's second law of diffusion states that diffusion at a point x, over time t is given by,

$$\frac{\partial C}{\partial t} = D\frac{\partial^2 C}{\partial x^2} \tag{1.15}$$

which for three-dimensional Cartesian coordinates is given by,

$$\frac{\partial C}{\partial t} = D\left(\frac{\partial^2 C}{\partial x^2} + \frac{\partial^2 C}{\partial y^2} + \frac{\partial^2 C}{\partial z^2}\right) \tag{1.16}$$

and for cylindrical coordinates is given by,

$$\frac{\partial C}{\partial t} = D\left(\frac{\partial^2 C}{\partial r^2} + \frac{1}{r}\frac{\partial C}{\partial \varphi} + \frac{\partial^2 C}{\partial x^2}\right) \tag{1.17}$$

where r is the radial coordinate and φ is the rotational coordinate.

If we apply a potential step from a potential where no reaction occurs, to one where a faradaic species is turned over at a diffusion-controlled rate, a diffusion field develops as depicted in Figure 1.4. This experiment is known as chronoamperometry (sometimes referred to as amperometry) and the resulting current is given by,[48]

$$i = \frac{nAFD^{1/2}C^*}{(\pi t)^{1/2}} \tag{1.18}$$

The resulting current-time transient is displayed in Figure 1.5.

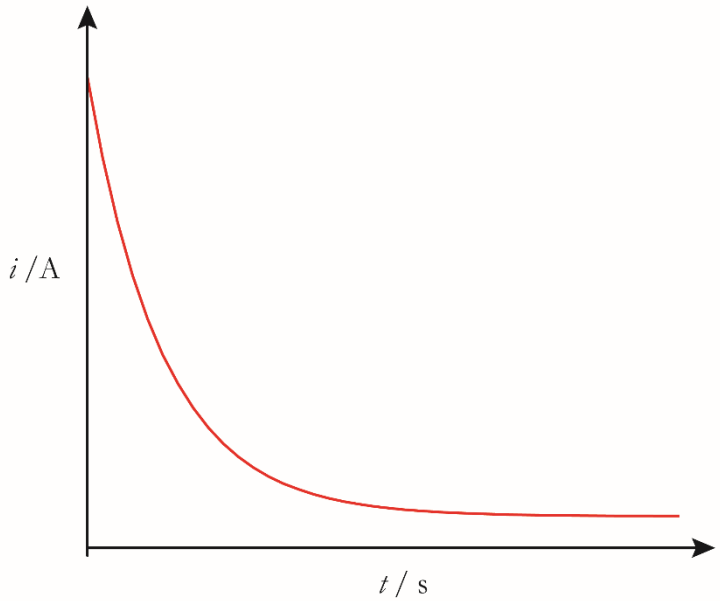

Figure 1.5: Current-time transient following a potential step.

In three dimensions, the diffusion fields that develop are dependent not only on the timescale of the experiment, but on the geometry of the electrode. At a macroelectrode

e.g. a 1 mm diameter disk electrode, linear diffusion prevails, where the diffusion fields lie normal to the electrode surface as shown in Figure 1.6a. In the case of microelectrodes – where the critical electrode dimension is μm in size or smaller, radial diffusion prevails, increasing the diffusional flux of species arriving at the electrode surface per unit time per unit area.

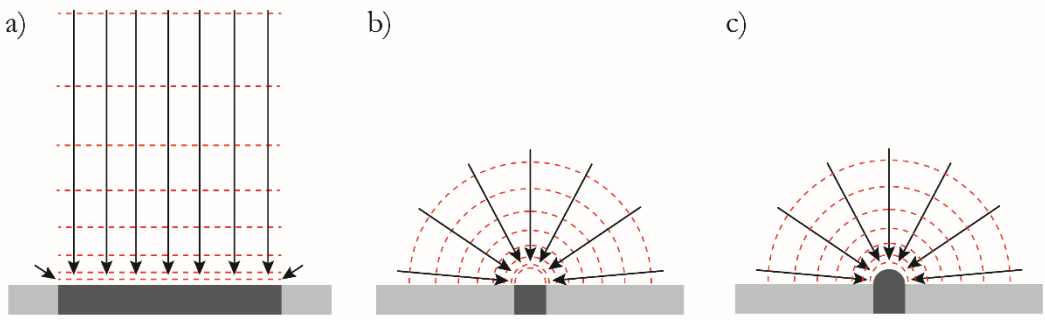

Figure 1.6: Diffusion profiles for a a) macroelectrode, b) microelectode and c) hemispherical electrode.

1.3.1.4 Convection and Migration

Convection is the movement of species due to a temperature, pressure or mechanical gradient and in one-dimension is described by,

$$j_x = v_x C^* \tag{1.19}$$

where j_x is the flux in the x direction and v_x is the velocity in the x direction. Experimentally, convection generally entails heating, stirring or flow of the solution and will be discussed in more detail in section 1.4.

Migration is the movement of a charged species under an electric field. In the case of a one-dimensional potential field, the flux is described by,

$$j_x = -\frac{zF}{RT} D C^* \frac{\partial \varphi}{\partial x} \tag{1.20}$$

where χ (C) is the charge on the species and $\delta\varphi/\delta x$ is the potential gradient. Equations 1.20, 1.19 and 1.12 may be combined into the Nernst-Planck equation, which describes one-dimensional mass transport to an electrode as,[42]

$$j_x = -D\frac{\partial C^*}{\partial x} - \frac{zF}{RT}DC^*\frac{\partial \varphi}{\partial x} + v_x C^* \tag{1.21}$$

where the three terms represent the diffusive, migratory and convective contributions to mass transport respectively.

Often, in order to simplify the mass transport experimentally such that it is easier to quantify, one or more of the terms of the Nernst-Planck equation are made negligible through experimental design. For example, the convective term can be nullified by maintaining room temperature and atmospheric pressure (1 ATM) throughout an experiment, whilst avoiding stirring or flowing the solution. Similarly, migratory effects can be avoided by the addition of an excess of an insert salt to solution, known as a background electrolyte. The background electrolyte (typically 0.1 M KNO_3 or KCl) is usually present at least 100 times the concentration of faradaic species and serves to increase conductivity in the solution and decrease the size of the diffuse layer at the electrode interface.[49] This is crucial as in order to reduce the problem to a purely diffusional one, the change in potential must be minimised to within the electron tunnelling distance (i.e. 10 – 20 Å).[48]

1.3.1.5 The Electrode-Solution Interface

A general model for the double layer as originally developed by Helmholtz,[50] then updated by Guoy, Chapman[51] and Graeme[52] is shown in Figure 1.7. Provided the electrode holds a charge, solvated (outer Helmholtz plane, *OHP*) and un-solvated (inner Helmholtz plane,

IHP) ions assemble at the electrode-solution interface to balance the charge. The double layer thickness ($1/\kappa$) at 25 °C is given by the following equation,[53]

$$\frac{1}{\kappa} = \frac{4.3\times10^{-8}}{\sqrt{(2I)}} \tag{1.22}$$

where the ionic strength *I,* for typical background electrolytes such as KNO_3 or KCl, is equivalent to *C**.

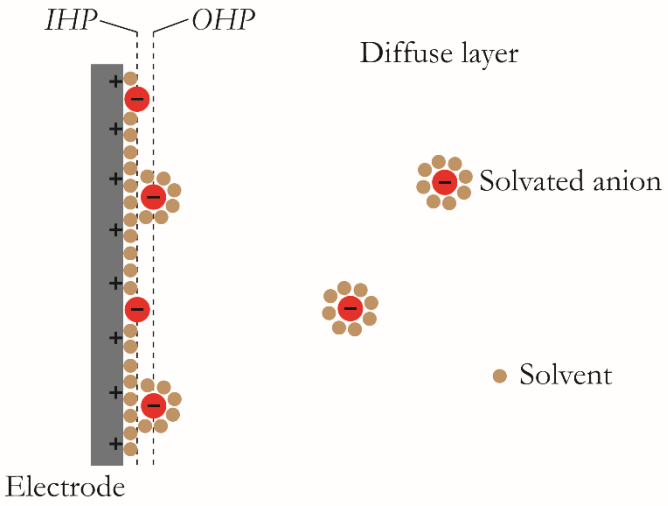

Figure 1.7: The electronic double layer at the electrode-solution interface for a positively charged electrode.

At high ion concentrations e.g. 0.1 M, the double layer is compact (i.e. 10 – 20 Å)[48] and the electric field extends only extends as far as the *OHP*, such that migratory effects on the faradaic species are negligible. Scanning or jumping the potential causes the charge distribution on the electrode surface to change and thus the double layer must adapt accordingly. This leads to a capacitive contribution to the current resulting in background currents independent of the faradaic species, which are exacerbated by fast scan rates and a large working electrode surface area. In chronoamperometric measurements, the capacitive current following a potential step is given by,[48]

$$i = \frac{E_F - E_S}{R_S} exp\left(\frac{-t}{R_S C_D}\right) \quad (1.23)$$

where E_F is the final potential, E_s is the starting potential and C_D is the double layer capacitance.

Transfer of electrons to/from faradaic species at the electrode/electrolyte interface can be classified as either inner or outer sphere based on how the species interacts with the electrode during ET.[48] An outer sphere species approaches to around the *OHP* at which point ET is undergone via electron tunnelling between the species and electrode. There is no direct interaction between the species and electrode, such that the ET is independent of the electrode material or surface. An inner sphere species directly interacts with the electrode surface via chemical reaction or adsorption during the ET, thus the ET is dependent on the electrode material or surface.[54] The two cases are depicted in Figure 1.8 below.

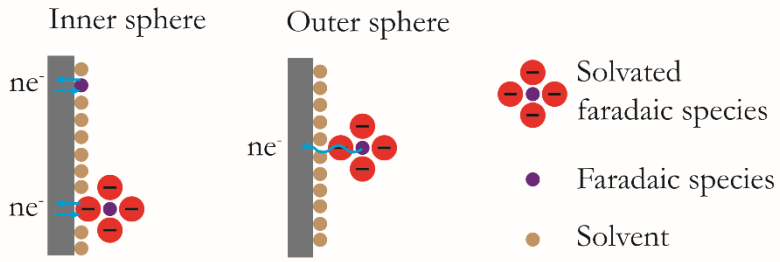

Figure 1.8: Illustration of inner and outer sphere ET.

1.3.1.6 Voltammetry

One of the most basic and common electrochemical techniques is cyclic voltammetry (CV).[48] The potential is typically scanned from a point where no ET occurs to a potential past $E^{0'}$, then reversed in direction at a defined potential scan speed (ν in V s^{-1}). By convention, this difference (E - $E^{0'}$) is known as the overpotential, η. The current, recorded as a function of the applied potential is illustrated in Figure 1.9 below for a one electron

oxidation process at a disk macroelectrode. Note, when the CV is stopped after the forward sweep, this technique is known as linear sweep voltammetry (LSV).

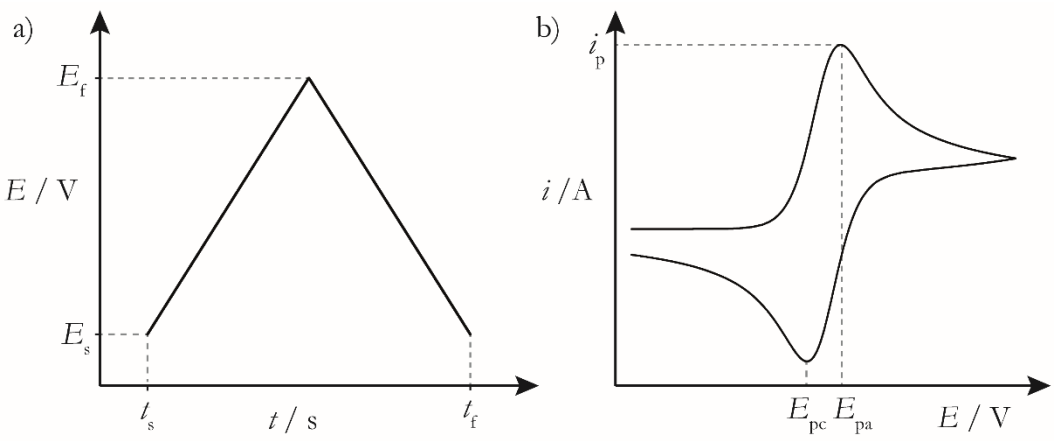

Figure 1.9: Cyclic voltammogram for an oxidation process at a disk macroelectrode with a) potential sweep and b) current response with time. The potential is swept from E_s to E_f, then back to E_s. E_{pa} and E_{pc} are the anodic and cathodic peak potentials respectively and i_p is the peak current for the forward sweep.

As the potential is increased, the current rises and species diffuse linearly from bulk (Figure 1.6a) down the concentration gradient (Figure 1.4) to the electrode surface. Eventually, the diffusion cannot keep up with the rate of surface ET and the current reaches a peak (i_p) at E_{pa} before decaying. On the reverse sweep, the previously generated oxidised species are reduced in a similar fashion, resulting in a reduction peak at $E_{pc.}$ i_p for a reversible (diffusion-controlled) process at T = 25 °C is given by the Randles Sevcik equation,[42]

$$i_p = 2.69 \times 10^5 n^{3/2} D^{1/2} C A v^{1/2} \quad (1.24)$$

where 2.69×10^5 is a constant containing F, T and R. These voltammograms are often characterised by their peak-peak potential (E_{pa} - E_{pc}), which for a one electron, reversible, diffusion limited ET is 59 mV.[55] Similarly, the half wave potential $E_{1/2}$ is often used in place of the $E^{0'}$ to describe the voltammogram i.e.[56]

$$E_{1/2} = E^{0'} + \frac{RT}{2nF} ln\left(\frac{D_{\text{red}}}{D_{\text{ox}}}\right) \tag{1.25}$$

where D_{red} and D_{ox} are the diffusion coefficients of the reduced and oxidised species respectively. Experimentally, $E_{1/2}$ is taken as the midpoint between the anodic and cathodic peaks.

For the case of a disk microelectrode (diameter ≤ 25 μm) operated under conditions where diffusion is the only form of mass transport to consider in the system, the current rises, then reaches a steady state before retracing the curve in the reverse sweep as shown in Figure 1.10. The steady state (not peaked) response occurs due to the hemispherical (not radial) diffusion (Figure 1.6b), i.e. k_t is large such that k_r is rate limiting and thus the current plateaus at high η.

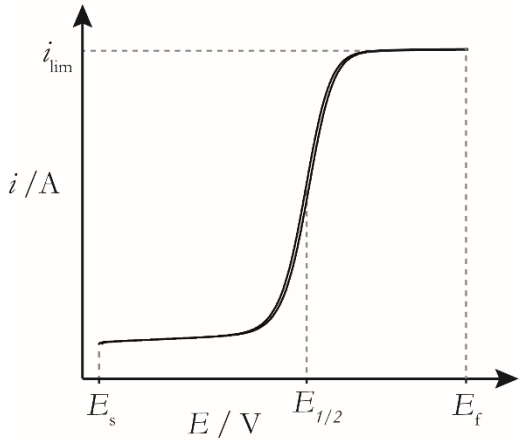

Figure 1.10: Cyclic voltammogram for an oxidation process at a disk microelectrode, where i_{lim} is the steady state (limiting) current.

The steady state current (also referred to as the limiting current, i_{lim}) is given by,

$$i_{\text{lim}} = 4nFDC^{*}a \tag{1.26}$$

where a is the radii of the microelectrode and $E_{1/2}$ is taken at half the i_{lim}.

For inner sphere species, $E_{1/2}$ is observed at different η, depending on the kinetic facility of the system (k^0). Slower kinetics e.g. from less kinetically active surfaces will lead to a shift of $E_{1/2}$ to higher η as well as a spreading out of the wave (*ca* large peak-peak for macroelectrodes).[57] k^o can be extracted using numerical simulations or finite element modelling, for example by the Nicholson method.[58]

1.3.1.7 Pulse Voltammetry

Another interesting approach is to scan the potential as a series of steps known as pulse voltammetry. The potential sweep method for a typical pulse voltammetry method - differential pulse voltammetry (DPV) is shown in Figure 1.11.[42]

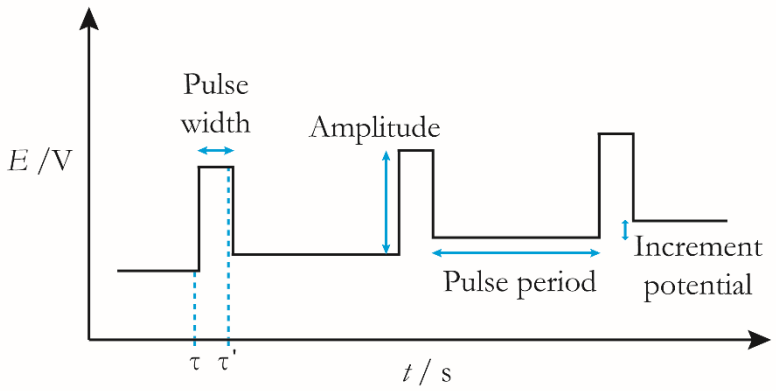

Figure 1.11: DPV potential staircase for an oxidation process.

Instead of constant current sampling as with CV, the current in DPV is sampled just before the start (τ) and at the end (τ') of a potential step i.e.

$$\Delta i = i_{\tau'} - i_{\tau} \tag{1.27}$$

where Δi is the differential current, $i_{\tau'}$ is the current at time τ' and i_{τ} is the current at time τ. The peak current is given by the following equation,[47]

$$\Delta i = \frac{nFAD^{1/2}C}{\pi^{1/2}(\tau'-\tau)^{1/2}}\left(\frac{1-\sigma}{1+\sigma}\right) \tag{1.28}$$

where σ is given by

$$\sigma = exp\left(\frac{nF\Delta E}{2RT}\right) \tag{1.29}$$

As described in equations 1.18 and 1.23, the faradaic and capacitive currents decay with an $i \propto t^{1/2}$ and $i \propto exp(-t)$ relationship respectively. Therefore, as the capacitive current decays much faster than the faradaic one, so long as the step size is large enough (>5 ms), the background capacitive contribution to the overall current is effectively quenched.[42,59] A typical differential pulse voltammogram (DPV) for an oxidation process is shown in Figure 1.12 with the corresponding LSV of the same system.

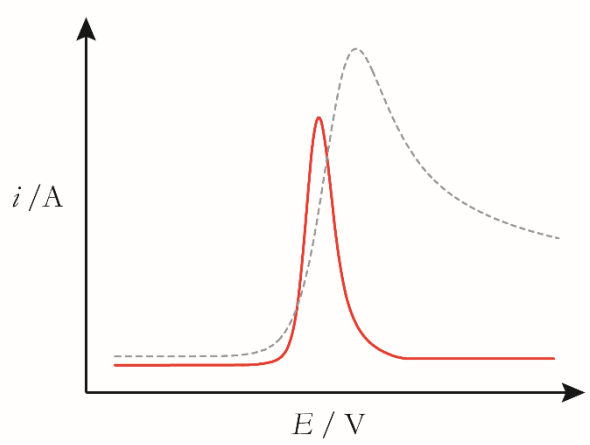

Figure 1.12: Current-potential plot for an oxidation via DPV (—) at a macorelectrode overlaid with the corresponding LSV (▪▪▪▪), currents for the two techniques are not to scale.

Note that the differential current is highest at the steepest upwards gradient of the LSV (around $E_{1/2}$) and drops to zero at the same potential as the peak current (i_p).

1.3.2 Boron Doped Diamond

Carbon materials are very popular choices for electrochemical sensors due to their ease of access, biocompatibility and useful properties based on the form.[60] Of all the many allotropes of carbon, diamond is probably the most extraordinary.[61] Diamond has a ordered face-centred-cubic lattice structure with extra atoms in the tetrahedral holes and

a density of 2×10^{23} carbon atoms per cm^3. It is incredibly hard (90 GPa), has a very high thermal conductivity (2000 W m^{-1} K^{-1}) and is a very strong electrical insulator with a 5.5 eV bandgap at 300 K.[61,62] In order to generate conductivity, diamond can be doped with boron (p-type dopant) or nitrogen (n-type dopant) though the former is more common due to its smaller activation energy (0.37 eV *vs* 1.7 eV). The introduction of boron into diamond creates an acceptor level 0.37 eV above the valence band as shown in Figure 1.13.

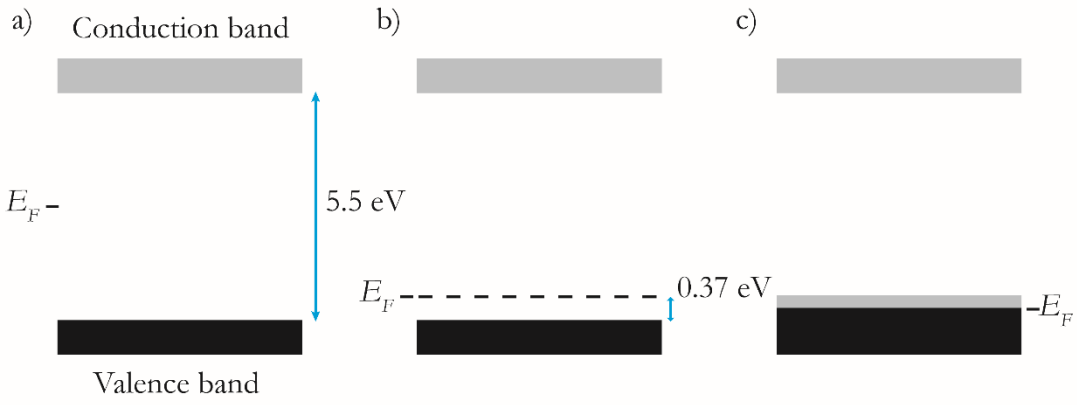

Figure 1.13: Energy level diagrams for a) intrinsic (un-doped), b) moderately doped and c) heavily doped BDD, where E_f is the fermi level.

At moderate doping levels (Figure 1.13b, ~1×10^{18} boron atoms per cm^3 i.e. 1/17000 atoms are boron), BDD is a p-type semiconductor, where the boron atoms accept electrons from the valence band leading to holes conducting in the valence band. At high doping levels (Figure 1.13c, ~ 10^{20} boron atoms per cm^3 i.e. roughly one in one thousand atoms are boron), these holes overlap resulting in a boron impurity band and quasi-metallic behaviour.[63,64] This doping is also characterised by a colour change from colourless through blue (semi-conducting) to black (metallic-like) with higher levels of doping.

Although there are several methods for synthetic diamond fabrication such as high pressure high temperature,[65] detonation synthesis[66] and cavitation,[67] chemical vapour deposition (CVD) is the most popular technique due to its high level of control over the

growth process and ability to grow large structured diamonds.[68] In short; a plasma is generated by either microwaves or a hot filament over a substrate such as silicon impregnated with diamond nanoparticles (NP). A gaseous carbon source such as methane is then added to the reactor with an excess of hydrogen gas and a boron source such as B_2H_6. The diamond sp^3 structure is then grown slowly atom by atom, leading to a polycrystalline wafer. The primary crystalline facets are 111, 110 and 100 which uptake boron to different degrees (Figure 1.14),[69] leading to a heterogeneously doped surface. Furthermore the diamond is initially hydrogen terminated at the surface, as a result of the hydrogen atmosphere during growth, but can be oxygen terminated either deliberately; using anodic polarisation[70] or alumina polishing,[71] or as a result of the electrode fabrication process leading to ketone, ester and hydroxyl functional groups at the surface.[72,73] Unlike metal electrodes where silver epoxy or solder can simply be used to contact to the electrode, BDD electrodes connected in this fashion frequently exhibit resistive voltammetry signatures. Therefore, an ohmic metal-carbide contact is often made to reduce ohmic drop effects.[68]

Depending on the growth conditions, BDD can be grown as an ultrananocrystal (grain size <10 nm) up to microcrystal (grain size up to 1 μm), thin film or even single crystal.[65,68] As shown in Figure 1.14, freestanding polished polycrystalline BDD wafers – of the type used within this thesis – have large grain sizes (~ 1 μm), and can be machined into different electrode geometries such as macrodisk electrodes.[74]

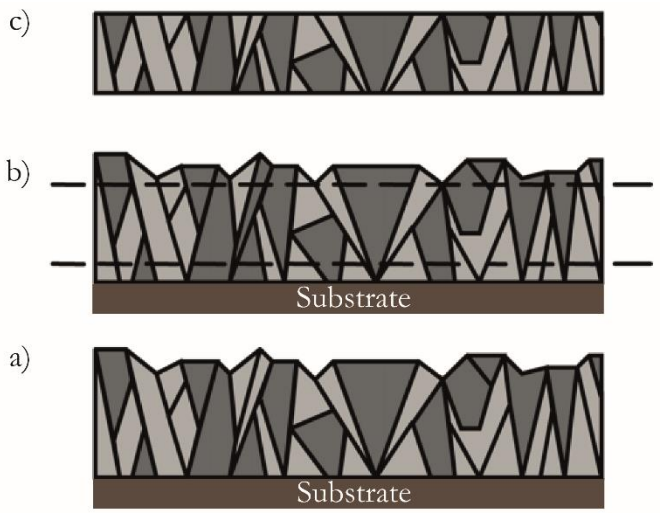

Figure 1.14: Schematic of BDD growth, with different boron uptake shown by different darkness of grains, a) structure after growth, b) processing / polishing and c) freestanding structure after polishing.[75]

1.3.2.1 Electrochemistry at Boron Doped Diamond Electrodes

As an electrode material, BDD has an sp^3 face-centred cubic type lattice structure, which results in a catalytically inactive surface and thus a high resistance to fouling, low background currents and slow ET kinetics towards inner sphere species.[71,76,77] For example, as shown in Figure 1.15,[74] the electrolysis of water (an inner sphere species) requires significantly greater electrode potentials at a BDD electrode compared to Pt (which has a much more electrocatalytically active surface).[74] This results in a very wide solvent window for BDD = 3.41 V, the widest of all electrode materials in aqueous solution. Note, the solvent window in this case was defined as the potential to reach a current density of 0.4 mA cm^{-3}, and taken from the forward sweeps in the cathodic and anodic directions.[68] The large solvent window and the low background currents simplify the interpretation of electrochemical signals and facilitate the trace detection of species. For example, the solvent window of Pt contains signals from oxygen and hydrogen adsorption / desorption, leading to a larger and more complex background response than BDD, as shown in Figure 1.15.

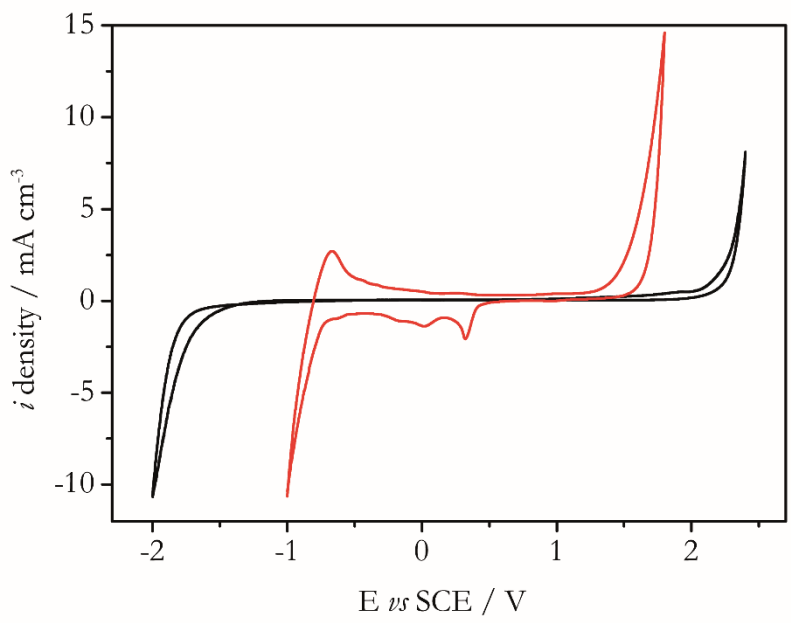

Figure 1.15: Solvent window for a 1 mm disk BDD macroelectrode (—) compared to a 2 mm disk Pt macroelectrode (—), in 0.1 M KNO_3, scan rate = 0.1 V s^{-1}, solvent windows are 3.41 V and 0.71 V respectively.

One important consideration is that the advantageous properties of BDD are highly dependent on the synthesis and processing.[71] For example, polycrystalline BDD often contains contain non-diamond carbon (NDC, e.g. sp^2 carbon) at grain boundaries between the different crystalline facets (Figure 1.14). This NDC is more catalytically active than diamond, resulting in smaller solvent windows and higher capacitance.[74] Also, NDC content is exacerbated by smaller crystalline grains or higher boron concentration and is usually quantified by Raman spectroscopy. Therefore, the use of BDD from freestanding polished polycrystalline wafers (i.e. large grain boundaries), coupled with acid cleaning to remove excess NDC in the fabrication procedure, leads to BDD electrodes with low NDC content.[71]

1.3.3 All-Diamond Electrodes

One of the final stages in BDD electrode fabrication is insulation of the electrode to expose only the required geometry. Freestanding BDD electrodes are typically either

sealed in glass or epoxy,[74] whereas thin film electrodes typically form the base of a cell which is clamped to the electrode to create a defined electrode area,[78] as shown in Figure 1.16 below.

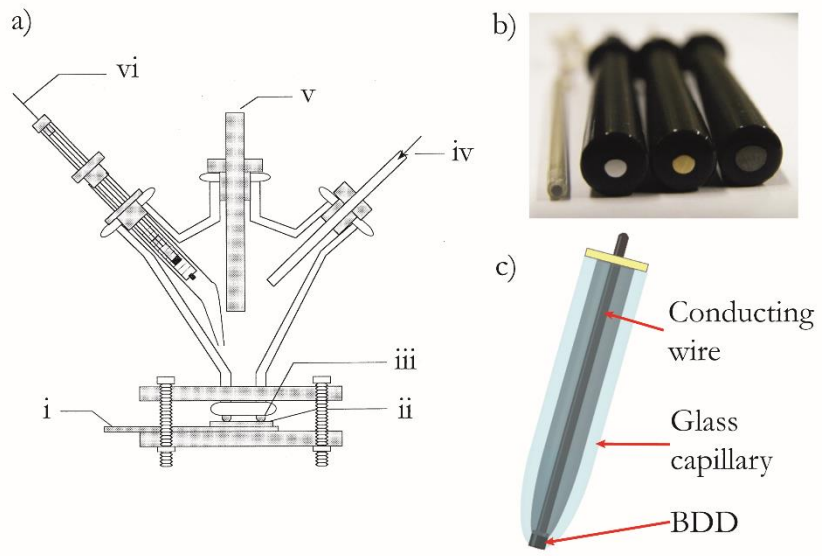

Figure 1.16: Illustrations of the typical electrode setup for a) thin film BDD,[78], where i) is a Cu or Al metal current collecting plate, ii) is the diamond film electrode, iii) is the O-ring seal, iv) is the input for nitrogen purge gas, v) is the carbon rod or Pt counter electrode and vi) is the reference electrode, b) freestanding BDD macroelectrode (left) beside Pt, Au and GC commercial macroelectrodes[74] and c) schematic of a freestanding BDD macroelectrode.[74]

However, neither approach is perfect: Firstly, for glass sealed electrodes, a typical cleaning method is polishing with an alumina slurry to clean off any impurities. However, as the insulating material will always polish at a faster rate than mechanically hard BDD, over time the sides of the BDD will become exposed, leading to larger electrochemical signals and a changing electrochemical response. This is also exacerbated when using BDD in harsh environments (e.g. organic solutions, strong pH's, high pressures / temperatures), as although the BDD may be stable to the conditions, the encapsulation material may not be! Secondly, electrochemical analysis requires precise control of the electrode geometry; changing electrode geometries or recessed / protruding structures can complicate analysis whether in a stationary or flow environment.[79] Thirdly, thin film electrodes are typically

difficult to polish experimentally and thus are usually used as grown, with a rough surface.[68] Thin film electrodes are also not applicable to acid cleaning as this can lead to delamination from the substrate.[71]

For these reasons it is beneficial to be able to fabricate controlled geometry BDD electrodes in a robust insulating substrate, with minimal offset between the electrode and substrate. Recent advancements in fabrication methodologies have facilitated the manufacture of high quality BDD microstructures, inlaid into insulating diamond as a surround.[45] This method allows the fabrication of bands, disks and ring disks as shown in Figure 1.17, with a minimum feature size of around 50 μm. Recently Silva *et al.*[80] also demonstrated the production of an all diamond micro-probe at the end of a tungsten wire with the same intention and a comparable fabrication approach.

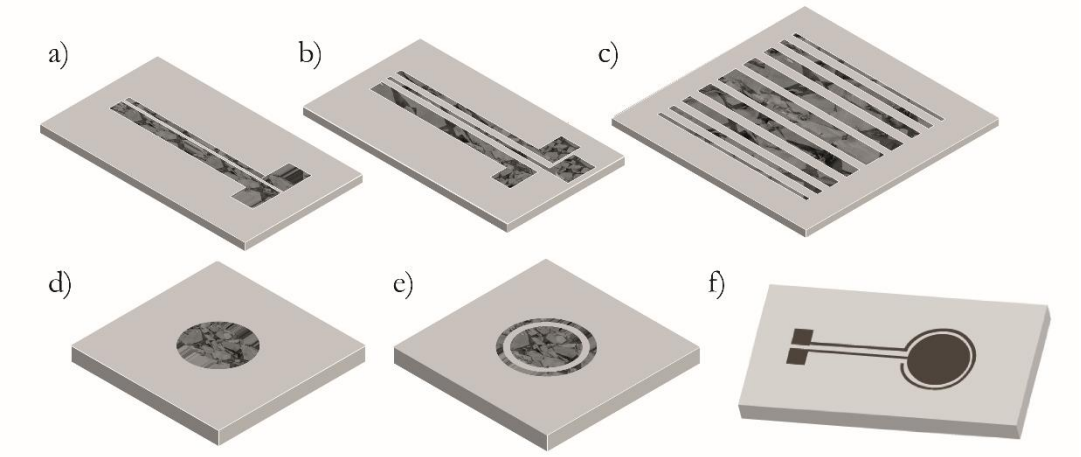

Figure 1.17: Schematic of all-diamond band (a-c), disk (d) and ring-disk (e-f) electrodes of various geometries.[45]

1.3.4 Nanoparticle Functionalised Electrodes

The functionalization of electrodes allows for the tuning of a sensor towards the application. For example, films are added to electrodes to shield the electrode from surface containments,[81] biomolecules are attached to electrodes for target molecule detection,[82] carbon nanotubes (CNT's) are added to electrodes to greatly enhance activity[83] and even

electrode surface termination can be altered to modify the electrochemical response.[84] NPs and general nanomaterials are of great interest to a wide range of fields from catalysis, to spectroscopy, to biosensors.[85-87] This interest stems from the fact that the properties of NPs are different and often superior to that of the corresponding bulk material.[88] The electrocatalytic properties of NPs are dependent on the shape, size, preparation method and history.[89]

Often the NPs are attached to a support which acts to provide a conductive contact as well as to limit aggregation. This also facilitates control over NP size and density. These supported NP electrodes are usually prepared by one of three methods: Firstly, the NP can be made by colloidal synthesis in solution before attachment to the support.[90] However, the NPs usually require stabilising in solution and robust attachment of the NP to the support is challenging. Secondly, metal ions can be immobilised onto the substrate before reduction to NPs on the surface.[91] However, this requires co-ordinating functional groups or films at the surface to stabilise the ions. Finally, NP supported electrodes can be fabricated by electrodeposition, whereby metal ions are reduced directly onto the metal surface.[74]

The latter method occurs in a two part process via nucleation (single metal atoms forming nuclei on the surface) and growth (reduction of metal ions onto the already formed nuclei). The main disadvantage of this method is that NPs can have a wide range of sizes due to progressive nucleation (new nuclei form whilst other are already growing) and Ostwald ripening.[89] However these effects can be overcome through control of the deposition parameters. The ideal support electrode is one that serves only to provide electrical contact to the metal NP but is itself electrochemically inactive towards the species of interest. Hence carbon based electrodes such as glassy carbon (GCE), screen printed carbon, CNT's and diamond are common.[74,92-94]

Aside from the reduced material costs, one big advantage of NP based electrodes is a high signal to noise ratio, particularly when using catalytically inactive supports such as BDD.[74] The background (capacitive, non-faradaic) currents scale with the active surface area of the working electrode. Hence a solid electrode will show a greater non faradaic contribution than one where the electrode component consists of 2D-arranged NPs. Additionally, over long timescales or with small inter-NP separations, the diffusion fields can overlap leading to similar faradaic signals to a corresponding-area bulk electrode as shown in Figure 1.18.

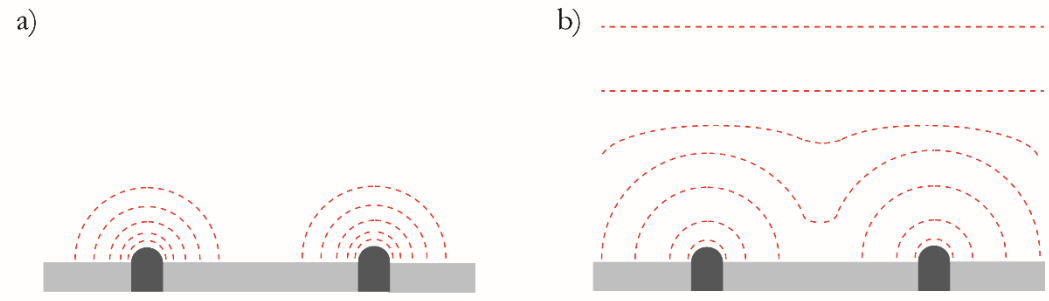

Figure 1.18: Diffusion fields at NP functionalised electrodes for a) short times and b) long times.

In order to confirm the size and density of NP-functionalised electrodes, they are often characterised by electrochemical and non-electrochemical methods.[89] Often with metal NPs, there are background peaks in any CV experiment caused by formation or stripping of metal oxides and metal hydrides at the NP surface. This is particularly prevalent for platinum, where the hydrogen desorption (H_{des}) and adsorption (H_{ads}) peaks are sometimes clear enough to differentiate different shapes or crystal facets using CV.[95]

Non-electrochemical techniques such as atomic force microscopy (AFM), scanning electron microscopy (SEM), X-ray diffraction (XRD) and transmission electron microscopy (TEM) are often use to determine the size, shape and density of the NP. However, the resolution of the technique can limit its effectiveness, particularly for small densely packed NPs. Also, for electrodes with heterogeneous NP density across the

electrode (e.g. heterogeneous surfaces such as polycrystalline electrodes), the image size can affect the measured NP average density. Finally, not all experimental systems are applicable to all the aforementioned imaging methods e.g. when the electrode is sealed within the experimental setup or when the electrode is bigger than the imaging chamber.

It is imperative that the NPs are stable under the conditions of the experiment as detachment, fouling or aggregation could lead to decreasing signals and erroneous analysis with extended use.[89] NP aggregation is well known to be exacerbated at elevated temperatures.[96] There is however a dearth of literature on the stability of NP under flow. There are limited reports of metal NPs on carbon electrodes under hydrodynamic (flow or rotation) conditions, however the metal NPs are often held in place by a support or mask to stabilize the particles in the flow environment.[93,97-101] Pt[102] and Au[103] NPs have been employed in conjunction with rotating BDD electrodes, however, the mechanical stability of the NPs, under these forced convection conditions, was not discussed.

1.3.5 Electrochemistry of Pharmaceuticals

Although electrochemistry is a well-established analytical discipline, electrochemical analysis is not commonplace in the pharmaceutical industry, certainly not to the degree of MS, HPLC, or the majority of the methods described in section 1.2.1 of this thesis. Despite this, EC is utilised in combination with other methods for example; CE-EC,[28] IC-EC[29] and HPLC-EC.[104] Furthermore, many GIs and APIs have been studied electrochemically and extensive lists are reported by Ozkan *et al.*[105] and Gupta *et al.*[106] We can glean some important facts from these reviews: i) Many GIs and APIs are electrochemically active. ii) The majority of these studies investigate the GI or API alone,[107] sometimes in equal quantities to other interferants[108] and sometimes in pharmaceutical formulations or human urine.[109] iii) Often, as is comfortable for electrochemists, determination is carried out in

aqueous solutions, as non-aqueous electrochemistry is less frequently practiced and correspondingly less well understood.[110]

1.3.6 Hydrazine Electrochemistry

HZ undergoes inner sphere ET with an $E_{1/2}$ strongly dependant on the chemical identity and crystallographic orientation, when considering metal electrodes.[43,111] ET can be described by the following general mechanism:

$$N_2H_4 \rightarrow N_{2\,(g)} + 4H^+ + 4e^- \tag{1.30}$$

Note that the ET is irreversible and evolves four electrons and protons for each HZ molecule oxidised. Due to its inner sphere ET mechanism, large diffusion coefficient[112] and multiple electrons per molecule,[113] HZ is an ideal electrochemical analyte for NP collision experiments, where the electrochemical response of single NPs can be elucidated.

It is also interesting to note the role of protons in the mechanism. In fact, HZ electrooxidation has been shown to be strongly pH dependant.[114] At pH's below the pKa (= 8.1),[115] HZ will be initially protonated in solution, thus equation 1.30 becomes,

$$N_2H_5^+ \rightarrow N_{2\,(g)} + 5H^+ + 4e^- \tag{1.31}$$

HZ oxidation is also concentration dependant with some authors showing deviations form a linear *i vs* concentration relationship at high concentrations (>0.05 M), attributed in this case to a Langmuir-type adsorption process.[116] Although HZ is commonly determined in aqueous solvents, non-aqueous detection is possible, though the mechanism and diffusion coefficients differ compared to aqueous systems.[110,117,118]

HZ electrooxidation is very kinetically facile on Pt and its mechanism has been studied in detail in literature.[43,119-121] The mechanism, as given by Álvarez-Ruiz *et al.*[122] is as follows,

$$N_2H_5^+ \rightleftharpoons N_2H_{3ads} + 2H^+ + e^- \quad (1.32)$$

$$N_2H_{3ads} \xrightarrow{RDS} N_2H_{2ads} + H^+ + e^- \quad (1.33)$$

$$N_2H_{2ads} \xrightarrow{FAST} N_2H_{ads} + H^+ + e^- \quad (1.34)$$

$$N_2H_{ads} \rightarrow N_{2ads} + H^+ + e^- \quad (1.35)$$

$$N_{2ads} \rightarrow N_{2(g)} \quad (1.36)$$

where the 'ads' subscript implies a species adsorbed to the Pt surface. The first step involves the formation of a bond between the lone pair of the nitrogen and the dy orbital of the Pt surface. The rate determining step (RDS) then involves the formation of a bond between the other nitrogen and a neighbouring Pt atom.

Another common electrode for HZ oxidation is Au. The mechanism differs on Au compared to Pt due to the differing surface bond lengths (leading to different HZ-metal bond overlap) and d-orbital filling between Pt and Au.[112,123-125] The mechanism, as given by Wang *et al.*[123] is as follows,

$$N_2H_5^+ \xrightarrow{RDS} N_2H_{3ads} + 2H^+ + e^- \quad (1.37)$$

$$N_2H_{3ads} \xrightarrow{FAST} N_2 + 3H^+ + 3e^- \quad (1.38)$$

Here the RDS involves the initial HZ-metal bond formation, but the overall oxidation products are the same as with Pt (following a series of fast decomposition steps). On non-metallic electrodes, HZ oxidation is not as well catalysed resulting in higher required η. This is particularly exacerbated for BDD where a large η (*ca* 1.8 V *vs* SCE) is observed, although the mechanism has not been fully studied in this system.[126,127]

There are many reports in literature over the last four years pertaining to the electrochemical trace detection of HZ, as described in Table 1.3

Technique	Electrode	LOD	System	Ref.
Amperometry	BiNP-graphene nanosheet/GCE	0.005 μM	HZ alone	[128]
Amperometry	AuPdCu/MWCNT/GCE	0.02 μM	HZ alone	[129]
Amperometry	CuONP/GCE	0.03 μM	HZ alone	[130]
Amperometry	poly(Bromocresol purple)/CNT/GCE	0.1 μM	HZ alone	[131]
Amperometry	PdNP- Poly(2-acryalamido-2-methyl-propane-sulfonic acid)-polyaniline	0.42 μM	HZ alone	[132]
Amperometry	Ag dentrites / ITO	0.5 μM	HZ alone	[133]
Amperometry	PtNP/Polydopamine-ordered mesoporous carbons/GCE	0.51 μM	HZ alone	[134]
Amperometry	AuNP/ssDNA/Au	0.56 μM	HZ alone	[135]
Amperometry	Chitosan/carbon-nanofiber/GCE	2.7 μM	HZ alone	[136]
Amperometry	PdNP/carbon black	8.8 μM	HZ alone	[137]
Amperometry	CoOOH nanosheet	20 μM	HZ alone	[138]
CV	CuS/graphene oxide/GCE	0.3 μM	HZ alone	[139]
CV	AuNP-polypyrrole/Fe	6 μM	HZ alone	[140]
CV	Pd-TiO_2	23 μM	HZ alone	[141]
CV / RDE	Pedot- PdNP	0.8 μM	HZ alone	[142]
CV and DPV	BDD	1 μM	HZ alone	[127]
DPV	Au-SH-SiO_2/Cu-MOF	0.01 μM	HZ alone	[143]
DPV	4 alpha-Ni(II)TAPc-AuNP/Au	0.05 μM	HZ alone	[144]
DPV	Co(II)bis-benzoylacetone-ethylenediimino-MWCNT-CPE	0.1 μM	HZ alone	[145]
DPV	Polyaniline/Au/GCE	1 μM	HZ alone	[146]
Photoelectroche-mical LSV / CV	TiO_2	30 μM	HZ alone	[147]
SWV	AuNP-CPE	0.042 μM	HZ alone	[148]

Table 1.3: List of electrochemical methods for HZ detection from the last four years where a LOD was calculated, ITO: indium tin oxide, MWCNT: multiwall CNT, RDE: rotating disk electrode, MOF: metal-organic framework, SWV: square wave voltammetry and CPE: carbon paste electrode.

It is interesting to note that the majority of the electrodes used are modified, often with multiple steps (e.g. sensing species bound to NP, bound to a GCE). Furthermore, across all of these studies HZ is only ever quantified down to trace amounts in solution containing only HZ and supporting electrolyte. Additionally, any measurements in the presence of other species are normally carried out at equivalent concentrations, usually as a recovery test.[130,133] Therefore, despite the wide range of electrodes demonstrated to determine HZ to low detection limits, there is a dearth of knowledge surround trace HZ determination in the presence of excess interferants such as APIs.

1.4 Hydrodynamic methods

As described by equations 1.19 and 1.21, convection can contribute to mass transport, increasing the flux towards the electrode and thus the current. Therefore many hydrodyanamic methods take advantage of the increased faradaic signal through convection. This is usually carried out by rotation of the electrode (RDE),[149] heating of the electrode or solution,[150] or flow of the electrolyte solution through an porous electrode,[151] against (e.g. impinging jet electrode),[152] or over the electrode (e.g. channel flow cell).[153] Channel flow cells are of particular interest due to their applicability to FIA, as well as and their simpler theoretical treatments compared to other hydrodynamic methods.[154]

In the case of solution flow through a tube or channel, two characteristic flow regimes are observed as depicted in Figure 1.19:

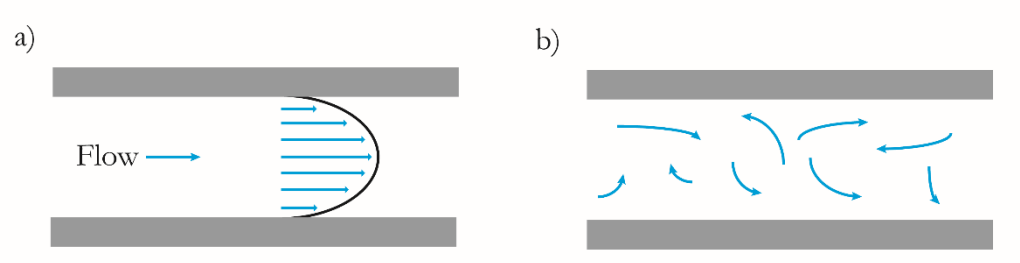

Figure 1.19: Velocity profiles for a) laminar and b) turbulent flow.[155]

Laminar flow (Figure 1.19a), also known as poiseuille flow, is characterised by an ordered velocity profile where the velocity is at its highest in the middle of the channel and decays to zero at the walls. Conversely turbulent flow (Figure 1.19b) is chaotic and poorly defined such that velocity at any point in the tube is difficult to predict and often changing.[42]

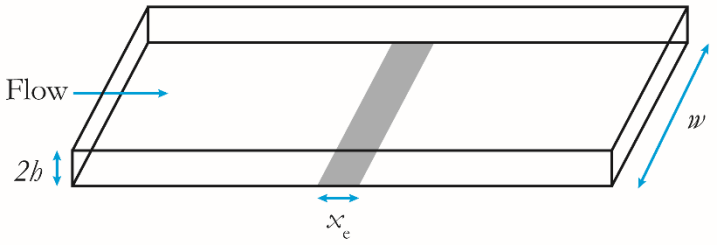

Figure 1.20: Schematic of a band electrode in a typical channel flow cell, $2h$ is the channel height, w is the channel width and x_e is the electrode width.

Consider a channel flow cell as depicted in Figure 1.20. The velocity profile in a high aspect ratio (2h<<w) channel of the type used in this thesis is given by,[156]

$$u_z = u_0\left[1 - \left(\frac{2z}{(2h)}\right)^2\right] \tag{1.39}$$

where u_z is the velocity at height z in the channel and u_0 is the maximum velocity at the centre of the channel, as given by,

$$u_0 = \frac{3\bar{U}}{2} \tag{1.40}$$

where $\bar{U}$ is the mean fluid velocity (cm s^{-1}) given by,

$$\overline{U} = \frac{V_f}{2hw} \tag{1.41}$$

In fact, the mode of flow in this system (laminar or turbulent) can be determined by the Reynolds number (*R*e) given by,[157]

$$R_e = \frac{\overline{U} D_h}{\nu'} \tag{1.42}$$

where ν' is the kinematic viscosity (= 0.01 $cm^2\ s^{-1}$)[157] and D_h is the hydraulic diameter (cm) given by,

$$D_h = \frac{8wh}{2h+w} \tag{1.43}$$

Laminar flow is observed for system with an Re < 2000,[158] hence hydrodynamic experiments are typically carried out within small channels and with moderate flow rates and viscosities.

Due to the enhanced mass transport from convection, steady state behaviour is observed (Figure 1.10) in hydrodynamic CVs, even with large (macro) electrodes at moderate flow rates.[159] Hence, it is important for analytical method development that the mass transport is well understood. The current for a band electrode in a channel flow cell under continuous flow of the electroactive species is given by the Levich equation,[154]

$$i_{lim} = 0.925 n F c_b D^{2/3} V_f^{1/3} w^{2/3} h^{-2/3} x_e^{2/3} \tag{1.44}$$

This equation is valid so long as i) laminar flow is fully developed in the channel before reaching the electrode, ii) diffusion along the direction of flow is negligible and iii) the concentration gradient is confined adjacent to the electrode (Lévêque approximation).[154]

1.4.1 Flow Injection Analysis

FIA is a well-established technique[160-163] which has seen increasing recent use in the pharmaceutical industry.[164-167] In short, a plug of analyte of known volume is injected into a flowing carrier stream, which transports the plug to a detector. Compared to other hydrodynamic methods, FIA has very small reagent consumption, well defined and very reproducible mass transport and the analytical signals are easy to interpret. A general schematic of a typical FIA setup is shown below (Figure 1.21):

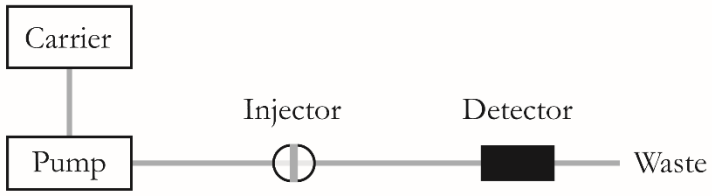

Figure 1.21: Schematic of a typical FIA setup.

The specifics of the experimental setup are dependent on the application, for example mixers, dialysis, reactors and solvent extraction can be carried out on-line.[168-171] Additionally, there are a wide variety of utilised detectors such as UV, fluorescence, spectroscopic and EC.[79,172-174]

In the case of FIA with electrochemical detection (FIA-EC), the carrier stream usually contains a background electrolyte and occasionally a buffer. Typically, a band electrode is housed within a channel flow cell (Fig 1.20), operated in amperometric (apply *E* measure *i*) or potentiometric (apply *i* measure *E*) modes. In comparison to continuous flow CV, FIA-EC operated in amperometric mode exhibits smaller background signals, resulting in better signal to noise ratios.[159] Furthermore, continuous flow CV requires that whole system be emptied and replaced with a new solution each time a new measurement is required, for example; of an alternate analyte or new concentration, leading to long

experimental times and large reagent consumption. Therefore FIA-EC is an ideal method for the trace detection of small quantities of analyte.

We can now identify the dynamics of a typical FIA-EC system. Consider a plug of analyte injected into a carrier stream. The plug shape and dimensions under different conditions are given in Figure 1.22:

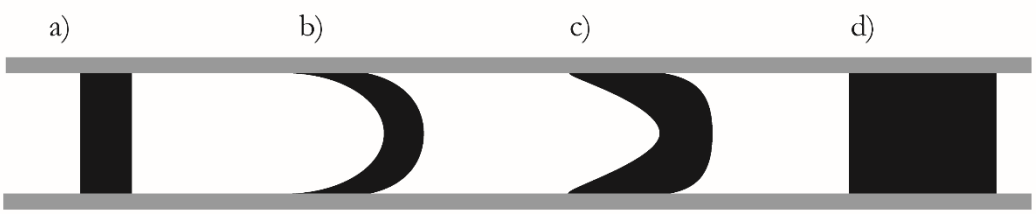

Figure 1.22: Illustration of a typical FIA plug a) initially, b) poiseuille (convection controlled region), c) diffusion-convection region and d) Taylor region (diffusion controlled).[175]

Straight after injection (a), axial dispersion (along the axis of flow) occurs at the plug-carrier stream edges where there is a sharp concentration gradient. Then, convection from the flow velocity profiles distorts the plug to a poiseuille shape (b). Next, radial diffusion (perpendicular to the direction of flow) diffuses the front of the plug outwards from the channel centre (to a lower u_z) as well as inwards from the backwards edges by the channel wall (to a higher u_z), serving to quench the distorted poiseuille shape (c). Over extended periods of time a combination of convection, axial and radial diffusion will lead to a flat plug shape of increased volume compared to the initial plug (i.e. lower concentration).[175] The occurrence of poiseuille, diffusion-convection or Taylor plug behaviour is dependent on the channel dimensions, flow rate and the time spent under flow (i.e. channel length). The corresponding analytical signal from the three plug shapes is given in Figure 1.23.

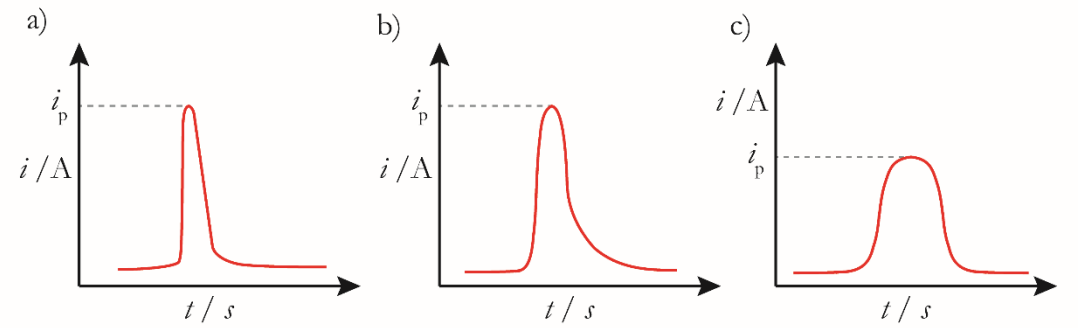

Figure 1.23: Illustration of typical FIA-EC peak signals for the plugs shown in Figure 1.20, a) corresponds to poiseuille flow, b) to convection-diffusion and c) to Taylor flow.[176]

Due to the stretched profile, poiseuille flow exhibits an asymmetric, sharp rise then slow decay profile (Figure 1.23a). At the other extreme, Taylor dispersion results in a broad symmetrical peak with decreased peak height compared to the other cases (Figure 1.23c). Most experimental FIA systems however, exhibit a skewed 'Gaussian' response (Figure 1.23b) with a sharp rise and slightly slower fall from the peak signal, denoted i_p in the case of FIA-EC.

1.4.1.1 Theory of Dispersion and Residence Time in Flow Injection Analysis

For simplicity's sake, most FIA systems are characterised by two factors to facilitate comparison and understanding, namely the residence time t_r and the dispersion coefficient D_c. t_r is defined as the time taken between injection and the maximum signal, this effectively controls the maximum possible frequency of measurement. D_c is defined by,[163]

$$D_c = \frac{c^0}{c^{\max}} \tag{1.45}$$

where C^0 is the initial concentration of the plug and C^{max} is the maximum concentration of the plug at the peak signal. This equation considers only physical dispersion (e.g. mass transport and dead volumes – discussed below) but not dispersion through chemical reactions. This relationship operates on the basis that any dispersion will lead to an increase

in plug volume and hence reduction in concentration, resulting in an i_p smaller than the theoretical maximum (i_{lim}, equation 1.44).[163] We can re-write equation 1.45 as,

$$D_c = \frac{i_{\mathrm{lim}}}{i_{\mathrm{p}}} \tag{1.46}$$

such that $D_c = 1$ represents negligible dispersion and $D_c = 2$ represents dispersion into the carrier stream to double the volume (i.e. half the concentration).

The dispersion in FIA can be further quantified by solving the diffusion-convection equation for dispersion in a cylindrical tube,[175]

$$D\left(\frac{\delta^2 C}{\delta x^2} + \frac{\delta^2 C}{\delta r^2} + \frac{1}{r}\frac{\delta C}{\delta r}\right) = \frac{\delta C}{\delta r} + u_0\left[1 - \left(\frac{r}{a}\right)^2\right]\frac{\delta C}{\delta x} \tag{1.47}$$

where the left term is the diffusion-convection for a radial coordinate system and the right terms are the radial diffusion and product of the convection and axial diffusion respectively, *a* is the tube radii. Various numerical and computational simulations have been carried out to solve this equation in different FIA systems, as shown in Figure 1.24, with the sections they apply and the authors shown.

To facilitate classification, the ratio of mass transport by convection *vs* dispersion is defined by the dimensionless Peclet number (P_e),

$$P_{\mathrm{e}} = \frac{u_0}{D} \tag{1.48}$$

Similarly, a dimensionless time τ_d is defined by,

$$\tau_{\mathrm{d}} = \frac{D \times t}{(2h)^2} \tag{1.49}$$

Interestingly the solutions by Taylor,[177] Aris,[178] Ananthakrishnan,[179] Stewart[180] and Růžička[181] as shown in Figure 1.24 do not account for the majority of experimental FIA systems.[175]

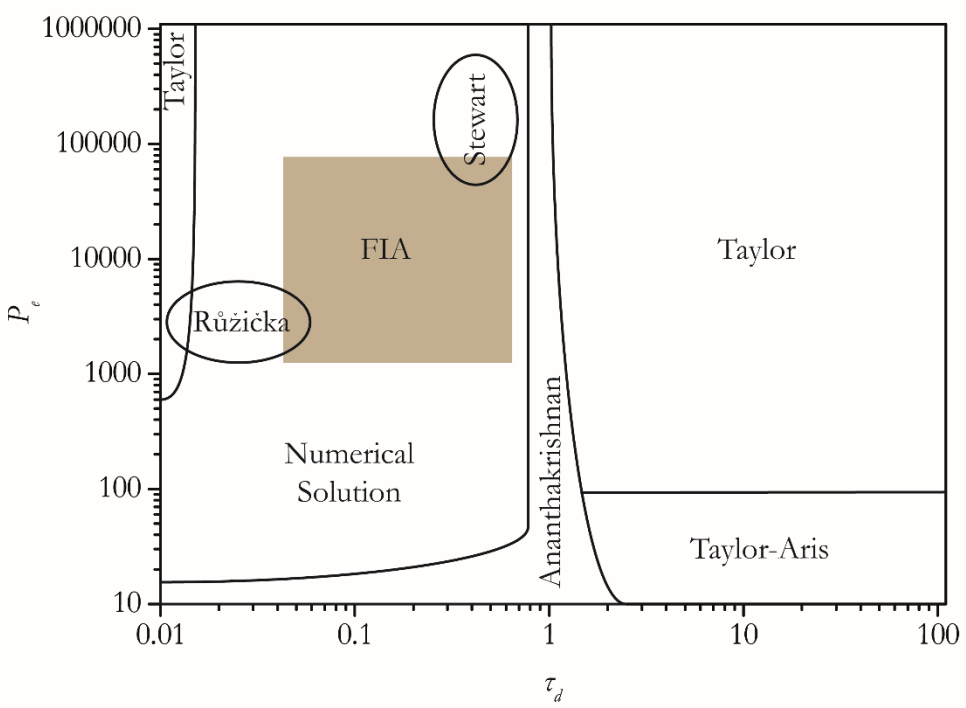

Figure 1.24: Schematic of solutions to the diffusion-convection equation (1.47), with common experimental systems in segmented sections and typical FIA experiments in the brown shaded region.[182,183]

As well as convection and axial / radial diffusion increasing dispersion, dispersion is also exacerbated by dead volumes,[184] created when there are sudden and significant changes in cross-sectional area, whereby the laminar flow is perturbed leaving some material trapped in areas of low fluid velocity. These are sometimes referred to as 'eddies' or 'recirculating zones' by different authors.[185] These effects lead to 'tailing' of the plug, as material takes longer to pass through the system such that the signal takes a longer time to decay to the background level. Also, changes in geometry can lead to multiple flow paths of different length – known as secondary flows - leading to a humped peak resulting from the different flow path lengths.[186] These secondary flows effectively also occur in any curved tubing, where the Poiseuille flow profile is not symmetrical across the tube.[187] Dispersion, dead volumes and secondary flows are discussed in more detail in chapter 4.

1.5 Aims and Objectives

As discussed above, there is a need for new approaches that can detect GIs in the presence of an excess of API. Furthermore, new approaches must endeavour to overcome some of the several disadvantages of current methods namely; cost of equipment and maintenance, inability to operate inline, requirement of various sample preparations for detection, speed of analysis, complexity, and adaptability to multiple GI:API systems. Demonstration of multiple electrochemical approaches to detect HZ – one of the most challenging GIs for current methodologies – would make great strides towards resolution of this problem within the pharmaceutical industry. Progress must be judged based not only on success of the individual methods, but with a view towards detection on-line, in the pharmaceutical formulation, containing likely an excess of API, in various solvents (aqueous and non-aqueous) and crucially; to the safe levels stipulated by pharmaceutical guidelines.

Towards this goal, chapter 3 serves as a proof of concept study, to demonstrate the electrochemical detection of HZ under quiescent conditions in aqueous solution in the presence of two electrochemically active APIs; acetaminophen (ACM, paracetamol) and promazine (PZ) added in excess. It is shown that by using a metal NP functionalized BDD electrode and by simply changing the chemical identity of the metal NP; it is possible to screen out interference effects from both APIs, thus tuning the sensor for detection of the GI in the presence of different electrochemically active APIs.

The detection limits from this quiescent study do not reach the safe limits set by the pharmaceutical industry for GI detection in the presence of an API. Therefore, a hydrodynamic approach is adopted in chapter 4 to take advantage of the convective contribution to mass transport and hence reach lower detection limits. A new FIA setup is developed based on an optimised flow cell, in terms of design to maximise FIA signal,

reproducibility and sampling rate, coupled with an all diamond BDD microband electrode. The new setup is shown to have reduced dispersion, high possible sampling frequency and lower sample volume requirement compared to previous designs in literature. Furthermore, the all-diamond device represents a durable, long lasting co-planar electrode which simplifies characterisation and reduces the occurrence of leaks.

Chapter 5 serves to apply this developed FIA system with a NP functionalised all-diamond BDD band micro electrode for the detection of HZ in the presence of a large excess of API. The stability of NP under flow is also investigated by electrochemical and non-electrochemical means. This aims to make use of the enhanced mass transport towards achieving the pharmaceutical safe detection limits which have not been previously demonstrated electrochemically. Chapter 6 concludes the thesis.

1.6 References

(1) Jones, H. M.; Chen, Y.; Gibson, C.; Heimbach, T.; Parrott, N.; Peters, S. A.; Snoeys, J.; Upreti, V. V.; Zheng, M.; Hall, S. D. *Clinical Pharmacology & Therapeutics* **2015**, *97*, 247-262.

(2) Maggio, R. M.; Castellano, P. M.; Kaufman, T. S. *Int J Pharmaceut* **2009**, *378*, 187-193.

(3) Blaser, H.-U. *Rend. Fis. Acc. Lincei* **2013**, *24*, 213-216.

(4) Siddiqui, M. R.; AlOthman, Z. A.; Rahman, N. *Arabian Journal of Chemistry* **2013**, doi:10.1016/j.arabjc.2013.1004.1016.

(5) Robinson, D. I. *Org. Process Res. Dev.* **2010**, *14*, 946-959.

(6) Müller, L.; Mauthe, R. J.; Riley, C. M.; Andino, M. M.; Antonis, D. D.; Beels, C.; DeGeorge, J.; De Knaep, A. G. M.; Ellison, D.; Fagerland, J. A.; Frank, R.; Fritschel, B.; Galloway, S.; Harpur, E.; Humfrey, C. D. N.; Jacks, A. S.; Jagota, N.; Mackinnon, J.; Mohan, G.; Ness, D. K.; O'Donovan, M. R.; Smith, M. D.; Vudathala, G.; Yotti, L. *Regul. Toxicol. Pharmacol.* **2006**, *44*, 198-211.

(7) Reddy, A. V. B.; Jaafar, J.; Umar, K.; Majid, Z. A.; Aris, A. B.; Talib, J.; Madhavi, G. *Journal of Separation Science* **2015**, *38*, 764-779.

(8) Fetterman, B. A.; Kim, B. S.; Margolin, B. H.; Schildcrout, J. S.; Smith, M. G.; Wagner, S. M.; Zeiger, E. *Environmental and Molecular Mutagenesis* **1997**, *29*, 312-322.

(9) Teasdale, A. *Genotoxic Impurities Stratagies for Identification and Control*; John Wiley & Sons: New Jersey, 2010, p 428.

(10) Teasdale, A.; *Guidance for Industry. Genotoxic and Carcinogenic Impurities in Drug Substances and Products: Recommended Approaches.*: US Department of Health and Human Services, Food and Drug Administration, Center for Drug Evaluation and Research (CDER), 2008.

(11) Davis, I. I. W. E.; Li, Y. *Anal Chem* **2008**, *80*, 5449-5453.
(12) Oh, J. A.; Shin, H. S. *Journal of Chromatography A* **2015**, *1395*, 73-78.
(13) Snodin, D. J. *Org Process Res Dev* **2010**, *14*, 960-976.
(14) Dewanji, A.; Murarka, S.; Curran, D. P.; Studer, A. *Org. Lett.* **2013**, *15*, 6102-6105.
(15) Graham, M. A.; Bethel, P. A.; Burgess, J.; Fairley, G.; Glossop, S. C.; Greenwood, R. D. R.; Jones, C. D.; Lovell, S.; Swallow, S. *Org. Lett.* **2013**, *15*, 6078-6081.
(16) Uygun, Y.; Bayrak, H.; Ozkan, H. *Turk. J. Chem.* **2013**, *37*, 812-823.
(17) Farghaly, T.; Abdallah, M.; Aziz, M. *Molecules* **2012**, *17*, 14625-14636.
(18) Sycheva, T. P.; Pavlova, T. N.; Shchukina, M. N. *Pharm. Chem. J.* **1972**, *6*, 696-698.
(19) Sakamoto, T.; Asazawa, K.; Sanabria-Chinchilla, J.; Martinez, U.; Halevi, B.; Atanassov, P.; Strasser, P.; Tanaka, H. *J. Power Sources* **2014**, *247*, 605-611.
(20) Elder, D. P.; Snodin, D.; Teasdale, A. *J. Pharm. Biomed. Anal.* **2011**, *54*, 900-910.
(21) Sun, M. J.; Bai, L.; Liu, D. Q. *J. Pharm. Biomed. Anal.* **2009**, *49*, 529-533.
(22) Kean, T.; Miller, J. H. M.; Skellern, G. C.; Snodin, D. *Pharmeuropa scientific notes* **2006**, *2*, 23-33.
(23) Gyllenhaal, O.; Grönberg, L.; Vessman, J. *J. Chromatogr. A* **1990**, *511*, 303-315.
(24) Matsui, F.; Robertson, D. L.; Lovering, E. G. *J. Pharm. Sci.* **1983**, *72*, 948-951.
(25) Mañes, J.; Gimeno, M. J.; Moltó, J. C.; Font, G. *J. Pharm. Biomed. Anal.* **1988**, *6*, 1023-1027.
(26) Qu, D.-Y.; Chen, J.-L.; Di, B. *Anal. Methods* **2014**, *6*, 4705-4709.
(27) Khan, M.; Kumar, S.; Jayasree, K.; Krishna Reddy, K. V. S. R.; Dubey, P. K. *Chromatographia* **2013**, *76*, 801-809.
(28) You, T.; Niu, L.; Gui, J. Y.; Dong, S.; Wang, E. *J. Pharm. Biomed. Anal.* **1999**, *19*, 231-237.
(29) Jagota, N. K.; Chetram, A. J.; Nair, J. B. *J. Pharm. Biomed. Anal.* **1998**, *16*, 1083-1087.
(30) Liu, M.; Ostovic, J.; Chen, E. X.; Cauchon, N. *J. Chromatogr. A* **2009**, *1216*, 2362-2370.
(31) Liu, J.; Zhou, W.; You, T.; Li, F.; Wang, E.; Dong, S. *Anal. Chem.* **1996**, *68*, 3350-3353.
(32) Tremillon, B. *Actual Chim.* **2009**, 10-26.
(33) Whittaker, E. T. *A history of the theories of aether and electricity from the age of Descartes to the close of the nineteenth century*; Longmans, Green and co.: London, New York, 1910.
(34) Gilbert, W.; Mottelay, P. F.; Wright, E. *William Gilbert of Colchester, physician of London, On the loadstone and magnetic bodies, and on the great magnet the earth*; J. Wiley & sons: New York,, 1893, p 368.
(35) Von Handorf, D. E. *Plat. Surf. Finish.* **2002**, *89*, 84-87.
(36) Yin, Y.-X.; Xin, S.; Guo, Y.-G.; Wan, L.-J. *Angewandte Chemie International Edition* **2013**, *52*, 13186-13200.
(37) Wei, D.; Andrew, P.; Ryhänen, T. *Journal of Chemical Technology & Biotechnology* **2010**, *85*, 1547-1552.
(38) Wang, J. *Chemical Reviews* **2008**, *108*, 814-825.
(39) Lim, R. J.; Xie, M.; Sk, M. A.; Lee, J.-M.; Fisher, A.; Wang, X.; Lim, K. H. *Catalysis Today* **2014**, *233*, 169-180.
(40) Wang, G.; Zhang, L.; Zhang, J. *Chemical Society Reviews* **2012**, *41*, 797-828.
(41) Lu, M.; Compton, R. G. *Analyst* **2014**, *139*, 4599-4605.
(42) Bard, A. J.; Faulkner, L. R. *Electrochemical Methods: Fundamentals and Applications*, 2nd ed.; John Wiley & Sons: New York, 1980.

(43) Azorero, M. D. G.; Marcos, M. L.; Velasco, J. G. *Electrochim. Acta* **1994**, *39*, 1909-1914.
(44) Liu, Y.; Li, M.; Zhang, F.; Zhu, A.; Shi, G. *Anal Chem* **2015**, *87*, 5531-5538.
(45) Joseph, M. B.; Bitziou, E.; Read, T. L.; Meng, L.; Palmer, N. L.; Mollart, T. P.; Newton, M. E.; Macpherson, J. V. *Anal. Chem.* **2014**, *86*, 5238-5244.
(46) Macpherson, J. V.; Unwin, P. R. *The Journal of Physical Chemistry* **1996**, *100*, 19475-19483.
(47) Brett, C. M. A.; Brett, A. M. O. *Electrochemistry : principles, methods, and applications*; Oxford University Press: Oxford, 1993.
(48) Compton, R. G.; Banks, C. E. *Understanding Voltammetry*, 2nd ed.; Imperial College Press: London, 2011.
(49) Dickinson, E. J. F.; Limon-Petersen, J. G.; Rees, N. V.; Compton, R. G. *The Journal of Physical Chemistry C* **2009**, *113*, 11157-11171.
(50) Helmholtz, H. *Annalen der Physik* **1879**, *243*, 337-382.
(51) Chapman, D. L. *Philosophical Magazine Series 6* **1913**, *25*, 475-481.
(52) Grahame, D. C. *Chemical Reviews* **1947**, *41*, 441-501.
(53) Han, K. N. *Fundamentals of aqueous metallurgy*; Society for Mining, Metallurgy, and Exploration: Littleton, Colo., 2002, p xii, 197 p.
(54) Bard, A. J. *J Am Chem Soc* **2010**, *132*, 7559-7567.
(55) Nicholson, R. S.; Shain, I. *Anal Chem* **1964**, *36*, 706-723.
(56) J. Ho, M. L. C., C. J. Cramer and D. G. Truhlar,. *Theoretical Calculation of Reduction Potentials. Organic Electrochemistry*, 5th ed.; CRC Press, Boca Raton, FL, 2013.
(57) Heinze, J. *Angewandte Chemie International Edition in English* **1991**, *30*, 170-171.
(58) Nicholson, R. S. *Anal Chem* **1965**, *37*, 1351-1355.
(59) Hernández, L.; Zapardiel, A.; Bermejo, E.; Pérez-López, J. A.; Pérez-Fernández, J. C. *Anal. Chim. Acta* **1996**, *336*, 85-93.
(60) Alkire, R. C.; Bartlett, P. N.; Lipkowski, J. *Electrochemistry of carbon electrodes*; John Wiley & Sons: Pennington, NJ, 2015; Vol. 16, p 350.
(61) Falcao, E. H. L.; Wudl, F. *Journal of Chemical Technology & Biotechnology* **2007**, *82*, 524-531.
(62) May, P. W. *Philos. Trans. R. Soc. Lond. Ser. A-Math. Phys. Eng. Sci.* **2000**, *358*, 473-495.
(63) Williams, A. W. S.; Lightowlers, E. C.; Collins, A. T. *Journal of Physics C: Solid State Physics* **1970**, *3*, 1727.
(64) Lagrange, J. P.; Deneuville, A.; Gheeraert, E. *Diamond and Related Materials* **1998**, *7*, 1390-1393.
(65) Yan, B. M.; Jia, X. P.; Sun, S. S.; Zhou, Z. X.; Fang, C.; Chen, N.; Li, Y. D.; Li, Y.; Ma, H. A. *Int. J. Refract. Met. Hard Mat.* **2015**, *48*, 56-60.
(66) Yu. Dolmatov, V. *Russian Chemical Reviews* **2001**, *70*, 607-626.
(67) Galimov, É. M.; Kudin, A. M.; Skorobogatskii, V. N.; Plotnichenko, V. G.; Bondarev, O. L.; Zarubin, B. G.; Strazdovskii, V. V.; Aronin, A. S.; Fisenko, A. V.; Bykov, I. V.; Barinov, A. Y. *Dokl. Phys.* **2004**, *49*, 150-153.
(68) Macpherson, J. V. *Phys Chem Chem Phys* **2015**, *17*, 2935-2949.
(69) Charles, S. J.; Steeds, J. W.; Evans, D. J. F.; Butler, J. E. *Mater. Lett.* **2003**, *57*, 3690-3693.
(70) Duo, I.; Levy-Clement, C.; Fujishima, A.; Comninellis, C. *Journal of Applied Electrochemistry* **2004**, *34*, 935-943.
(71) Hutton, L. A.; Iacobini, J. G.; Bitziou, E.; Channon, R. B.; Newton, M. E.; Macpherson, J. V. *Anal. Chem.* **2013**, *85*, 7230-7240.
(72) Tryk, D. A.; Tachibana, H.; Inoue, H.; Fujishima, A. *Diamond and Related Materials* **2007**, *16*, 881-887.

(73) Thomas, R. E.; Rudder, R. A.; Markunas, R. J. *Journal of Vacuum Science & Technology A* **1992**, *10*, 2451-2457.
(74) Hutton, L.; Newton, M. E.; Unwin, P. R.; Macpherson, J. V. *Anal. Chem.* **2009**, *81*, 1023-1032.
(75) Wilson, N. R.; Clewes, S. L.; Newton, M. E.; Unwin, P. R.; Macpherson, J. V. *The Journal of Physical Chemistry B* **2006**, *110*, 5639-5646.
(76) Pleskov, Y. V. *Russ J Electrochem* **2002**, *38*, 1275-1291.
(77) Brillas, E.; Martínez-Huitle, C. A. *Synthetic diamond films: preparation, electrochemistry, characterization, and applications*; John Wiley & Sons: Hoboken, N.J., 2011, p 680.
(78) Granger, M. C.; Witek, M.; Xu, J.; Wang, J.; Hupert, M.; Hanks, A.; Koppang, M. D.; Butler, J. E.; Lucazeau, G.; Mermoux, M.; Strojek, J. W.; Swain, G. M. *Anal Chem* **2000**, *72*, 3793-3804.
(79) Sansuk, S.; Bitziou, E.; Joseph, M. B.; Covington, J. A.; Boutelle, M. G.; Unwin, P. R.; Macpherson, J. V. *Anal. Chem.* **2013**, *85*, 163-169.
(80) Silva, E. L.; Gouvêa, C. P.; Quevedo, M. C.; Neto, M. A.; Archanjo, B. S.; Fernandes, A. J. S.; Achete, C. A.; Silva, R. F.; Zheludkevich, M. L.; Oliveira, F. J. *Anal Chem* **2015**, *87*, 6487-6492.
(81) Ye, Y.; Huang, X.; Yang, C.; Chen, Y.; Zhao, W.; Wu, D. In *Proceedings of the Sixteenth*, Chung, J. S.; Hong, S. W.; Marshall, P. W.; Komai, T.; Koterayama, W., Eds.; International Society Offshore& Polar Engineers: Cupertino, 2006, pp 304-306.
(82) Ghica, M. E.; Pauliukaite, R.; Fatibello-Filho, O.; Brett, C. M. A. *Sensor Actuat B-Chem* **2009**, *142*, 308-315.
(83) Wang, H. M.; Wu, Z. C.; Plaseied, A.; Jenkins, P.; Simpson, L.; Engtrakul, C.; Ren, Z. Y. *J. Power Sources* **2011**, *196*, 7465-7469.
(84) Szunerits, S.; Manesse, M.; Actis, P.; Marcus, B.; Denuault, G.; Jama, C.; Boukherroub, R. *Electrochem. Solid State Lett.* **2007**, *10*, G43-G46.
(85) Koper, M. T. M. *Nanoscale* **2011**, *3*, 2054-2073.
(86) Kneipp, K.; Kneipp, H.; Itzkan, I.; Dasari, R. R.; Feld, M. S. *Chemical Reviews* **1999**, *99*, 2957-+.
(87) Pankhurst, Q. A.; Connolly, J.; Jones, S. K.; Dobson, J. *Journal of Physics D-Applied Physics* **2003**, *36*, R167-R181.
(88) Chen; Cai, Y.; Yan, Z.; Goodman, D. W. *J Am Chem Soc* **2006**, *128*, 6341-6346.
(89) Kleijn, S. E. F.; Lai, S. C. S.; Koper, M. T. M.; Unwin, P. R. *Angew. Chem., Int. Ed.* **2014**, *53*, 3558-3586.
(90) Hampton, M. A.; Nguyen, T. A. H.; Nguyen, A. V.; Xu, Z. P.; Huang, L.; Rudolph, V. *Journal of Colloid and Interface Science* **2012**, *377*, 456-462.
(91) Dai, J. H.; Bruening, M. L. *Nano Lett.* **2002**, *2*, 497-501.
(92) Salimi, A.; Kurd, M.; Teymourian, H.; Hallaj, R. *Sens. Actuator B-Chem.* **2014**, *205*, 136-142.
(93) de Oliveira, P. R.; Oliveira, M. M.; Zarbin, A. J. G.; Marcolino, L. H.; Bergamini, M. F. *Sens. Actuator B-Chem.* **2012**, *171*, 795-802.
(94) Zhou, J. Y.; Barbara, P.; Paranjape, M. *J. Nanosci. Nanotechnol.* **2010**, *10*, 3890-3894.
(95) Vidal-Iglesias, F. J.; Aran-Ais, R. M.; Solla-Gullon, J.; Herrero, E.; Feliu, J. M. *ACS Catalysis* **2012**, *2*, 901-910.
(96) Puertolas, B.; Mayoral, A.; Arenal, R.; Solsona, B.; Moragues, A.; Murcia-Mascaros, S.; Amoros, P.; Hungria, A. B.; Taylor, S. H.; Garcia, T. *ACS Catalysis* **2015**, *5*, 1078-1086.
(97) Zen, J. M.; Hsu, C. T.; Kumar, A. S.; Lyuu, H. J.; Lin, K. Y. *Analyst* **2004**, *129*, 841-845.

(98) Li, X.-H.; Xie, Z.-H.; Min, H.; Xian, Y.-Z.; Jin, L.-T. *Electroanal.* **2007**, *19*, 2551-2557.
(99) Wiaderek, K. M.; Cox, J. A. *Electrochim. Acta* **2011**, *56*, 3537-3542.
(100) Chakraborty, S.; Raj, C. R. *Biosens. Bioelectron.* **2009**, *24*, 3264-3268.
(101) Norouzi, P.; Faridbod, F.; Larijani, B.; Ganjali, M. R. *Int. J. Electrochem. Sci.* **2010**, *5*, 1213-1224.
(102) Hu, J.; Wisetsuwannaphum, S.; Foord, J. S. *Faraday Discussions* **2014**, *172*, 457-472.
(103) Zhang, Y.; Suryanarayanan, V.; Nakazawa, I.; Yoshihara, S.; Shirakashi, T. *Electrochim. Acta* **2004**, *49*, 5235-5240.
(104) Wyszecka-Kaszuba, E.; Warowna-Grzeskiewicz, M.; Fijalek, Z. *J Pharmaceut Biomed* **2003**, *32*, 1081-1086.
(105) Ozkan, S. A. *Electroanalytical Methods in Pharmaceutical Analysis and Their Validation*; HNB publishing: New York, USA, 2012, p 350.
(106) Gupta, V. K.; Jain, R.; Radhapyari, K.; Jadon, N.; Agarwal, S. *Anal. Biochem.* **2011**, *408*, 179-196.
(107) Xin, M.; Lin, H.; Yang, J.; Chen, M.; Ma, X.; Liu, J. *Electroanal* **2014**, n/a-n/a.
(108) Eisele, A. P. P.; Clausen, D. N.; Tarley, C. R. T.; Dall'Antonia, L. H.; Sartori, E. R. *Electroanal* **2013**, *25*, 1734-1741.
(109) Tajik, S.; Taher, M. A.; Beitollahi, H. *Electroanal* **2014**, n/a-n/a.
(110) Cao, X. Q.; Wang, B. C.; Su, Q. *J. Electroanal. Chem.* **1993**, *361*, 211-214.
(111) Kokkinidis, G.; Jannakoudakis, P. D. *J. Electroanal. Chem. Interfacial Electrochem.* **1981**, *130*, 153-162.
(112) Li, J.; Xie, H. Q.; Chen, L. F. *Sens. Actuator B-Chem.* **2011**, *153*, 239-245.
(113) Wakerley, D.; Güell, A. G.; Hutton, L. A.; Miller, T. S.; Bard, A. J.; Macpherson, J. V. *Chem. Commun.* **2013**, *49*, 5657-5659.
(114) Golabi, S. M.; Zare, H. R. *Electroanal* **1999**, *11*, 1293-1300.
(115) Meites, L. *Handbook of Analytical Chemistry*, 1st ed.; McGraw-Hill Inc.,US, 1963; Vol. 96, p 358.
(116) Zhang, R.; Liu, L.; Li, Y. H.; Wang, W. Y.; Li, R. F. *Int J Electrochem Sc* **2015**, *10*, 2355-2369.
(117) Michlmayr, M.; Sawyer, D. T. *J. Electroanal. Chem.* **1969**, *23*, 375-385.
(118) Antoniadou, S.; Jannakoudakis, A. D.; Theodoridou, E. *Synth. Met.* **1989**, *30*, 295-304.
(119) Alvarez-Ruiz, B.; Gomez, R.; Orts, J. M.; Feliu, J. M. *J Electrochem Soc* **2002**, *149*, D35-D45.
(120) Aldous, L.; Compton, R. G. *Phys Chem Chem Phys* **2011**, *13*, 5279-5287.
(121) Karp, S.; Meites, L. *J Am Chem Soc* **1962**, *84*, 906-912.
(122) Álvarez-Ruiz, B.; Gómez, R.; Orts, J. M.; Feliu, J. M. *J Electrochem Soc* **2002**, *149*, D35-D45.
(123) Wang, G.; Zhang, C.; He, X.; Li, Z.; Zhang, X.; Wang, L.; Fang, B. *Electrochim Acta* **2010**, *55*, 7204-7210.
(124) Hammer, B.; Norskov, J. K. *Nature* **1995**, *376*, 238-240.
(125) Hosseini, M.; Momeni, M. M.; Faraji, M. *Journal of Molecular Catalysis A: Chemical* **2011**, *335*, 199-204.
(126) Xu, J. S.; Granger, M. C.; Wang, J.; Chen, Q. Y.; Witek, M. A.; Hupert, M. L.; Hanks, A.; Swain, G. M.; Sakaguchi, I.; Nishitani-Gamo, M.; Ando, T. *Structure-reactivity studies at boron-doped single and polycrystalline diamond thin-film electrodes: Relationship to applications in electroanalysis*; Electrochemical Society Inc: Pennington, 2000; Vol. 99, p 403-415.
(127) Sun, H.; Dong, L.; Yu, H.; Huo, M. *Russ. J. Electrochem.* **2013**, *49*, 883-887.

(128) Devasenathipathy, R.; Mani, V.; Chen, S.-M. *Talanta* **2014**, *124*, 43-51.
(129) Xu, F.; Zhao, L. J.; Zhao, F. Q.; Deng, L. Z.; Hu, L.; Zeng, B. Z. *Int J Electrochem Sc* **2014**, *9*, 2832-2847.
(130) Yin, Z.; Liu, L.; Yang, Z. *J. Solid State Electrochem.* **2011**, *15*, 821-827.
(131) Kocak, S.; Aslisen, B. *Sensor Actuat B-Chem* **2014**, *196*, 610-618.
(132) Lyutov, V.; Tsakova, V. *Journal of Electroanalytical Chemistry* **2011**, *661*, 186-191.
(133) Sivasubramanian, R.; Sangaranarayanan, M. V. *Sensor Actuat B-Chem* **2015**, *213*, 92-101.
(134) Yan, L.; Bo, X.; Zhu, D.; Guo, L. *Talanta* **2014**, *120*, 304-311.
(135) Chang, G. H.; Luo, Y. L.; Lu, W. B.; Hu, J. M.; Liao, F.; Sun, X. P. *Thin Solid Films* **2011**, *519*, 6130-6134.
(136) Ding, W.; Wu, M.; Liang, M. L.; Ni, H. M.; Li, Y. *Anal. Lett.* **2015**, *48*, 1551-1569.
(137) Panchompoo, J.; Aldous, L.; Downing, C.; Crossley, A.; Compton, R. G. *Electroanal* **2011**, *23*, 1568-1578.
(138) Lee, K. K.; Loh, P. Y.; Sow, C. H.; Chin, W. S. *Biosensors and Bioelectronics* **2013**, *39*, 255-260.
(139) Yang, Y. J.; Li, W.; Wu, X. *Electrochim Acta* **2014**, *123*, 260-267.
(140) Oukil, D.; Benhaddad, L.; Makhloufi, L.; Aitout, R.; Saidani, B. *Sens. Lett.* **2013**, *11*, 395-404.
(141) Yi, Q.; Niu, F.; Yu, W. *Thin Solid Films* **2011**, *519*, 3155-3161.
(142) Kondratiev, V. V.; Babkova, T. A.; Tolstopjatova, E. G. *J. Solid State Electrochem.* **2013**, *17*, 1621-1630.
(143) Hosseini, H.; Ahmar, H.; Dehghani, A.; Bagheri, A.; Fakhari, A. R.; Amini, M. M. *Electrochim Acta* **2013**, *88*, 301-309.
(144) Jeevagan, A. J.; John, S. A. *RSC Adv.* **2013**, *3*, 2256-2264.
(145) Benvidi, A.; Kakoolaki, P.; Zare, H. R.; Vafazadeh, R. *Electrochim Acta* **2011**, *56*, 2045-2050.
(146) Xin, M.; Lin, H. L.; Yang, J. M.; Chen, M. N.; Ma, X. Y.; Liu, J. Y. *Electroanal* **2014**, *26*, 2216-2223.
(147) Ojani, R.; Safshekan, S.; Raoof, J.-B. *J. Solid State Electrochem.* **2014**, *18*, 779-783.
(148) Abdul Aziz, M.; Kawde, A.-N. *Talanta* **2013**, *115*, 214-221.
(149) Hutton, L. A.; O'Neil, G. D.; Read, T. L.; Ayres, Z. J.; Newton, M. E.; Macpherson, J. V. *Anal Chem* **2014**, *86*, 4566-4572.
(150) Meng, L.; Iacobini, J. G.; Joseph, M. B.; Macpherson, J. V.; Newton, M. E. *Faraday Discussions* **2014**, *172*, 421-438.
(151) Hutton, L. A.; Vidotti, M.; Iacobini, J. G.; Kelly, C.; Newton, M. E.; Unwin, P. R.; Macpherson, J. V. *Anal Chem* **2011**, *83*, 5804-5808.
(152) O'Neil, G. D.; Newton, M. E.; Macpherson, J. V. *Anal Chem* **2015**, *87*, 4933-4940.
(153) Bitziou, E.; Joseph, M. B.; Read, T. L.; Palmer, N.; Mollart, T.; Newton, M. E.; Macpherson, J. V. *Anal Chem* **2014**, *86*, 10834-10840.
(154) Compton, R. G.; Unwin, P. R. *Journal of Electroanalytical Chemistry and Interfacial Electrochemistry* **1986**, *205*, 1-20.
(155) Nakayama, Y.; Boucher, R. F. *Introduction to fluid mechanics*; Arnold; J. Wiley & Sons: London, New York, 1999, p 308.
(156) Bae, A. J.; Beta, C.; Bodenschatz, E. *Lab Chip* **2009**, *9*, 3059-3065.
(157) Snowden, M. E.; King, P. H.; Covington, J. A.; Macpherson, J. V.; Unwin, P. R. *Anal Chem* **2010**, *82*, 3124-3131.
(158) Nakayama, Y.; Boucher, R. F. *Introduction to fluid mechanics*; J. Wiley & Sons: London, 1999, p xii, 308 p.
(159) Snowden, M. E.; Unwin, P. R.; Macpherson, J. V. *Electrochemistry Communications* **2011**, *13*, 186-189.

(160) Růžička, J.; Hansen, E. H. *Anal. Chem.* **2000**, *72*, 212A-217A.
(161) de Castro, M. D. L.; Valcárcel, M. *J. Pharm. Biomed. Anal.* **1989**, *7*, 1291-1300.
(162) Pungor, E.; Feher, Z.; Nagy, G. *Anal. Chim. Acta* **1970**, *51*, 431-436.
(163) Růžička, J.; Hansen, E. H. *Flow injection analysis*, 2nd ed.; J. Wiley: New York, 1988, p 498.
(164) Tzanavaras, P. D.; Themelis, D. G. *Anal. Chim. Acta* **2007**, *588*, 1-9.
(165) Trojanowicz, M. *Anal. Chim. Acta* **2009**, *653*, 36-58.
(166) Felix, F. S.; Angnes, L. *J. Pharm. Sci.* **2010**, *99*, 4784-4804.
(167) Hartwell, S. K.; Kehling, A.; Lapanantnoppakhun, S.; Grudpan, K. *Anal. Lett.* **2013**, *46*, 1640-1671.
(168) Arab Chamjangali, M.; Goudarzi, N.; Ghochani Moghadam, A.; Amin, A. H. *Spectrochimica Acta Part A: Molecular and Biomolecular Spectroscopy* **2015**, *149*, 580-587.
(169) Grudpan, K.; Jakmunee, J.; Sooksamiti, P. *Talanta* **1999**, *49*, 215-223.
(170) Mahbub, P.; Zakaria, P.; Guijt, R.; Macka, M.; Dicinoski, G.; Breadmore, M.; Nesterenko, P. N. *Talanta* **2015**, *143*, 191-197.
(171) Miro, M.; Estela, J. M.; Cerda, V. *Curr. Anal. Chem.* **2005**, *1*, 329-343.
(172) Burguera, J. L.; Burguera, M.; Rondón, C.; Carrero, P.; Brunetto, M. R.; Petit de Peña, Y. *Talanta* **2000**, *52*, 27-37.
(173) Herold, M.; May, I.; Nicolas, A. *Eur. J. Hosp. Pharm.-Sci. Pract.* **2015**, *22*, 46-50.
(174) Lima Vaz, M. F.; de Oliveira, J. V. F.; Cassella, R. J.; Pacheco, W. F. *Luminescence* **2015**, *30*, 337-342.
(175) Vanderslice, J. T.; Stewart, K. K.; Rosenfeld, A. G.; Higgs, D. J. *Talanta* **1981**, *28*, 11-18.
(176) van der Linden, W. E. *TrAC Trends in Analytical Chemistry* **1982**, *1*, 188-191.
(177) Taylor, G. *Dispersion of Soluble Matter in Solvent Flowing Slowly through a Tube*, 1953; Vol. 219, p 186-203.
(178) Aris, R. *On the Dispersion of a Solute in a Fluid Flowing through a Tube*, 1956; Vol. 235, p 67-77.
(179) Ananthakrishnan, V.; Gill, W. N.; Barduhn, A. J. *AIChE Journal* **1965**, *11*, 1063-1072.
(180) Stewart, K. K.; Beecher, G. R.; Hare, P. E. *Analytical Biochemistry* **1976**, *70*, 167-173.
(181) Růžička, J.; Hansen, E. H. *Anal. Chim. Acta* **1978**, *99*, 37-76.
(182) van der Linden, W. E. *TrAC Trends in Analytical Chemistry* **1987**, *6*, 37-40.
(183) DeLon Hull, R.; Malick, R. E.; Dorsey, J. G. *Anal. Chim. Acta* **1992**, *267*, 1-24.
(184) Růžička, J.; Hansen, E. H. *Anal. Chim. Acta* **1980**, *114*, 19-44.
(185) Pike, D.; Kapur, N.; Millner, P.; Stewart, D. *Sensors* **2012**, *13*, 58.
(186) Stone, D. C.; Tyson, J. F. *Analyst* **1987**, *112*, 515-521.
(187) Stone, D. C.; Tyson, J. F. *Analyst* **1987**, *112*, 515-521.

Chapter 2 Experimental

2.1 Chemicals and Materials

All aqueous solutions used within this thesis were prepared from Milli-Q (18.2 MΩ cm^{-1} resistivity at 25°C, Millipore). All solids were weighed out using a four figure analytical balance (Sartorius, A2008) and pH measurements were carried out with a pH meter (PHM201 Portable pH meter, Radiometer, Copenhagen). The chemicals and materials used within this thesis are given in Tables 2.1 and 2.2 respectively:

Chemical	Details	Supplier
Potassium hexachloroplatinate(IV) (PtK_2Cl_6)	99.99%	Sigma Aldrich (UK)
Potassium gold (III) chloride ($KAuCl_4$)	99.995%	Sigma Aldrich (UK)
Sodium perchlorate monohydrate ($NaClO_4.H_2O$)	99%	Sigma Aldrich (UK)
Phosphate buffer solution (PBS)	pH 7.2	Sigma Aldrich (UK)
Hydrazine sulphate (HZ)	99%	Sigma Aldrich (UK)
Promazine hydrochloride (PZ)	99%	Sigma Aldrich (UK)
Acetaminophen (ACM)	98%	Sigma Aldrich (UK)
Potassium nitrate (KNO_3)	99%	Sigma Aldrich (UK)
Sodium dihydrogen orthophosphate (NaH_2PO_4)	99.1%	Fisher Scientific (UK)
Ferrocene methyltrimethylammonium hexafloruophosphate ($FcTMA^+.PF_6$)	98%	Synthesised in house[1]
Sodium phosphate dibasic heptahydride ($Na_2HPO_4.7H_2O$)	98%	Sigma Aldrich (UK)
Sodium hydroxide (NaOH)	98%	Sigma Aldrich (UK)
Sulphuric acid (H_2SO_4)	≥ 95% purity	Sigma Aldrich (UK)

Methacrylate based photoactive resin	(R11)	EnvisionTec (UK)
High temperature resin	HTM140v2	EnvisionTec (UK)
Paraffin oil		MP Biomedicals SAS (UK)
Acetonitrile	99.99%	Fisher Scientific (UK)
Ethanol	99.8%	Sigma Aldrich (UK)
Acetone	99%	Sigma Aldrich (UK)
Toluene	99.99%	Fisher Scientific (UK)
Dodecane	99%	Sigma Aldrich (UK)
Tertrahydrofuran	99.99%	Fisher Scientific (UK)
Dimethyl sulphoxide	99%	Fisher Scientific (UK)
Butan-1-ol	99.96%	Fisher Scientific (UK)
Ethyl acetate	99.9%	Sigma Aldrich (UK)
Hydrazine hydrate	99.9%	Acros Organics (UK)
Silicon elastromer base		DOW corning (UK)
Silicon elastromer curing agent		DOW corning (UK)

Table 2.1 Chemicals used within this thesis as well as purity and supplier.

Material	**Details**	**Supplier**
Conducting silver epoxy		RS components (UK)
Non-conductive epoxy		Robnor (UK)
Alumina Slurry	0.05 μm	Buehler (DE)
Electroanalysis grade boron doped diamond (BDD)[2]	Density = 3×10^{20} boron atoms cm^{-3}	Element Six, (UK)
Insulating diamond	Thermal grade	Element Six, (UK)
Saturated calomel electrode (SCE)		Cambria Scientific (UK)
Pt wire	1 mm diameter, 99.99%	Sigma Aldrich (UK)
Ag wire	1 mm diameter, 99.99%	Sigma Aldrich (UK)

PEEK tubing (polyetheretherketone)	0.18 mm ID	VICI (USA)
Teflon tubing	0.5 mm ID	VWR (NI)
Capillaries	2 mm OD, 1.16 mm ID	Harvard Apparatus (UK)
Teflon tape		Scientific Laboratory Supplies LTD (UK)
Polishing disk	Carbimet grit paper disc	Buehler, Germany

Table 2.2 Materials used within this thesis with corresponding suppliers, where ID is inner diameter.

2.2 Fabrication Techniques

2.2.1 Boron Doped Diamond Macrodisk Electrode Fabrication

All BDD electrodes were cut from wafer grown by Element Six Ltd. using microwave (MW) assisted CVD (500 μm thick, ~ 3×10^{20} boron atoms cm^{-3}, polished on both sides to nm roughness, EA grade, Element Six, Harwell, UK,). The BDD macrodisk electrodes were fabricated according to a previous procedure developed by Hutton *et. al*:[3] In short, a 1 mm diameter cylinder was lasered (E-355H-3-ATHI-O, Oxford Lasers, UK) from a freestanding BDD wafer (500 μm thick, with 1-3 nm surface roughness). The BDD cylinder was then acid cleaned in boiling conc. H_2SO_4, supersaturated with KNO_3 to remove any loose NDC. An ohmic contact[4] was made to the back of the electrode by sputtering (Edwards E606 sputter/evaporator) Ti (~20 nm) then Au (~300 nm), followed by annealing for four hours at 400 °C (MTF 12/25/400, Carbolite, UK).[5] The BDD disk was then sealed into a pulled glass capillary and polished back with a grit paper disc to expose the BDD. Exposure was confirmed with optical microscopy, then a contact was made through conducting epoxy and Cu wire to the back of the electrode. The resulting macrodisk BDD electrode is illustrated in Figure 2.1 below.

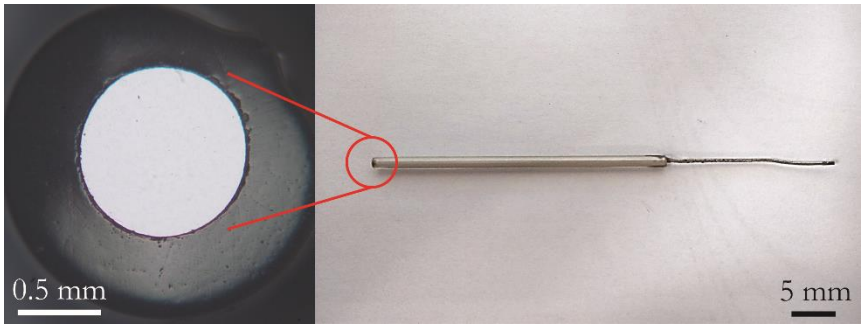

Figure 2.1: Pictures of a 1 mm diameter disk BDD macroelectrode, from top view (left) and side view (right).

2.2.2 All-Diamond Microband Electrode Fabrication

The all-diamond microband electrodes were fabricated according to the following procedure as illustrated in Figure 2.2. In short, a microstructure is lasered into a wafer (thermal grade, Element Six, Harwell, UK) of freestanding insulating diamond (Figure 2.2a. b) BDD (EA grade, Element Six, Harwell, UK) is then overgrown by MW-CVD to cover the surface c), before polishing back to reveal the inlaid structure d). Ohmic contacts can then be made by either top contacting e) or back contacting.[6] The former method is used for devices within this thesis. The electrode was then characterised by FE-SEM, solvent windows and continuous flow CV as described in chapter 4.

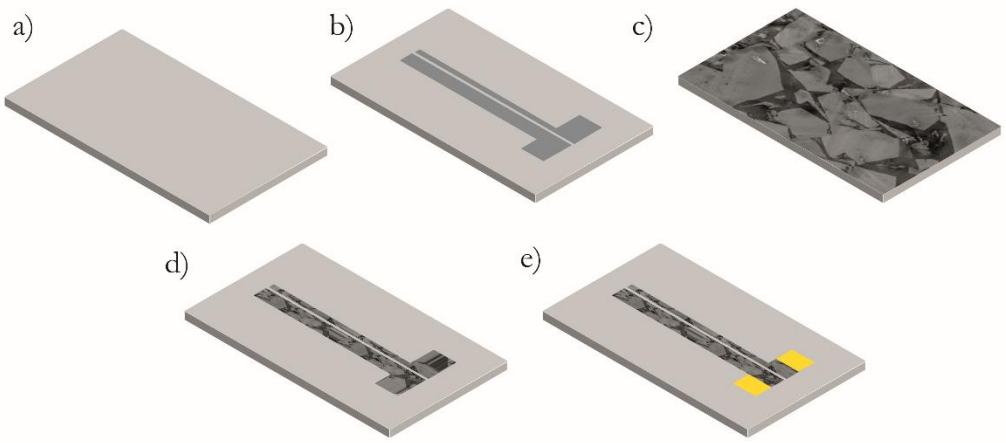

Figure 2.2: Fabrication route for all-diamond electrodes, a) insulating diamond, b) laser ablation, c) BDD overgrowth, d) polishing BDD layer and e) electrical contact to top face.[6]

2.2.3 Flow Injection Analysis Flow Cell Fabrication

The FIA channel flow cell was designed using SolidWorks (Dassault Systems, FR), and fabricated by photolithography using a Perfactory Mini (EnvisionTec, UK) and a methacrylate based photoactive resin. The flow cell was then clamped to the all diamond electrode in a two-part FIA setup. The channel dimensions were confirmed by continuous flow CV and interferometry (ContourGT, Bruker, UK). Design and optimisation of the flow cell is discussed in greater detail in chapter 4.

A piston pump (305, Gilson, USA) was used to drive the carrier phase, in conjunction with a manometric module (806, Gilson, USA) which served to dampen the modulations in flow rate from the pump. PEEK tubing (l = 12.5 cm, 0.18 mm ID) was used between the sample injector and flow cell and Teflon tubing (0.5 mm ID) at the flow cell outlet. The FIA setup was then completed with a manual sample injector (7725i, Rheodyne UK) utilising a 50 μL sample loop (PEEK, VICI, USA), as shown in Figure 2.3.

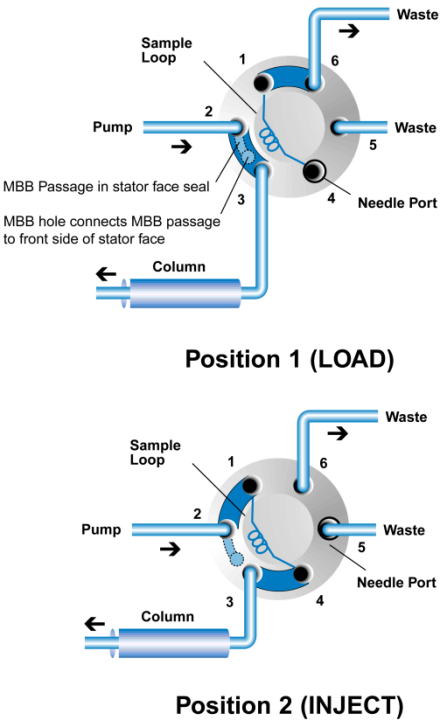

Figure 2.3: 6-port injection mechanism for FIA.[7]

2.2.4 Microfluidic Chip Fabrication

The droplet-microfluidics device used in chapter 5 (section 5.2.4.4) was fabricated as follows: An SU8-2100 photoresist (Microchem, Newton MA) was spin-coated onto a four inch silicon wafer (at 3000 rpm for 30 seconds) producing a ~100 μm thick film. The wafer was then transferred to a hot plate and heated from 15 °C up to 95 °C through ramping up 5 °C every ten minutes. After cooling to room temperature, a UV-mask aligner (SUSS MicroTec) was used to transfer a microfluidic channel design onto the photoresist, using a 365 nm Hg - UV lamp for 20 s. The wafer was then heated to 65 °C for ten minutes, then 95 °C for 30 minutes, followed by development with an EC solvent (Microposit, Rohm and Hass, Denmark) and washing with isopropyl alcohol, deionised water and drying with nitrogen gas.

This wafer was then used as a mold for fabrication of the microfluidics PDMS chip. A silicon elastomer base and silicon elastomer curing agent were mixed in a 10:1 ratio then after mixing, the mixture was degassed under vacuum in a desiccator. The mixture was then poured onto the wafer mould and after re-degassing under vacuum, was set at 70 °C for 3 hours in an oven. After setting, the microfluidic chip was cut from the wafer and set to the Au bands through an oxygen plasma asher.[8]

The Au bands used with these cells were fabricated by was spin coating S1818 (Rohm and Haas, Denmark) onto a glass microscope slide. Ti (10 nm) and Au (200 nm) were then sputtered onto the slide and any excess material lifted off through washing with acetone.

2.3 Electrochemical Techniques

A CHI potentiostat (CHI730A, CH Instruments Inc., TX.) was used for all stationary electrochemical measurements in chapters 3-5. An Ivium potentiostat (CompactStat, Alvatek, UK) was used for all hydrodynamic electrochemical experiments in chapters 4 and 5.

2.3.1 Nanoparticle Electrodeposition

Nanoparticle (NP) deposition was carried out by chronoamperometry with the following parameters for each system. The BDD macrodisk electrodes used in chapter 3 were functionalised with Pt NP by holding the electrode at – 1 V for 5 s, in a solution containing 1 mM potassium hexachloroplatinate(IV) in 0.1 M HCl.[3] Similarly, Au NP were deposited by holding the electrode at -0.9 V for 2 s in a solution of 1 mM potassium gold (III) chloride and 0.2 M sodium perchlorate monohydrate. Deposition of Pt NPs in chapter 5 for the all diamond microband electrode was achieved by holding the electrode at -1 V *vs* Ag/AgCl for 1.5 s in a solution of 1 mM PtK_2Cl_6 in 0.1 M H_2SO_4 The NP-BDD electrodes were then characterised by AFM, SEM and CV as described in chapters 3 and 5.

2.4 Non-Electrochemical techniques

2.4.1 Field Emission - Scanning Electron Microscopy

FE-SEM is an imaging technique used to study conductive surfaces and surface structures. In short, high energy electrons are produced under vacuum and accelerated (0.1 - 30 kV) towards a surface. The surface responds to this irradiation through several interactions, resulting in the emission of photons and electrons.[9] Two interactions are particularly important, namely; backscattered electrons and secondary electrons.

An elastic reflection of the incident beam results in backscattered electrons which are monitored by an in-lens detector. This is often used to study differences in conductivity in a surface e.g. higher doped grains of polycrystalline BDD adsorb more electrons and scatter less, appearing lighter in the final SEM image.[10] An inelastic collision results in the emission of secondary electrons. This is particularly useful for studying surface topography as different elements and different structures reflect different amounts of secondary electrons. As SEM allows for the recording of a range of image sizes (~ 3 by 3 μm up to

1 by 1 mm images), it is an ideal technique for studying large composite structures e.g. NP functionalised surfaces.

Two example images of the edge of a Pt NP-BDD microband electrode, imaged via the secondary electron detector (Figure 2.4a) and in-lens detector (Figure 2.4b) are shown below. Note that the polycrystalline BDD grain structure is clear on the secondary image only in the areas of Pt NP deposition (left side) as opposed to intrinsic diamond (right side), whereas the in-lens detector shows the underlying diamond grain structure throughout.

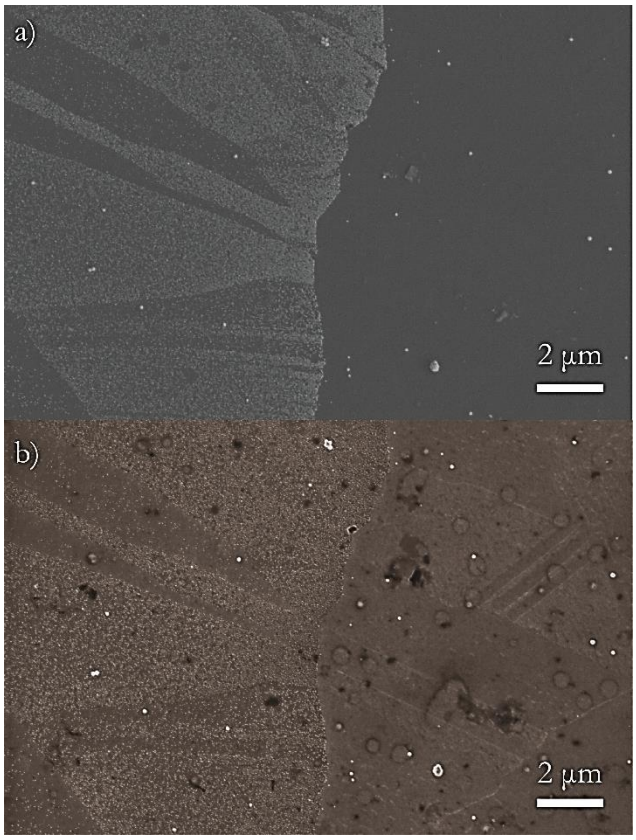

Figure 2.4: SEM images of a Pt NP-BDD microband electrode using the a) secondary electron detector and b) in-lens detector. The left side is Pt NP-BDD and the right is intrinsic diamond.

In this thesis, a high-resolution Supra 66 VP Field-emission SEM (FE-SEM, Zeiss, DE) was used in conjunction with an in-lens detector, 2 kV accelerating voltage and 4 mm working distance to record images of the unfunctionalised BDD microbands in chapter 4.

A secondary electron detector, 2 kV accelerating voltage and 5 mm working distance were used for images of Pt NPs in chapter 5. The Pt NP images were then analysed via MATLAB (R2013a, MathWorks, UK) to determine the NP density.

2.4.2 Atomic Force Microscopy

AFM is a scanning probe microscopy technique used to take high resolution images on the nanoscale.[11] In AFM, a microscopic tip attached to a cantilever is scanned across a sample to yield a topographical image of the surface as shown in Figure 2.5 below. The cantilever deflection is monitored via a beam-deflection method with a split photodiode detector. The tip position on the surface is controlled via a feedback mechanism of the cantilever deflection to a set of piezoelectric positioners attached to the tip.

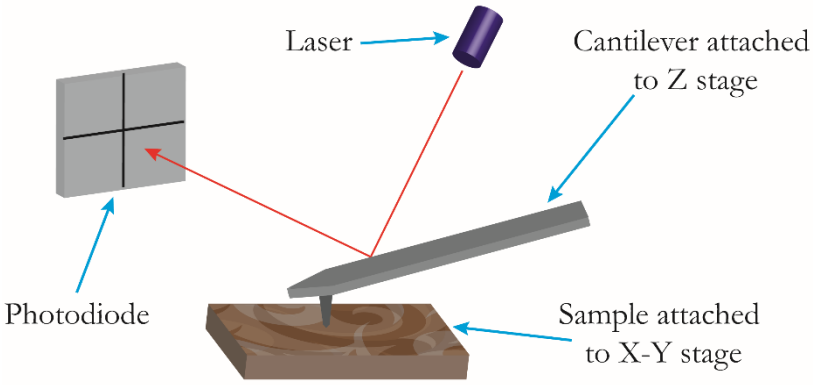

Figure 2.5: Schematic of AFM, the cantilever scans across the sample (through manipulation of the X-Y stage) and a laser is shone onto the cantilever and reflected to the photodiode.

Two modes of operation are common: contact mode and tapping mode. In contact mode, the tip is scanned across a surface by maintaining a constant force between the tip and surface via a constant cantilever defection, maintained by the piezoelectric positioners whilst scanning. In tapping mode, the tip is oscillated at its resonant frequency and the tip-surface distance is maintained via control of the oscillation dampening. The force on the tip is greatly reduced compared to contact mode, making tapping mode ideal for particularly hard surfaces like BDD, in which long term imaging can damage the tip.[12,13]

Also, tapping mode is useful for fragile surfaces such as NP, in order to avoid the displacement / dragging of NP across the surface.[3]

Unlike SEM, the resulting images are 3D (i.e. X, Y and Z) and typically much smaller (~200 by 200 nm up to 100 by 100 μm). AFM is thus ideal for visualization of fine surface structure, although ultimately the resolution is limited by the size of the tip (~200 nm). In this thesis, an Enviroscope AFM (Veeco, USA) with a NanoScope IV controller (Veeco, USA) was used in tapping mode, with RFESP tips (Veeco, USA) as described in chapter 3.

2.4.3 Interferometry

White light interferometry is a useful technique for measuring sample topography.[14] In short; a sample beam and reference beam are emitted from a broad spectrum light source towards the measurement sample. The interferometer then splits these beams and whilst the reference beam goes straight to a high resolution camera, the sample beam is reflected off the measurement sample, before reaching the camera. Recombination of these beams results in an interference pattern from the difference in path lengths, which is used to infer the sample topography.

Compared to AFM and FE-SEM, interferometry is non-destructive, non-contact and typically quicker, making it ideal for characterisation of the channel flow cells used in chapter 4 (Figure 4.9) using an a Bruker ContourGT interferometer (Bruker Nano Inc., USA).

2.5 References

(1) Lemay, S. G.; van den Broek, D. M.; Storm, A. J.; Krapf, D.; Smeets, R. M. M.; Heering, H. A.; Dekker, C. *Anal. Chem.* **2005**, *77*, 1911-1915.

(2) Diafilm EA: Enabling new electroanalytical applications. www.e6.com/sensors [accessed 23/06/14].

(3) Hutton, L.; Newton, M. E.; Unwin, P. R.; Macpherson, J. V. *Anal. Chem.* **2009**, *81*, 1023-1032.

(4) Tachibana, T.; Williams, B. E.; Glass, J. T. *Physical Review B* **1992**, *45*, 11975-11981.
(5) Wilson, N. R.; Clewes, S. L.; Newton, M. E.; Unwin, P. R.; Macpherson, J. V. *J. Phys. Chem. B* **2006**, *110*, 5639-5646.
(6) Joseph, M. B.; Bitziou, E.; Read, T. L.; Meng, L.; Palmer, N. L.; Mollart, T. P.; Newton, M. E.; Macpherson, J. V. *Anal. Chem.* **2014**, *86*, 5238-5244.
(7) Product Bulletin 209: Models 7725/7725i and 9725/9725i Sample Injectors for HPLC https://www.idex-hs.com/support/literature-downloads/operation-manuals [accessed 04/09/15].
(8) Bhattacharya, S.; Datta, A.; Berg, J. M.; Gangopadhyay, S. *Microelectromechanical Systems, Journal of* **2005**, *14*, 590-597.
(9) I. M. Watt. *The Principles and Practice of Electron Microscopy*, 2nd ed.; Cambridge University Press: Cambridge, 1997.
(10) Patten, H. V.; Meadows, K. E.; Hutton, L. A.; Iacobini, J. G.; Battistel, D.; McKelvey, K.; Colburn, A. W.; Newton, M. E.; Macpherson, J. V.; Unwin, P. R. *Angewandte Chemie International Edition* **2012**, *51*, 7002-7006.
(11) Binnig, G.; Quate, C. F.; Gerber, C. *Physical Review Letters* **1986**, *56*, 930-933.
(12) Putman, C. A. J.; Van der Werf, K. O.; De Grooth, B. G.; Van Hulst, N. F.; Greve, J. *Applied Physics Letters* **1994**, *64*, 2454-2456.
(13) Su, C.; Huang, L.; Kjoller, K.; Babcock, K. *Ultramicroscopy* **2003**, *97*, 135-144.
(14) Conor, O. M.; Martin, H.; Magali, B.; Russell, D.; Alan, M. *Measurement Science and Technology* **2003**, *14*, 1807.

Chapter 3 Hydrazine Detection in the Presence of an Active Pharmaceutical Ingredient in Stationary Solution

Electrochemical detection of the genotoxic impurity (GI); hydrazine (HZ) is demonstrated, in the presence of two important electrochemically active, inner sphere, active pharmaceutical ingredients (APIs); acetaminophen (ACM) and promazine (PZ). A metal nanoparticle (NP) functionalised polycrystalline boron-doped diamond (BDD) macroelectrode is utilised, characterised by atomic force microscopy (AFM). Importantly, it is demonstrated that the API electrochemical interferants can be selectively screened out, simply by changing the chemical identity of the metal NPs on the BDD electrode. HZ detection limits of 11.1 μM and 3.3 μM HZ in the presence of 1 mM ACM and PZ, respectively, are determined in quiescent solutions.

3.1 Introduction

GIs are compounds which modify DNA and are therefore harmful to human health (section 1.2.1).[1] A variety of chemicals exhibit genotoxic activity and are classified according to key functional groups, resulting in a list of structural alerts.[2] They occur in a pharmaceutical process as starting materials, intermediates, reaction bi-products or degradation products from the API.[3] The safe levels of exposure to GIs is given by the threshold of toxicological concern (TTC),[4] which stipulates an intake limit of 1.5 μg/day, equating to low parts per million (ppm) relative to the API. An important GI in the

pharmaceutical industry is the carcinogenic and mutagenic compound hydrazine (HZ).[5,6] HZ is also of great interest due to its use in fuel cells,[7] and as a chemical reducing agent.[8]

HZ and HZ-derivatives are class 1 GIs (known mutagens and carcinogens)[4] and are difficult to quantify due to their high volatility, high polarity, low molecular weight and lack of chromophore.[9] Therefore a variety of techniques are employed to detect HZ in the presence of the API such as GCMS, HPLC-UV and IC (section 1.2.2).[9,10] Liquid-liquid extraction and derivatization approaches are often used to enhance the detection sensitivity of HZ.[10-12] As the majority of these methods are time consuming and labour intensive - resulting in significant drug development costs[4,13] - new approaches are required that are simple and robust, such as electrochemical analysis.

HZ undergoes an irreversible, four electron electrooxidation, though the particulars of the mechanism and $E_{1/2}$ are strongly dependant on the chemical identity and crystallographic orientation of the metal electrode,[14,15] as well as the pH.[16] HZ has been previously studied electrochemically on a wide variety of electrodes (section 1.3.6), usually alone and very occasionally in the presence of equivalent concentrations of other species, normally as a recovery test.[17,18] The vast majority of APIs are electrochemically active,[19,20] thus HZ detection will be difficult if the API and HZ have similar $E_{1/2}$, particularly when the API is present in excess.

Herein, the quantitation of HZ in presence of two electrochemically active APIs; ACM and PZ is demonstrated (Figure 3.1) via linear sweep voltammetry (LSV) and differential pulse voltammetry (DPV). ACM is a common analgesic drug electrochemically oxidised in aqueous solution (pH ~7) via a two-electron transfer (ET) mechanism.[21] Electrochemical detection of ACM has also been demonstrated in pharmaceutical mixtures via differential pulse voltammetry (DPV)[22] and square-wave voltammetry on a BDD electrode.[23] PZ is an antipsychotic drug used to treat schizophrenia or to induce

spinal anaesthesia.[24] Whilst PZ has been studied by cyclic voltammetry (CV),[25] potentiometric titration[26] and differential-pulse polarography,[27] its electrochemical oxidation mechanism is still not fully understood. A BDD macroelectrode is used, functionalised with metal NP as a way to increase detection limits and reduce material costs.[28-30] Furthermore, by simply changing the NP identity, the sensor is shown to be tuneable to the GI-API system.

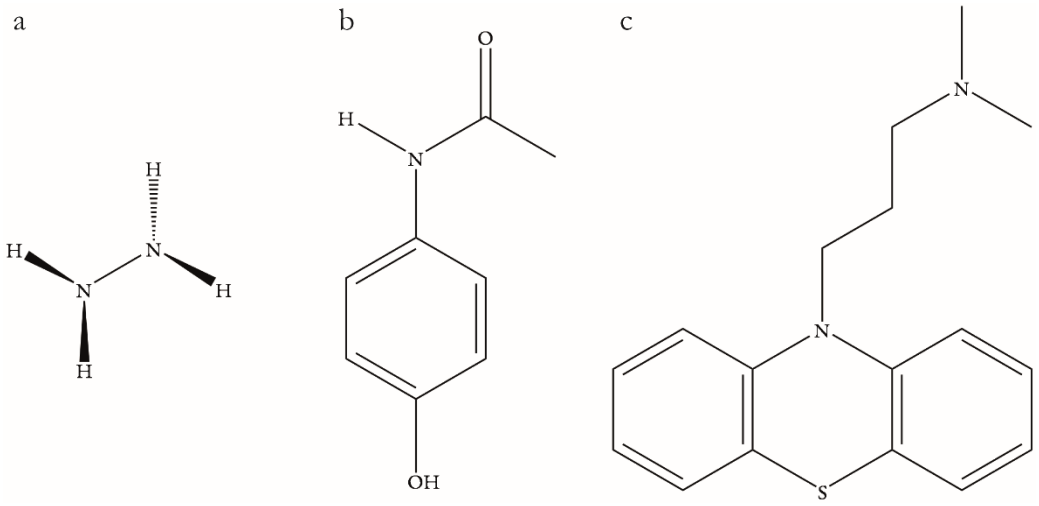

Figure 3.1: Structures of a) HZ, b) ACM and c) PZ.

3.2 Results and Discussion

3.2.1 Nanoparticle Functionalised Boron Doped Diamond

1 mm diameter macro disk BDD electrodes were fabricated using a procedure described by Hutton *et al.*[31] and described in section 2.2.1. Pt NPs were electrodeposited on BDD by holding the electrode at – 1 V for 5 s, in a solution containing 1 mM potassium hexachloroplatinate(IV) in 0.1 M HCl, as previously described in section 2.3.1.[31] Au NPs were electrodeposited from a solution of 1 mM potassium gold (III) chloride and 0.2 M sodium perchlorate monohydrate by holding the BDD electrode at -0.9 V for 2 s. Deposition conditions were chosen to ensure a high density of small NPs. NP

electrodeposition was characterised via tapping-mode atomic force microscopy (AFM), as shown in Figure 3.2 below.

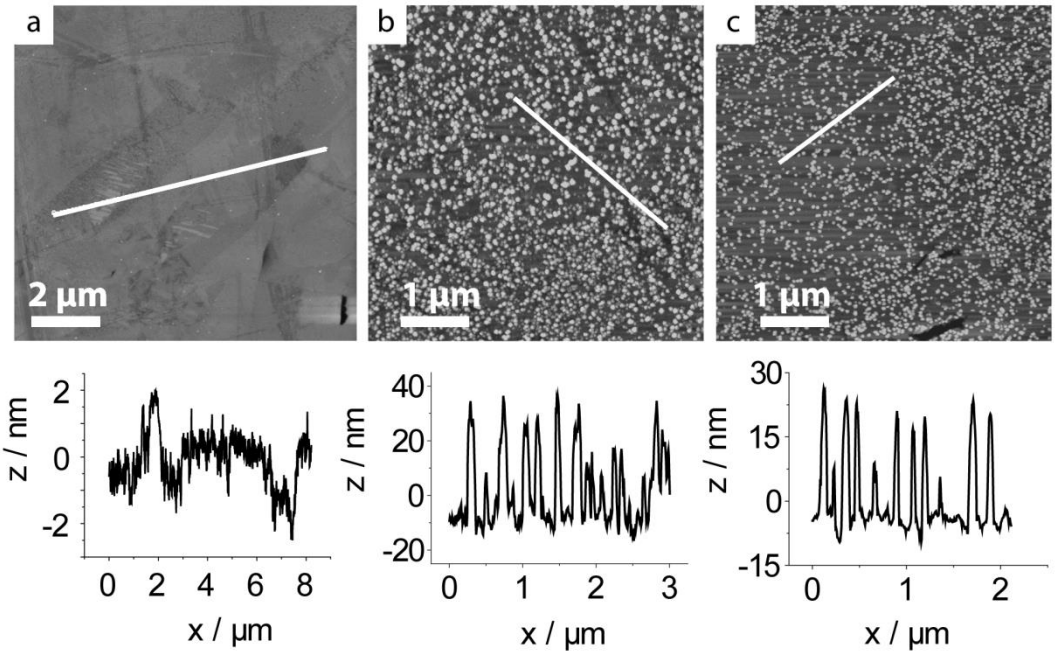

Figure 3.2: Tapping mode AFM images of a) bare BDD; b) electrodeposited Au NP-BDD and c) electrodeposited Pt NP-BDD electrodes with cross sectional height analysis of the three different surfaces in the zones indicated by the white lines.

The unfunctionalised BDD surface has a roughness of ~ nm (Figure 3.2a) and the heights of the NPs are in the range 10 - 40 nm for Au (Figure 3.2b) and 10 - 30 nm for Pt (Figure 3.2c).

As discussed in the introduction, the background signals and solvent window of metals such Au and Pt are much smaller than that of BDD (Figure 1.15). Hence an Au NP-BDD electrode should in theory have much lower background currents than a solid Au electrode, as shown in Figure 3.3 below. This bodes well for trace detection as a reduction in background size and variance will decrease the achievable detection limits.[32] Note, all voltammetry measurements in this chapter are quoted versus a saturated calomel reference electrode (SCE).

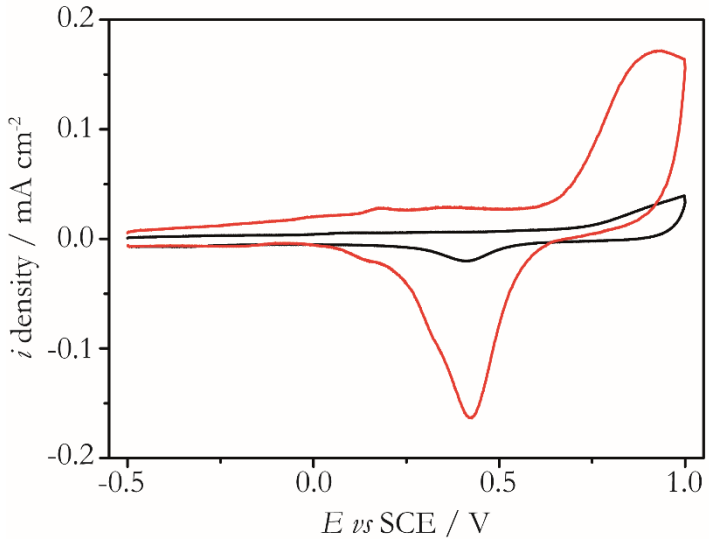

Figure 3.3: Background cyclic voltammetry (CV) in degassed 0.1 M KNO_3 at 0.1 V s^{-1} using (—) 2 mm diameter Au macroelectrode and Au NP deposited on a 1 mm diameter BDD macroelectrode (—).

3.2.2 Hydrazine Voltammetry

Initial studies focused on investigating HZ oxidation on different macroelectrodes (Pt, Au, BDD and a glassy carbon electrode- GCE) as shown in Figure 3.4 below.

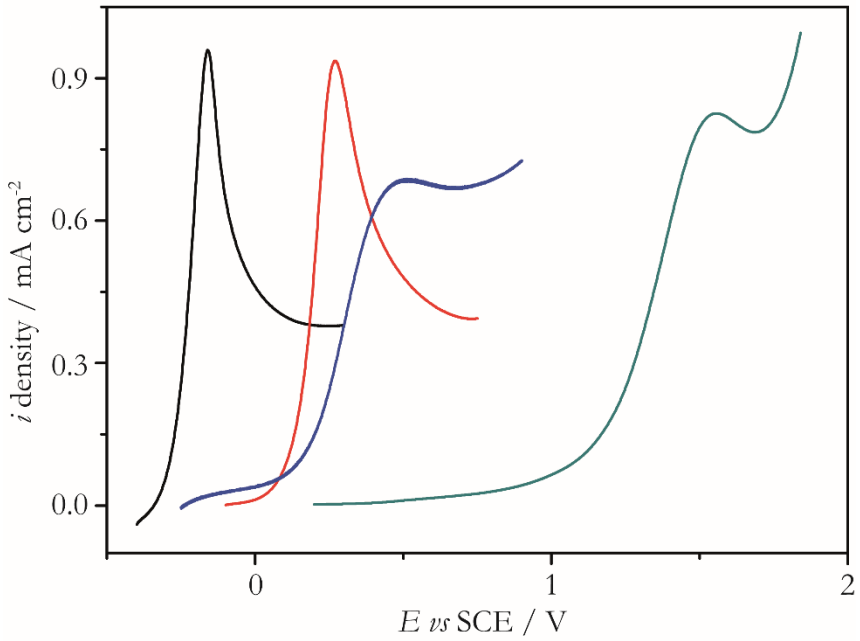

Figure 3.4: LSV (current density *vs* potential) with 1 mM HZ in 0.2 M PBS (pH 6.9), using Pt (2.0 mm diameter, —), Au (2.1 mm diameter, —), GCE (3.1 mm diameter, —), and BDD (1.0 mm diameter, —) macroelectrodes, at 0.1 V s^{-1}.

For HZ electrooxidation on BDD, ET is very kinetically hindered with the voltammetric signature occurring very close to the anodic solvent window for BDD (Peak potential E_p = +1.55 V). Furthermore, there are large shifts in the oxidative potential for HZ dependent on electrode material *i.e.* GCE (E_p = +0.51 V), Au (E_p = +0.27 V) and Pt (E_p = -0.16 V). The cathodic shift in $E_{1/2}$ for GC compared to BDD is as expected, based on the increased catalytic activity of the GC surface due to the reactive surface quinone groups.[33-35] Also, the shift from GC and BDD down to the Au and Pt electrodes, is due to improved catalytic activity of the metals.[36] Furthermore, the difference in HZ peak position for Au and Pt can be attributed to the different oxidation mechanisms on the two metals.[36-38] Finally, $E^{0'}$ for HZ is -0.23 and -0.33 V *vs* the natural hydrogen electrode in acidic and alkaline solutions respectively (-0.474 and -0.484 V respectively *vs* SCE).[39] Note other values have been quoted elsewhere e.g. -1.16 V *vs* NHE, on Pt, in alkaline solutions.[40] Experimentally, $E_{1/2}$ for HZ oxidation is usually at least 0.3 V positive of these values in dilute solutions,[41] due to the strong dependence of the mechanism and overpotential on the electrode material, pH,[16] electrode freshness,[42] crystalline facet of the surface[14,15,40] and even the presence of oxygen.[43] Hence it is difficult to compare peak positions between different studies / experiments without strict repetition of conditions.

These effects are also reflected in the case of Pt and Au NP functionalised BDD, as show in Figure 3.5. The HZ oxidation peak occurs at significantly lower overpotentials on the metal NP functionalised BDD (E_p (Pt) = -0.36 V, E_p (Au) = +0.29 V) electrodes compared to the bare BDD (E_p = +1.5 V). It is also interesting to note that the current densities are similar to the solid macroelectrodes (Figure 3.4). This suggests that the diffusion fields of the NP overlap during the voltammogram (Figure 1.18), such that linear diffusion prevails and the faradaic response is as that of a solid electrode. This, coupled

with the significantly reduced background signals compared to solid electrodes (Figure 3.3), shows the effectiveness of these electrodes for trace detection.

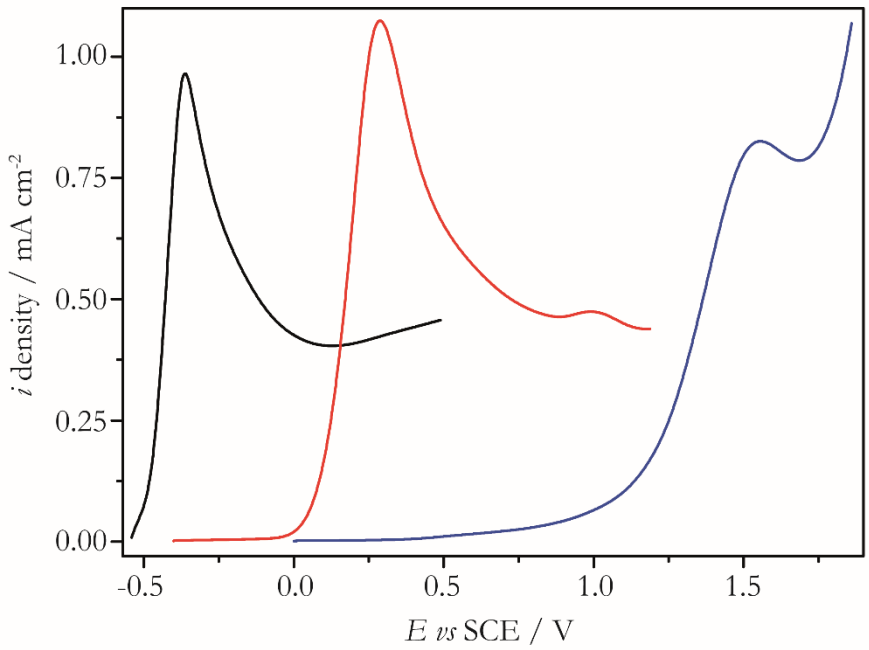

Figure 3.5: LSV of 1 mM HZ oxidation on (—) Pt NP-BDD, (—) Au NP-BDD and (—) bare 1 mm diameter BDD macrodisk electrode, recorded at a potential scan rate of 0.1 V s^{-1}.

3.2.2.1 Hydrazine Quantitation by Linear Sweep Voltammetry and Differential Pulse Voltammetry

HZ detection was further investigated over the concentration range 10 – 1000 µM at an Au NP-BDD electrode, using both LSV and DPV as shown in Figure 3.6 and 3.7 respectively. As discussed in the introduction (section 1.3.1.7), the DPV peak occurs at roughly the $E_{1/2}$ of the LSV. The peak current (i_p in LSV) and peak area (DPV) both scale with HZ concentration in a linear fashion, as shown in the respective Figure 3.6 and 3.7 insets. In LSV over the concentration range 10 - 1000 µM, the gradient was 8.3×10^{-3} ($\pm$ 0.13×10^{-3}) µA μM^{-1} with an R^2 of 0.999 (n = 5). For DPV, over the same concentration range, the gradient was 2.63×10^{-2} ($\pm$ 0.086×10^{-2}) µC μM^{-1} with an R^2 of 0.997 (n = 5). For DPV, the peaks were integrated to give the charge passed ($Q = i \times t$), as this gave a better linearity compared to the relationship of i_p *vs* concentration (in this case R^2 = 0.991

and sensitivity = 0.0016 μA μM^{-1}). Note, all DPV was executed with 5 mV incremental potential, 50 mV amplitude, 0.2 s pulse width and 0.4 s pulse period.

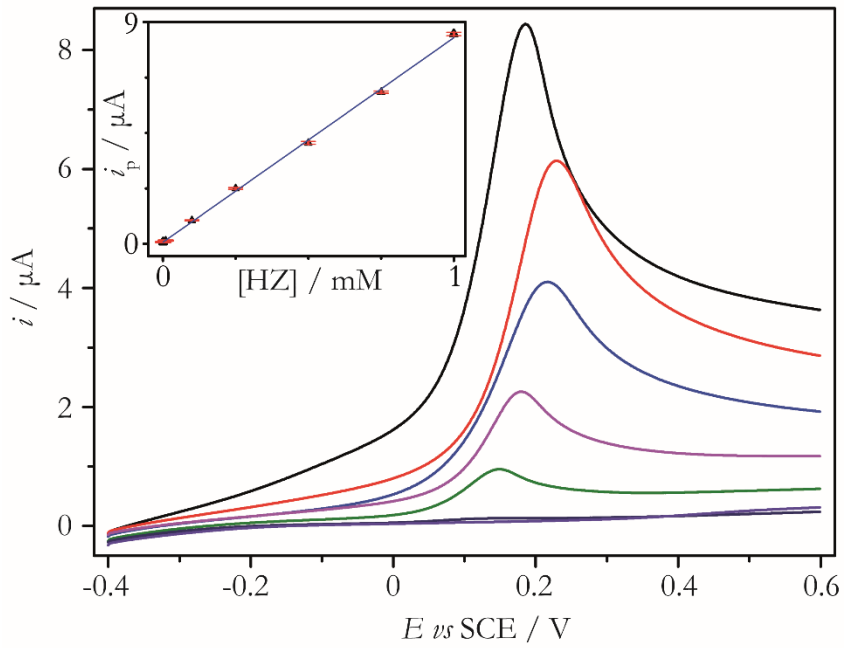

Figure 3.6: LSV with 0, 10, 100, 250, 500, 750 and 1000 μM HZ (n = 5 i.e. 5 repeats of each concentration), on an Au NP-BDD electrode at 0.1 V s^{-1}. Inset; limit of detection (LOD) plot of i_p vs HZ concentration, R^2 = 0.999, sensitivity = 0.0083 μA μM^{-1}, LOD = 1.32 μM.

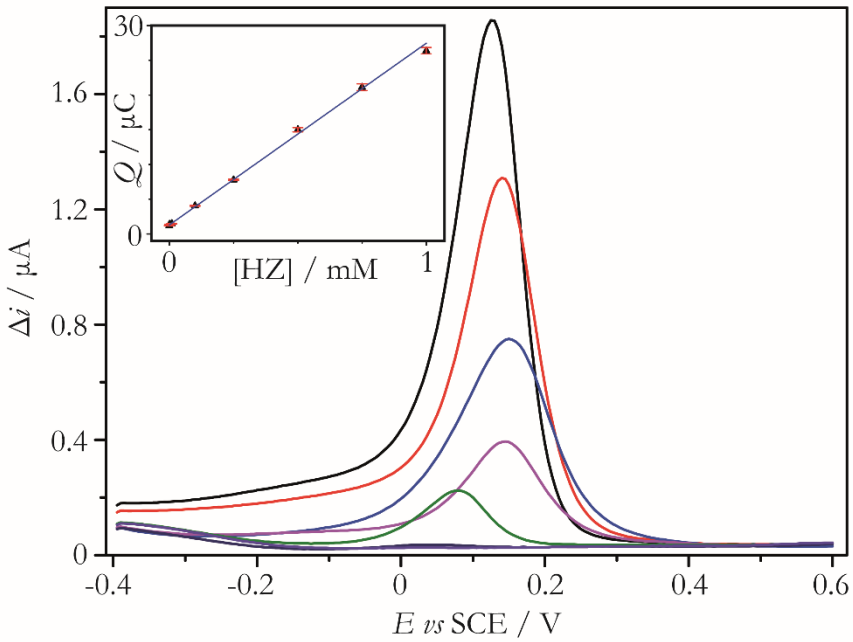

Figure 3.7: DPV with 0, 10, 100, 250, 500, 750 and 1000 μM HZ (n = 5), on an Au NP-BDD electrode. Inset; LOD plot of peak charge Q *vs* HZ concentration, R^2 = 0.997, sensitivity = 0.0263 μC mM^{-1}, LOD = 0.67 μM.

The limit of detection (LOD), is the concentration at which a measured signal is significantly different from the background response, to a pre-defined certainty e.g. 95%. It is given by,[32]

$$LOD = \bar{\mu} + 3\sigma \tag{3.1}$$

where $\bar{\mu}$ is the mean of the blank injection and σ is the standard deviation of the background response (with no faradaic species). Note, some authors quote a limit of quantitation whereby ten times the standard deviation is used for increased certainty (~99%). The mean background response and the standard deviation are taken from the current at the peak potential over several LSVs in the absence of HZ (n = 5). This results in an LOD value for LSV detection of HZ at an Au NP-BDD electrode of 1.32 μM. In the case of DPV, the mean background response is taken as the y-intercept of the LOD plot (Figure 3D) and the standard deviation is calculated from the variation in the area of several DPVs in the absence of HZ. This results in an LOD for DPV detection of HZ at an Au NP-BDD electrode of 0.67 μM. The lower LOD for DPV is attributed to the subtraction of background capacitive current contributions present in LSV, during the differential pulse (section 1.3.1.7). Thus, we focus further quantitative detection studies on DPV as it also provides the best method to both distinguish between two or more mediators and aid quantitative analysis of mixtures.[44,45]

3.2.3 Acetaminophen Voltammetry

As mentioned in the introduction, ACM undergoes a reversible 2 electron oxidation mechanism, shown below in Figure 3.8.[21] As the mechanism contains protons, it is no surprise that the $E_{1/2}$ and the reversibility (i.e. peak to peak separation) are dependent on the pH. In fact the mechanism becomes irreversible at strongly acidic or basic pH's.[21]

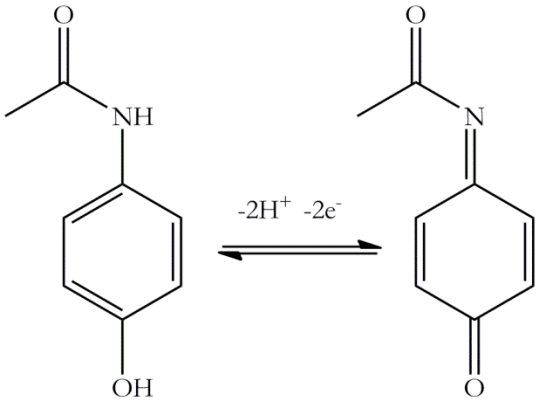

Figure 3.8: Overall oxidation mechanism for ACM at neutral pH.

ACM has been studied electrochemically by various authors in literature and varying overpotentials are observed for the oxidation, although these are dependent on the technique and working electrode used.[21-23,46-51] This suggests the mechanism may be inner sphere, which was tested by studying 1 mM ACM via LSV at pH 6.9, with Pt, Au, GCE and BDD electrodes, as shown in Figure 3.9.

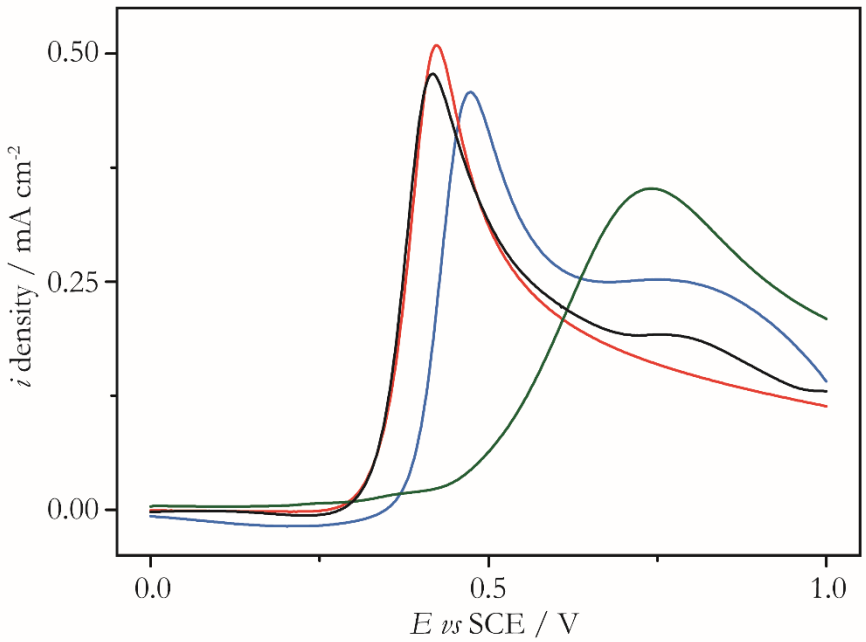

Figure 3.9: LSV (current density *vs* potential) with 1 mM ACM in 0.2 M PBS (pH 6.9), using Pt (2.0 mm diameter, ▬), Au (2.1 mm diameter, ▬), GCE (3.1 mm diameter, ▬), and BDD (1.0 mm diameter, ▬) macroelectrodes, at 0.1 V s^{-1}.

ET is found to be kinetically hindered (E_p = +0.74 V) on BDD compared to the other three electrodes, which show similar E_p values at +0.42 V (Pt), +0.38 V (GCE) and +0.37 V (Au). Finally, we can assess ACM by DPV on an Au NP-BDD electrode as shown in Figure 3.10. E_p for LSV and DPV are found at +0.51 V and +0.42 V, respectively. This data indicates that resolution of both the ACM and HZ (Figure 3.7) DPV peaks should be possible using an Au NP-BDD electrode, when both are present in solution.

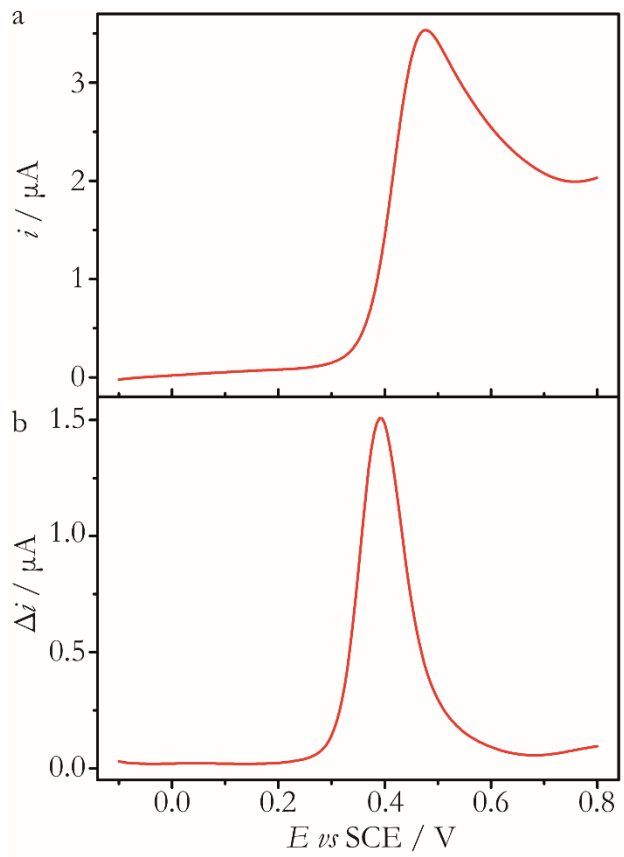

Figure 3.10: Oxidation of 1 mM ACM in 0.1 M PBS with an Au NP-BDD electrode via a) LSV and b) DPV

3.2.3.1 Determination of Hydrazine in the Presence of Acetaminophen

Figure 3.11 shows the resulting DPV response, recorded at an Au NP-BDD electrode in a pH 7.2 PBS solution, containing 1 mM ACM and varying concentrations of HZ (10 - 1000 μM). DPV is able to clearly resolve both the ACM peak and the concentration-varying HZ peaks. Although the DPV peak for the fixed concentration of ACM shifts

slightly in peak potential (+0.38 to +0.41 V) with HZ concentration, the area of the peak remains approximately constant (20.2 ± 0.6 μC). Importantly, for a fixed excess concentration of ACM, the area under the HZ DPV peaks varies in a linear fashion with concentration, making electrochemical quantification possible as shown in the Figure 3.11 inset.

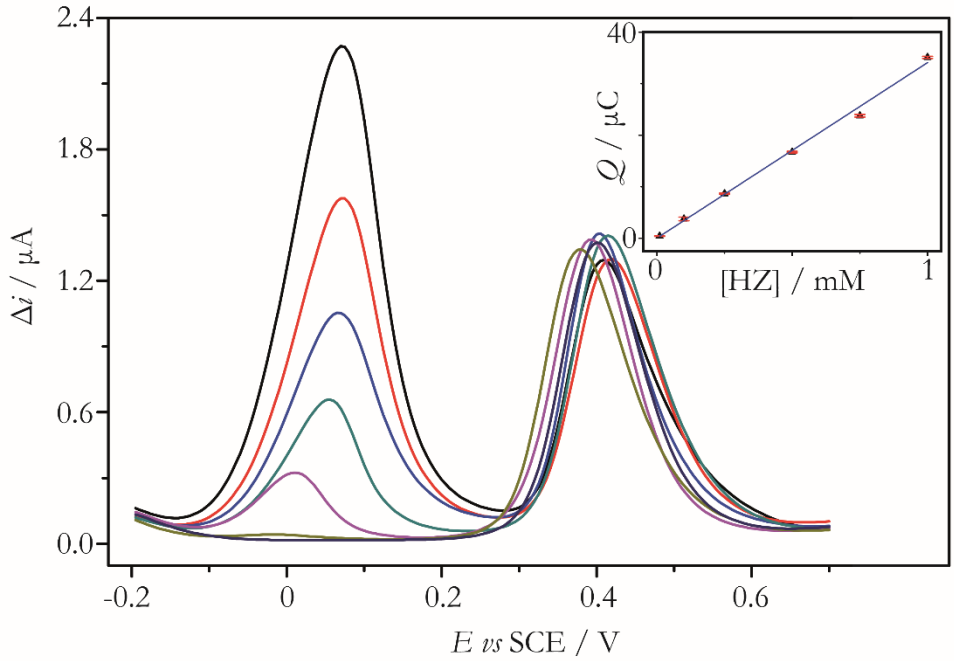

Figure 3.11: (a) DPV of 0, 10, 100, 250, 500, 750 and 1000 μM HZ in the presence of 1 mM ACM at an Au NP-BDD electrode, (b) plot of Q *vs* concentration (n = 5), sensitivity = 0.0034 μC μM^{-1}, R^2 = 0.998, LOD = 11.1 μM.

Note the area under the DPV peak for 1 mM ACM (18.8 μC) is lower than that for HZ (28.4 μC), by a factor of ~ 1.5. This is due to ACM oxidation being a two electron process,[21] compared to a four electron process for HZ.[52] The diffusion coefficients, *D*, for HZ and ACM were determined from the steady-state current recorded at a 25 μm diameter Pt disk ultramicroelectrode, measured to be 1.19×10^{-5} cm^2 s^{-1} and 4.12×10^{-6} cm^2 s^{-1} respectively, comparing favourably to literature values.[37,53] Over the concentration range 10 - 1000 μM, the slope of the graph is 3.40×10^{-2} μC mM^{-1}, with an R^2 of 0.998 (n = 5).

In the presence of 1 mM ACM, the LOD for HZ is determined as 11.10 μM. This value is larger than that obtained for HZ in the absence of ACM (0.67 μM), probably due to the increased background signal as a result of having an excess of API present in solution.

3.2.4 Promazine Voltammetry

PZ is another important electrochemically active API, which to date has not received a great deal of attention in the electrochemical literature. It has previously been studied by CV on Pt,[54] potentiometric titration on a polymer electrode,[55] differential-pulse polarography,[56] CV on a horseradish modified carbon composite electrode,[57] CV in ionic liquids,[58] CV on multiwalled carbon nanotubes[59,60] and flow injection analysis with electrochemical detection.[61] The PZ electrooxidation mechanism is not discussed in these studies, with the exception of reference 59 and 60, where PZ is used as a mediator for cysteamine and hydroxylamine oxidation respectively (though the mechanism is mentioned briefly as PZ is not the focus of the study).

Figure 3.12 shows the LSV (Figure 3.12a) and DPV (Figure 3.12b) signatures for the oxidation of 1 mM PZ at both a bare BDD (—) and an Au NP-BDD electrode (—). A slightly higher peak current is observed via LSV on Au NP-BDD than bare BDD, likely due to the greater background capacitive currents resulting from the presence of the Au NPs. Reduction of the background contributions via DPV results in the DPV response for both the bare BDD and Au NP-BDD being similar, peaking in current at 0.5 V. As this value is more positive than that of ACM (*ca* ~ 0.4 V), this suggests both HZ and PZ should be resolvable using an Au NP-BDD electrode. Moreover, the fact that the PZ DPV peak position does not change with the chemical identity of the electrode, in stark contrast to that observed for HZ (Figure 3.4) and ACM (Figure 3.9) on BDD and Au, suggests that PZ oxidation occurs through an outer sphere ET process.

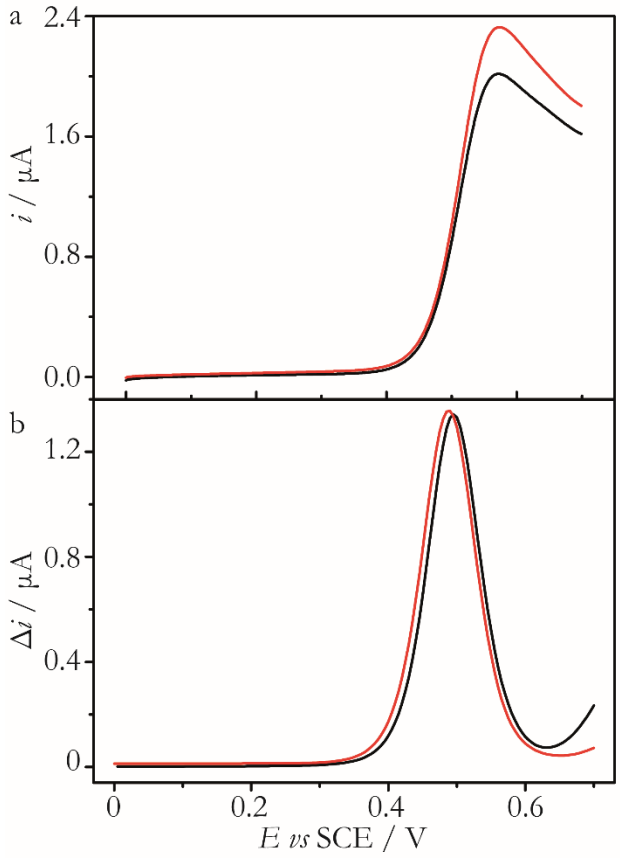

Figure 3.12: PZ oxidation in a solution containing 1 mM PZ in 0.1 M PBS, at a bare BDD (━) and an Au NP-BDD electrode (━) via a) LSV and b) DPV.

3.2.4.1 Determination of Hydrazine in the Presence of Promazine on Au NP

The DPV response for 1 mM PZ in the presence of varying concentrations of HZ (10 – 1000 μM) on an Au NP-BDD electrode is shown below in Figure 3.13. In contrast to HZ detection in the presence of ACM (Figure 3.11), it is no longer possible to resolve two distinct DPV peaks associated with the API and HZ. Instead, there is one dominant peak (E_p = +0.5 V), occurring in the same position as expected for PZ, with a small shoulder at a less positive potential (E_p = +0.2 V). With increasing HZ concentration, both the dominant peak and small shoulder only increase slightly in magnitude. This suggests that in the presence of PZ, at an Au NP-BDD electrode, HZ oxidation is either being retarded, or becoming less kinetically facile and shifting to more positive potentials, such that the HZ oxidation peak overlaps with that for PZ. However, even if the latter were true, the

increase in current would be expected to be much greater than that observed. We will return to an explanation of this phenomenon at the end of this chapter.

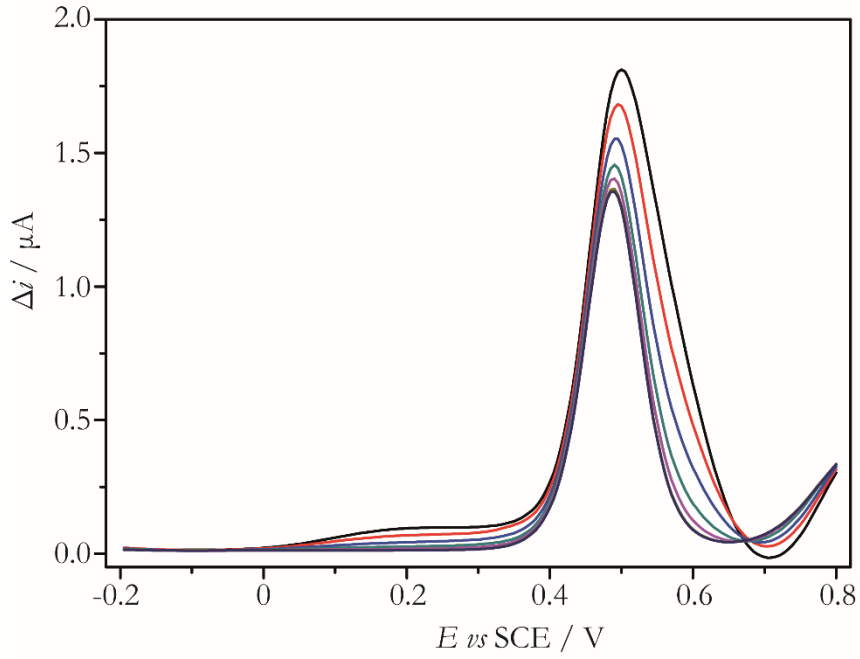

Figure 3.13: DPV of varying concentrations of HZ in the presence of 1 mM PZ, at an Au NP-BDD electrode with 0, 10, 100, 250, 500, 750 and 1000 μM HZ.

3.2.4.2 Determination of Hydrazine in the Presence of Promazine on Pt NP

Clearly, HZ and PZ cannot be independently resolved via this approach and quantification of HZ concentrations is thus not possible. As shown in Figure 3.4 and 3.5, HZ oxidation occurs at a significantly more negative potential on Pt than on Au. Thus switching metal NP identity may offer a route to separating out the electrochemical signatures of HZ and PZ oxidation. Therefore, HZ detection via DPV, in the presence of 1 mM PZ at a Pt NP-BDD electrode is shown below in Figure 3.14.

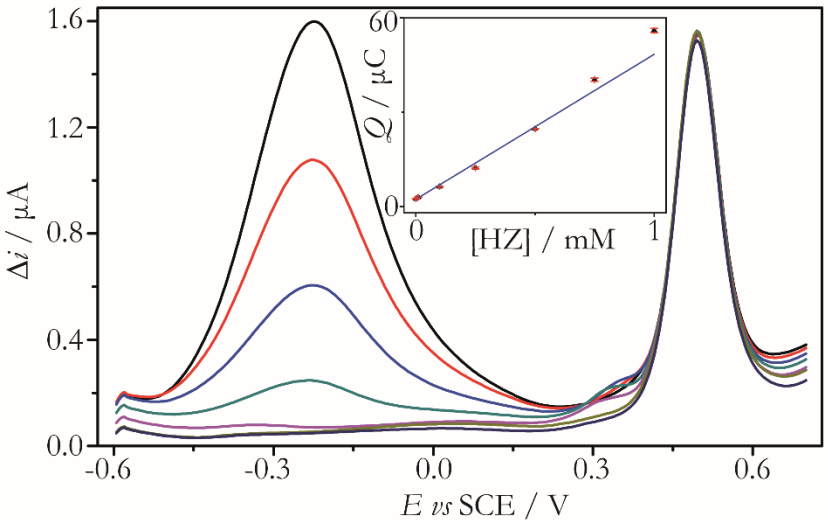

Figure 3.14: (a) DPV of varying concentrations of HZ in the presence of 1 mM PZ, at a Pt NP-BDD electrode with 0, 10, 100, 250, 500, 750 and 1000 μM HZ, inset; LOD plot of *Q vs* HZ concentration (n = 5), R^2 = 0.996, sensitivity = 0.0461 μC μM^{-1}.

Two peaks are now clearly identifiable. The PZ DPV peak position is at ~ 0.5 V in accordance with the observation that PZ electron transfer is occurring independently of the chemical identity of the surface. The DPV peak corresponding to HZ oxidation is now seen at -0.25 V, which represents a positive shift of *ca.* +0.25 V, compared to a HZ only solution, again indicating possible interactions between the PZ and HZ. The area of the 1 mM PZ peak (~21.7 μC) is smaller than that of the HZ peak (56.4 μC) by a factor of 2.6, which is suggestive of a two ET process, in agreement with oxidation of PZ by non-electrochemical methods.[62,63] A D for PZ was determined to be 2.65 × 10^{-6} cm^2 s^{-1} assuming a two electron process, which is similar to reported literature values.[64] However, as with HZ detection in the presence of ACM, the area of the HZ DPV peak (*ca* –0.25 V) scales linearly with concentration in the presence of PZ, as shown in the Figure 3.14 inset, with a sensitivity of 4.61 × 10^{-2} μC mM^{-1} and R^2 of 0.991 (n = 5). In the presence of 1 mM PZ, the LOD for HZ is calculated as 3.27 μM.

We can put these values into context with the TTC by converting the LOD into ppm with respect to the mass of API (section 1.2.1). Recall from equation (1.1),

$$\text{ppm} = \frac{\text{mass GI (mg)}}{\text{mass API (kg)}} \tag{3.1}$$

Thus the LOD for HZ determination with 1 mM ACM and 1 mM PZ are 2352 and 693 ppm respectively. Therefore, whilst the proposed method is able to clearly distinguish HZ from both ACM and PZ, the detection limits are insufficient in comparison to the TTC (~1 ppm) and other methods for HZ determination in the pharmaceutical industry.[13] The problem is likely surpassable by moving from quiescent solutions to hydrodynamic flow systems, where the enhanced mass transport should result in improved signal-to-noise ratios and thus smaller LOD.[65]

Now, let us return to question of why HZ determination in the presence of PZ is possible on Pt but not on Au. The lack of literature on PZ makes this a challenging question without further experiments. However it is seems likely that either i) PZ affects the HZ oxidation mechanism at the rate determining step (RDS), on Au but not on Pt, ii) PZ binds / adsorbs to Au blocking the surface for HZ oxidation or iii) HZ retards the PZ oxidation mechanism. Firstly, let us refresh ourselves on the HZ oxidation mechanisms on Au and Pt (section 1.3.6) as follows;

$$N_2H_5^+ \xrightarrow{RDS} N_2H_{3ads} + 2H^+ + e^- \tag{3.2}$$

$$N_2H_{3ads} \xrightarrow{FAST} N_2 + 3H^+ + 3e^- \tag{3.3}$$

for Au,[66] and

$$N_2H_5^+ \rightleftharpoons N_2H_{3ads} + 2H^+ + e^- \tag{3.4}$$

$$N_2H_{3ads} \xrightarrow{RDS} N_2H_{2ads} + H^+ + e^- \quad (3.5)$$

$$N_2H_{2ads} \xrightarrow{FAST} N_2H_{ads} + H^+ + e^- \quad (3.6)$$

$$N_2H_{ads} \rightarrow N_{2ads} + H^+ + e^- \quad (3.7)$$

$$N_{2ads} \rightarrow N_{2(g)} \quad (3.8)$$

for Pt.[67] Furthermore, it is likely that the PZ mechanism follows a similar path to that of oxidation by Cu[62] and Mn,[63] as shown in Figure 3.15 below. This mechanism is also corroborated by Rezaei *et al,*[59,60] who study PZ mediated hydroxylamine electrooxidation.

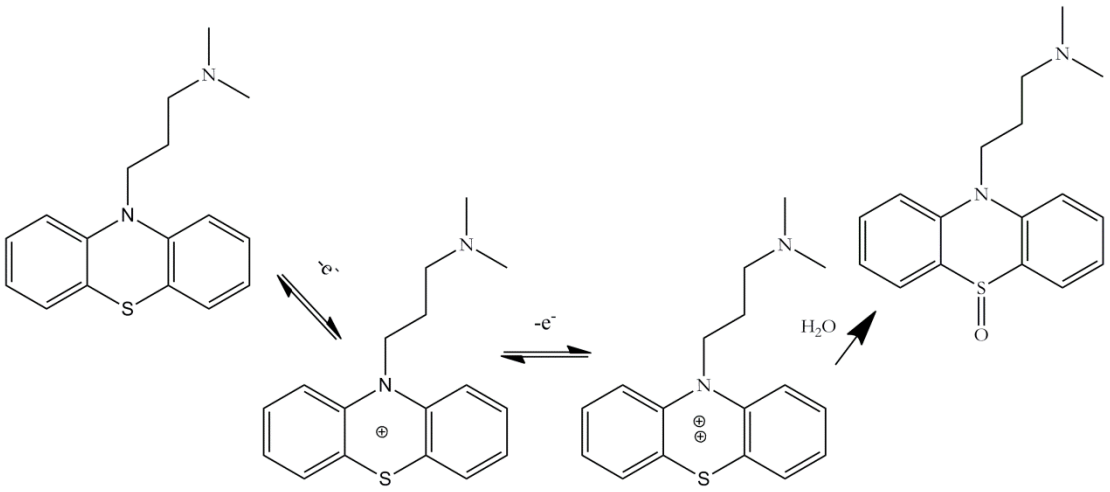

Figure 3.15: Possible electrooxidation mechanism for PZ.[59,60,62,63]

Option iii) can likely be discounted based on the consistent PZ peak height and position alone or on Au / Pt NP (Figure 3.12, 3.12 and 3.14). Option ii) is attractive in that sulphur is known to bind easily to Au (e.g. self-assembled monolayers).[68,69] Thus one could imagine that the difference in binding between PZ and Au or Pt could lead to PZ covering the surface and inhibiting the HZ oxidation. However this does not correlate with results suggesting PZ is an outer sphere species (Figure 3.12) or that HZ oxidation occurs before PZ. This leaves option i). The HZ oxidation mechanism RDS on Pt involves

an already bound Pt-N_2H_3 molecule (equation 3.5), whereas on Au, the metal-nitrogen bond forms in the RDS (equation 3.2). Thus it is possible that the PZ inhibits the RDS on Au in a way it cannot accomplish with Pt, as the HZ molecule is already bound. Clearly further experiments are required to understand this phenomenon; however a full investigation is beyond the scope of this study.

3.3 Conclusions

In this investigation, we have demonstrated electrochemical detection of the GI, HZ, in the presence of two electrochemically active APIs. For the case of HZ detection in the presence of excess ACM (1 mM), Au NP-BDD macrodisk electrodes were found to be suitable enabling a LOD for HZ of 11.10 μM using DPV. However, in the presence of PZ, the Au NP-BDD electrode was not able to sufficiently resolve the DPV peaks for both the GI and the API. As HZ oxidation is surface sensitive, this problem was solved by changing the chemical identity of the metal catalyst from Au to Pt, the latter which oxidises HZ at more negative potentials. Under these conditions, a LOD of 3.27 μM for HZ in the presence of excess PZ (1 mM) was obtained.

Compared to conventional techniques for HZ detection in pharmaceutical analysis, this electrochemical approach is inexpensive, fast and also requires no synthetic derivatization of the GI. By combining this measurement with hydrodynamic flow systems it will be possible to significantly improve detection limits, to reach the TTC required by the pharmaceutical industry for GI determination in the presence of an API.

3.4 References

(1) Robinson, D. I. *Org. Process Res. Dev.* **2010**, *14*, 946-959.
(2) Alzaga, R.; Ryan, R. W.; Taylor-Worth, K.; Lipczynski, A. M.; Szucs, R.; Sandra, P. *J. Pharm. Biomed. Anal.* **2007**, *45*, 472-479.

(3) Reddy, A. V. B.; Jaafar, J.; Umar, K.; Majid, Z. A.; Aris, A. B.; Talib, J.; Madhavi, G. *Journal of Separation Science* **2015**, *38*, 764-779.
(4) Müller, L.; Mauthe, R. J.; Riley, C. M.; Andino, M. M.; Antonis, D. D.; Beels, C.; DeGeorge, J.; De Knaep, A. G. M.; Ellison, D.; Fagerland, J. A.; Frank, R.; Fritschel, B.; Galloway, S.; Harpur, E.; Humfrey, C. D. N.; Jacks, A. S.; Jagota, N.; Mackinnon, J.; Mohan, G.; Ness, D. K.; O'Donovan, M. R.; Smith, M. D.; Vudathala, G.; Yotti, L. *Regul. Toxicol. Pharmacol.* **2006**, *44*, 198-211.
(5) Poso, A.; Vonwright, A.; Gynther, J. *Mutat. Res., Fundam. Mol. Mech. Mutagen.* **1995**, *332*, 63-71.
(6) Yu, X.; Zhang, J. *Chem. Eur. J.* **2012**, *18*, 12945 – 12949.
(7) Sanabria-Chinchilla, J.; Asazawa, K.; Sakamoto, T.; Yamada, K.; Tanaka, H.; Strasser, P. *J. Am. Chem. Soc.* **2011**, *133*, 5425-5431.
(8) Chen, H.; Wang, J. M.; Hong, X. C.; Zhou, H. B.; Dong, C. N. *Can. J. Chem.* **2012**, *90*, 758-761.
(9) Elder, D. P.; Snodin, D.; Teasdale, A. *J. Pharm. Biomed. Anal.* **2011**, *54*, 900-910.
(10) Kean, T.; Miller, J. H. M.; Skellern, G. C.; Snodin, D. *Pharmeuropa scientific notes* **2006**, *2*, 23-33.
(11) Carlin, A.; Gregory, N.; Simmons, J. *J. Pharm. Biomed. Anal.* **1998**, *17*, 885-890.
(12) Gyllenhaal, O.; Grönberg, L.; Vessman, J. *J. Chromatogr. A* **1990**, *511*, 303-315.
(13) Teasdale, A. *Genotoxic Impurities Stratagies for Identification and Control*; John Wiley & Sons: New Jersey, 2010, p 428.
(14) Kokkinidis, G.; Jannakoudakis, P. D. *J. Electroanal. Chem. Interfacial Electrochem.* **1981**, *130*, 153-162.
(15) Azorero, M. D. G.; Marcos, M. L.; Velasco, J. G. *Electrochim. Acta* **1994**, *39*, 1909-1914.
(16) Golabi, S. M.; Zare, H. R. *Electroanal* **1999**, *11*, 1293-1300.
(17) Yin, Z.; Liu, L.; Yang, Z. *J. Solid State Electrochem.* **2011**, *15*, 821-827.
(18) Sivasubramanian, R.; Sangaranarayanan, M. V. *Sensor Actuat B-Chem* **2015**, *213*, 92-101.
(19) Ozkan, S. A. *Electroanalytical Methods in Pharmaceutical Analysis and Their Validation*; HNB publishing: New York, USA, 2012, p 350.
(20) Gupta, V. K.; Jain, R.; Radhapyari, K.; Jadon, N.; Agarwal, S. *Anal. Biochem.* **2011**, *408*, 179-196.
(21) Li, Y.; Chen, S. M. *Int. J. Electrochem. Sci.* **2012**, *7*, 2175-2187.
(22) Khaskheli, A. R.; Fischer, J.; Barek, J.; Vyskocil, V.; Sirajuddin; Bhanger, M. I. *Electrochim. Acta* **2013**, *101*, 238-242.
(23) Eisele, A. P. P.; Clausen, D. N.; Tarley, C. R. T.; Dall'Antonia, L. H.; Sartori, E. R. *Electroanal* **2013**, *25*, 1734-1741.
(24) Chen, Y. W.; Chu, C. C.; Chen, Y. C.; Kan, C. D.; Wang, J. J. *Neurosci. Lett.* **2012**, *521*, 115-118.
(25) Petit, C.; Murakami, K.; Erdem, A.; Kilinc, E.; Borondo, G. O.; Liegeois, J. F.; Kauffmann, J. M. *Electroanalysis* **1998**, *10*, 1241-1248.
(26) Ayad, M. M.; Shalaby, A.; Abdellatef, H. E.; Elsaid, H. M. *Microchim. Acta* **2002**, *140*, 93-96.
(27) Belal, F.; El-Ashry, S. M.; Shehata, I. M.; El-Sherbeny, M. A.; El-Sherbeny, D. T. *Microchim. Acta* **2000**, *135*, 147-154.
(28) Kondratiev, V.; Babkova, T.; Tolstopjatova, E. *J. Solid State Electrochem.* **2013**, *17*, 1621-1630.
(29) Oukil, D.; Benhaddad, L.; Makhloufi, L.; Aitout, R.; Saidani, B. *Sens. Lett.* **2013**, *11*, 395-404.

(30) Dudin, P. V.; Snowden, M. E.; Macpherson, J. V.; Unwin, P. R. *ACS Nano* **2011**, *5*, 10017-10025.
(31) Hutton, L.; Newton, M. E.; Unwin, P. R.; Macpherson, J. V. *Anal. Chem.* **2009**, *81*, 1023-1032.
(32) Miller, J. N.; Miller, J. C. *Statistics and Chemometrics for Analytical Chemistry*, 5th ed.; Pearson Education Limited: London, 2005.
(33) McCreery, R. L. *Chemical Reviews* **2008**, *108*, 2646-2687.
(34) Guell, A. G.; Meadows, K. E.; Unwin, P. R.; Macpherson, J. V. *Phys Chem Chem Phys* **2010**, *12*, 10108-10114.
(35) Macpherson, J. V. *Phys Chem Chem Phys* **2015**, *17*, 2935-2949.
(36) Garcia, M. D.; Marcos, M. L.; Velasco, J. G. *Electroanalysis* **1996**, *8*, 267-273.
(37) Li, J.; Xie, H. Q.; Chen, L. F. *Sens. Actuator B-Chem.* **2011**, *153*, 239-245.
(38) Hammer, B.; Norskov, J. K. *Nature* **1995**, *376*, 238-240.
(39) Bard, A. J.; Parsons, R.; Jordan, J. *Standard Potentials in Aqueous Solution*; Taylor & Francis, 1985.
(40) Rosca, V.; Koper, M. T. M. *Electrochim Acta* **2008**, *53*, 5199-5205.
(41) Bard, A. J.; Lund, H. *Encyclopedia Of Electrochemistry Of The Elements*; Taylor & Francis, 1975.
(42) Aldous, L.; Compton, R. G. *Phys Chem Chem Phys* **2011**, *13*, 5279-5287.
(43) Chen, C.-H.; Jacobse, L.; McKelvey, K.; Lai, S. C. S.; Koper, M. T. M.; Unwin, P. R. *Anal Chem* **2015**, *87*, 5782-5789.
(44) Laborda, E.; Molina, A.; Martinez-Ortiz, F.; Compton, R. G. *Electrochim. Acta* **2012**, *73*, 3-9.
(45) Habibi, B.; Jahanbakhshi, M.; Pournaghi-Azar, M. H. *Analytical Biochemistry* **2011**, *411*, 167-175.
(46) Lourenção, B. C.; Medeiros, R. A.; Rocha-Filho, R. C.; Mazo, L. H.; Fatibello-Filho, O. *Talanta* **2009**, *78*, 748-752.
(47) Peng, Y.; Wu, Z.; Liu, Z. *Analytical Methods* **2014**.
(48) Reddy, T. M.; Narayana, P. V.; Gopal, P.; Naidu, G. R. *Analytical Methods* **2014**.
(49) Silva, W. C.; Pereira, P. F.; Marra, M. C.; Gimenes, D. T.; Cunha, R. R.; da Silva, R. A. B.; Munoz, R. A. A.; Richter, E. M. *Electroanal* **2011**, *23*, 2764-2770.
(50) Stefano, J. S.; Montes, R. H. O.; Richter, E. M.; Muñoz, R. A. A. *Journal of the Brazilian Chemical Society* **2014**, *25*, 484-491.
(51) Razmi, H.; Habibi, E. *Electrochim Acta* **2010**, *55*, 8731-8737.
(52) Karp, S.; Meites, L. *J Am Chem Soc* **1962**, *84*, 906-912.
(53) Ribeiro, A. C. F.; Barros, M. C. F.; Veríssimo, L. M. P.; Santos, C. I. A. V.; Cabral, A. M. T. D. P. V.; Gaspar, G. D.; Esteso, M. A. *J. Chem. Thermodyn.* **2012**, *54*, 97-99.
(54) Dermiş, S.; Biryol, İ. *J Pharmaceut Biomed* **1990**, *8*, 999-1003.
(55) Ayad, M. M.; Shalaby, A.; Abdellatef, H. E.; Elsaid, H. M. *Microchim Acta* **2002**, *140*, 93-96.
(56) Belal, F.; El-Ashry, S. M.; Shehata, I. M.; El-Sherbeny, M. A.; El-Sherbeny, D. T. *Microchim Acta* **2000**, *135*, 147-154.
(57) Petit, C.; Murakami, K.; Erdem, A.; Kilinc, E.; Borondo, G. O.; Liegeois, J.-F.; Kauffmann, J.-M. *Electroanal* **1998**, *10*, 1241-1248.
(58) Talwar, R.; Mahajan, R. K. *Materials and Applications for Sensors and Transducers Iii* **2014**, *605*, 581-584.
(59) Rezaei, B.; Khosropour, H.; Ensafi, A. *Ionics* **2014**, *20*, 1335-1342.
(60) Rezaei, B.; Ensafi, A. A.; Jamshidi-mofrad, E. *Sensors and Actuators B: Chemical* **2015**, *211*, 138-145.
(61) Daniel, D.; Gutz, I. G. R. *Anal. Chim. Acta* **2003**, *494*, 215-224.

(62) Wiśniewska, J.; Kita, P.; Wrzeszcz, G. *Transition Met. Chem.* **2007**, *32*, 857-863.
(63) Wiśniewska, J.; Rześnicki, P.; Topolski, A. *Transition Met. Chem.* **2011**, *36*, 767-774.
(64) Kazakova, E. K.; Syakaev, V. V.; Morozova, J. E.; Makarova, N. A.; Muslinkina, L. A.; Evtugyn, G. A.; Konovalov, A. I. *J. Inclusion Phenom. Macrocyclic Chem.* **2007**, *59*, 143-154.
(65) Sansuk, S.; Bitziou, E.; Joseph, M. B.; Covington, J. A.; Boutelle, M. G.; Unwin, P. R.; Macpherson, J. V. *Anal. Chem.* **2012**, *85*, 163-169.
(66) Wang, G.; Zhang, C.; He, X.; Li, Z.; Zhang, X.; Wang, L.; Fang, B. *Electrochim Acta* **2010**, *55*, 7204-7210.
(67) Álvarez-Ruiz, B.; Gómez, R.; Orts, J. M.; Feliu, J. M. *J Electrochem Soc* **2002**, *149*, D35-D45.
(68) Love, J. C.; Estroff, L. A.; Kriebel, J. K.; Nuzzo, R. G.; Whitesides, G. M. *Chemical Reviews* **2005**, *105*, 1103-1170.
(69) Hakkinen, H. *Nat Chem* **2012**, *4*, 443-455.

Chapter 4 Design of a Flow Injection Analysis System

In order to overcome the insufficient detection limits achieved via stationary analysis for GI determination in the presence of an API, it is beneficial to move to a hydrodynamic approach; whereby convection increases the mass transport leading to improved signal to noise ratios. Herein, a new flow injection analysis (FIA) system is developed based on an inlaid all diamond BDD microband electrode and an optimised flow cell. The FIA response is analysed numerically and against various models of dispersion to assess the quality of the method. The employed system is shown to give smaller dispersion, reduced dead volumes, higher sampling frequency and smaller sample requirement compared to previous employed FIA systems.[1,2]

4.1 Introduction

Since its inception around the 1970's,[3] FIA has grown into a large field spanning many disciplines.[4,5] Consequentially, there is no one optimal experimental FIA methodology for all applications, rather, the exact experimental design depends on the specifics of the application. For instance, several applications make use of mixing chambers, merging zones and on line liquid-liquid extraction.[6-8] Conversely, FIA for trace-level detection requires minimisation of dispersion and required sample volumes, whilst maximising sensitivity, signal to noise ratios and sampling frequencies.[9] Dispersion is particularly problematic in this area as it results in reduced signals and lower sampling frequencies. The effect of dispersion must be considered right from injection of the analyte into the system, through to detection. Note the nature of dispersion will depend strongly on the

design of the FIA flow cell and injection system and the dispersion from individual components (e.g. injection, transport, detection) is not always straightforward.[4,10-12]

There are various fluid injection mechanisms in FIA, though the 6 port method used in this study (as described in section 2.2.3) is particularly common due to its simplicity.[13] There are however promising alternatives such as time stopped methods, whereby beads inside the injection loop perturb the typical laminar profile and the injection is manually completed by switching back to the carrier stream whilst the sample is still inside the loop.[14,15] Whilst this reduces dispersion from injection, it results in unknown and inconsistent injection volumes. Furthermore, the effect of solution flow rate on dispersion is complex, dependent on the specifics of the flow system and has been the subject of study by various authors.[4,12,16,17]

In general terms, minimisation of tube diameters (or channel height for channel flow cells), increasing injection volume and reduction of injection-detector tubing length should decrease dispersion,[4] although this can be complicated by dead volumes and secondary flows, in areas where the flow cell changes geometry.[17-20] As shown below (Figure 4.1), due to the nature of the Poiseuille flow profile, geometry changes can lead to e.g. areas of low fluid flow velocity (Figure 4.1, a-regions) where material effectively gets trapped.[21]

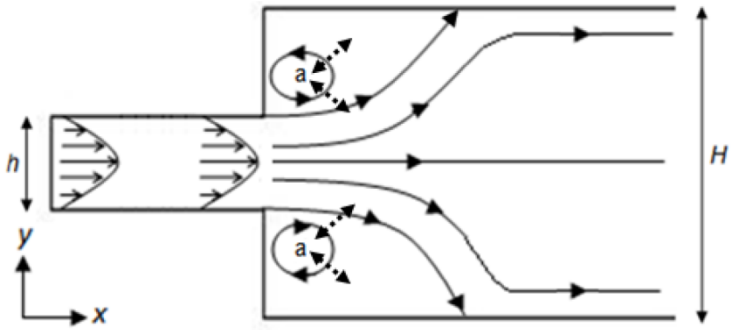

Figure 4.1: Schematic of dead volume formation (a) from the sudden expansion of flow cell.[21]

These are sometimes referred to as 'eddies' or 'areas of recirculating flow', but correspond to the same phenomenon and will be referred to as 'dead volumes' for consistency throughout this thesis.

Secondary flows refer to a subset of dead volumes, whereby a geometry change effectively leads to multiple flow paths within the same section of tubing as shown in Figure 4.2 below.[17] This effect also applies to curved tubing – typical to many FIA systems, whereby the convection and diffusion are altered with respect to flow in a straight tube.[20] Aside from increasing dispersion, this can also lead to humped peaks (Figure 4.2b). Unfortunately, many of the numerical and computational models for dispersion are based on highly-specific flow regimes in a straight cylindrical tube and do not apply to the majority of experimental FIA systems (see section 1.4.1, Figure 1.24).

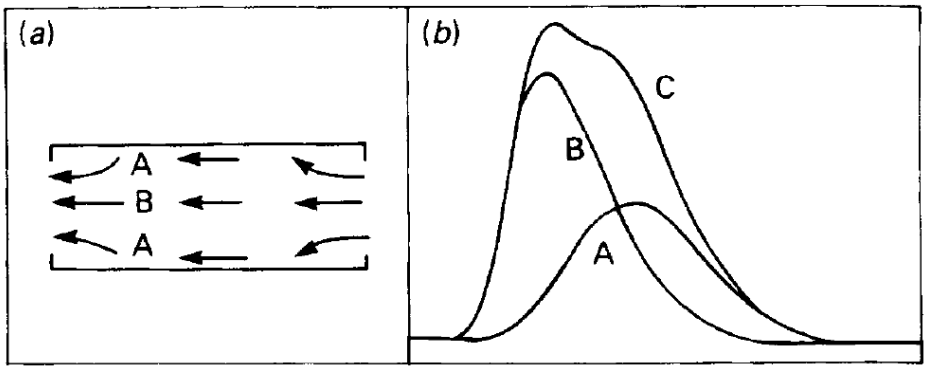

Figure 4.2: a) Secondary flows in the same section of flow cell, b) resulting peak shapes for each path (A, B) leading to an overall humped peak shape (C).[17]

In FIA-EC with channel flow cells, the detector is usually a two-part cell; formed of a base containing the electrode and a flow cell, attached to the base which determines the flow channel geometry.[2] Three-part cells are occasionally used involving a spacer between the electrode and flow cell to define the channel and electrode area, although these are not ideal as small channel heights are difficult to generate and the spacers often deform under compression leading to unknown channel heights and thus erroneous

results.[21,22] Additionally, one part cells - where the cell and electrode are part of one device – are under development.[23,24]

Common FIA-EC electrodes include Au,[25] SWNT,[2] carbon paste[26] and BDD.[27] Usually, the electrodes are either sputtered onto glass (e.g. Au bands), sealed in glass or epoxy, or the electrode size is defined using lithography.[2] The latter two methods can lead to inconsistent hydrodynamics and flow cell leakage if the electrode protrudes sufficiently from the resulting surface. Whilst sputtered Au bands are very useful due to their electrocatalytic activity and ease of fabrication,[1] the electrodes are prone to fouling or removal from the surface (as they exist only in thin film form). Thus re-calibration for each electrode before measurement should ideally be undertaken. This is similar to the use of screen printed electrodes which are cheap and easy to fabricate, but suffer from high background signals and are not ideal for long term measurements, hence they are fabricated at costs that mean they can be employed as "one-shot" electrodes.[26] BDD electrodes are ideal for hydrodynamic experiments due to their robustness and very low background signals, however they are typically sealed into glass or epoxy, resulting in recessions developing at the electrode-surround edges over time through polishing, due to the different hardness of the BDD compared to the surround, leading to changing electrochemical responses.[28]

Herein, the design and characterisation of a two-part FIA-EC design flow cell incorporating an inlaid BDD microband electrode, are demonstrated. The responses (dispersion coefficient, D_c, residence time, t_r and peak tailing) are compared to commercial and non-commercial FIA-EC methods and shown to be at least equal and in some cases superior. Finally, the signals are rationalised in relation to models for hydrodynamic mass transport and dispersion.

4.2 Results and Discussion

4.2.1 Review of Previous Flow Cell Designs

There are several methods of flow cell manufacture such as 3D printing, micromachining and microsteriolithography (MSL).[1,29,30] Common materials include acrylate resins, Perspex, Polytetrafluoroethylene (PTFE, also known as Teflon), polydimethylsulphoxide (PDMS), silicon and glass.[31] In order to understand the need for a new flow design for FIA, it is important to consider some previous example flow cell devices.

4.2.1.1 Non-Commercial Design for Flow Injection Analysis

A wide variety of FIA approaches exist with the exact optimal design clearly dependent on the application.[12] For example, on-line liquid-liquid extraction with a column is advantageous for chromatographic low pressure FIA systems with UV detection,[32] but would lead to high levels of dispersion and decreased sensitivity for electrochemical trace level detection.[33] Unfortunately many research based FIA-EC investigations do not discuss the flow cell design in detail, so it is not clear to ascertain whether the system has been optimised fully.[34-37] However, it is of interest to discuss two FIA-EC studies which do focus on system design in relation to performance.

Chi *et al.*[38] described the optimisation of a flow cell design for FIA with electrochemiluminescence detection (Figure 4.3). They used a radial flow microring electrode,[39] with a 400 μm Pt ring wrapped around a capillary as in inlet, positioned against a quartz wall ($2h \sim 50$ μm) to create a thin layer cell, as shown in Figure 4.3b. Whilst the authors demonstrate a reduction in ohmic drop and in dead volumes compared to previous electrochemiluminescence flow cell designs (Figure 4.3a), some dead volumes are still present in the inlet capillary (right angle of inlet). These dead

volumes are shown as shaded regions in Figure 4.3. Furthermore, the channel height is not exactly known in this setup, leading to uncertainty in quantification of the resulting analytical signals (equation 1.44). This design is similar to other wall jet cell and thin layer ring disk designs described in literature,[40,41] although the fluid dynamics in these systems are much more complex than with a channel flow cell.[42]

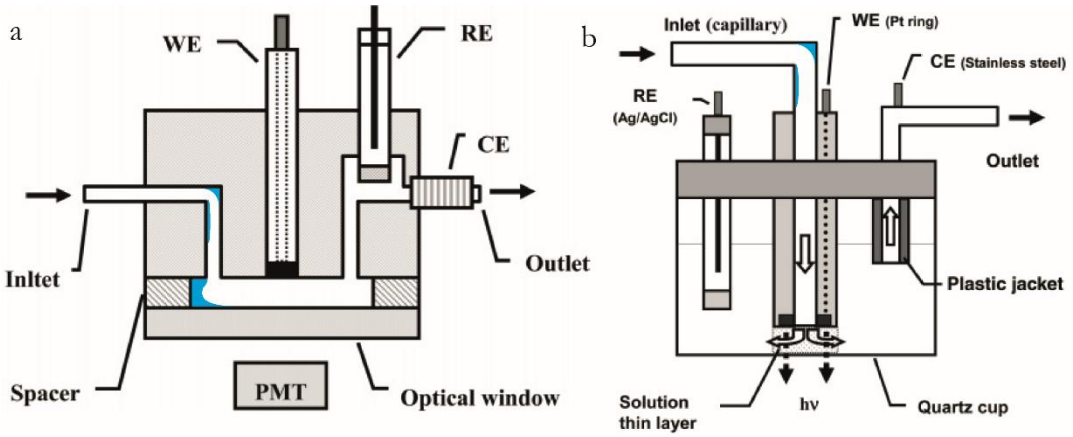

Figure 4.3: Flow cell design for electrochemiluminescence, a) typical previous design and b) improved design for this study, blue shaded areas show regions of dead volumes for FIA.[38]

Pike *et al.*[21] described an experimental and simulation approach for the design of three part flow cells for biosensing. This is pertinent to our investigations as they showed that the translation of fluid into different geometry flow cell channels can lead to large dead volumes, depending on the design, as shown in Figure 4.4. The dead volumes in these cells are shown previously in Figure 4.1. Based on finite element modelling of a series of 2D geometries (Figure 4.4b), a smooth profile between inlet and channel geometries was recommended (i.e. Figure 4.4bi over g or h) to avoid dispersion from dead volumes (Figure 4.1). However, these devices still contained a long injection-channel distance (25 mm plus connection of flow cell to injector head) including sharp geometry changes (right angle opening from top part of flow cell (b) to channel section) resulting in extra dispersion previous to the channel.

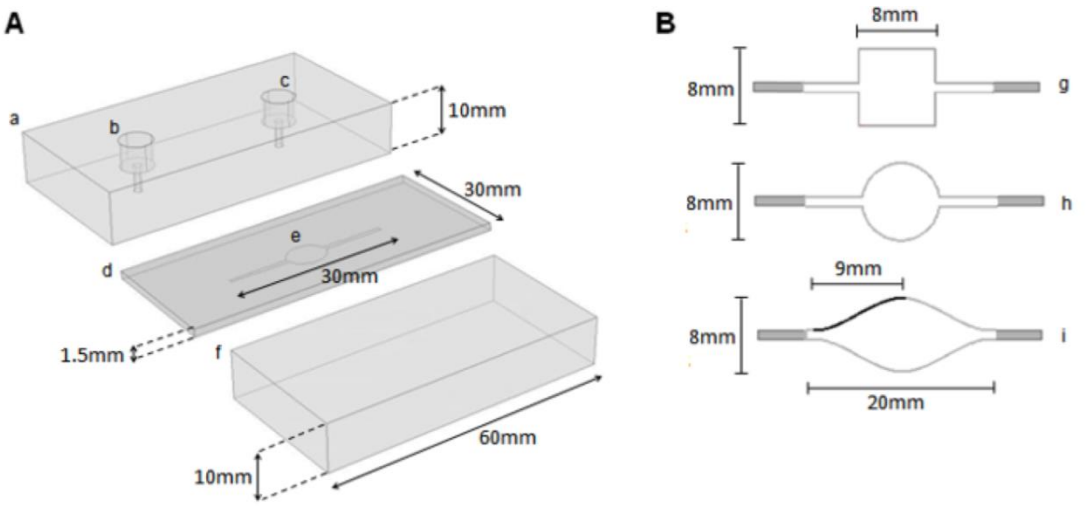

Figure 4.4: A) Design of three part flow cell with PMMA inlet and outlet section and base and PTFE mid-section defining the channel, B) different tested channel geometries.[21]

4.2.1.2 Commercial Flow Cell Designs for Flow Injection Analysis

There are different commercial FIA devices available from various companies such as Metrohm, Dropsens, Bioanalytical systems inc. (BASi) and FIAlab. For example, : Dropsens produce a range of FIA devices such as wall jet cells, channel flow cells and flow cells with already integrated screen printed carbon or Au band electrodes ($2h$ = 400 μm, width = 400 or 800 μm). These have been used in a variety of FIA-EC studies.[43,44] BASi produce a three part flow cell, intended for HPLC-EC, which is held together with a clamp and has been used for FIA-EC.[45-47] The middle section comprises an oval gasket which controls the channel height ($2h$ = 13, 51, 127 and 281 μm). An oval shaped channel is typically used, similar to Figure 4.4b-i. The main advantage of commercial flow cells is that they are already optimised for a specific application (i.e. HPLC-EC for the BASi cell, or UV/vis. for FIAlab devices) and often fairly simple to setup. However, this is also a drawback in that the flow cells can usually only be used with the commercial electrodes (e.g. 3 mm diameter GC disks for the BASi cell) and in the pre-defined arrangement, leaving no room for improvement or adaptability of the flow system.

4.2.1.3 Flow Cell Design by Microsteriolithography

MSL was chosen herein for the fabrication of flow cells for FIA-EC, as this one-step process allows the quick (~3 hours) fabrication of a variety of geometries (down to 20-100 μm feature resolution) in the same build, based on computer-aided design (CAD) structures (Solidworks). The resulting cells can then be attached to an electrode in a two-part FIA cell, with a thread or clamp.[1,48] The devices are built up in a series of X-Y layers from an acrylate resin, which is photopolymerised before moving to the next layer in the z-direction. The resulting cells are robust and can be used for numerous experiments without changing geometry or breaking. MSL has been used to fabricate flow cells through three different iterations (the third being the subject of this chapter), and it is useful to discuss the development through these interactions, in order to place the new design into context:

Snowden *et al.*[1] described the first fabrication of a microfluidic flow cell using an MSL approach (know henceforth as FIA-EC 1). This cell was designed for continuous flow voltammetry with a 200 μm channel height (*2h*) and was tested against the Levich equation (equation 1.44) and finite element modelling to characterise the hydrodynamic mass transport. Poiseuille flow was found to be developed early in the channel and the electrochemical response was found to adhere to the Levich equation, within the bounds of experimental error. The same flow cell was later used for the trace detection of dopamine (down to 10 nM),[49] the analysis of ascorbic acid oxidation[50] and dissolution of gypsum and calcium sulphate under hydrodynamic flow.[51] The flow cell design with a projection of the channel (Figure 4.5a-i), 3D wireframe model (Figure 4.5a-ii), cross section through the cell to show the flow path (Figure 4.5a-iii) and an illustration of the flow cell inlet up the channel (Figure 4.5a-iv) is shown below.

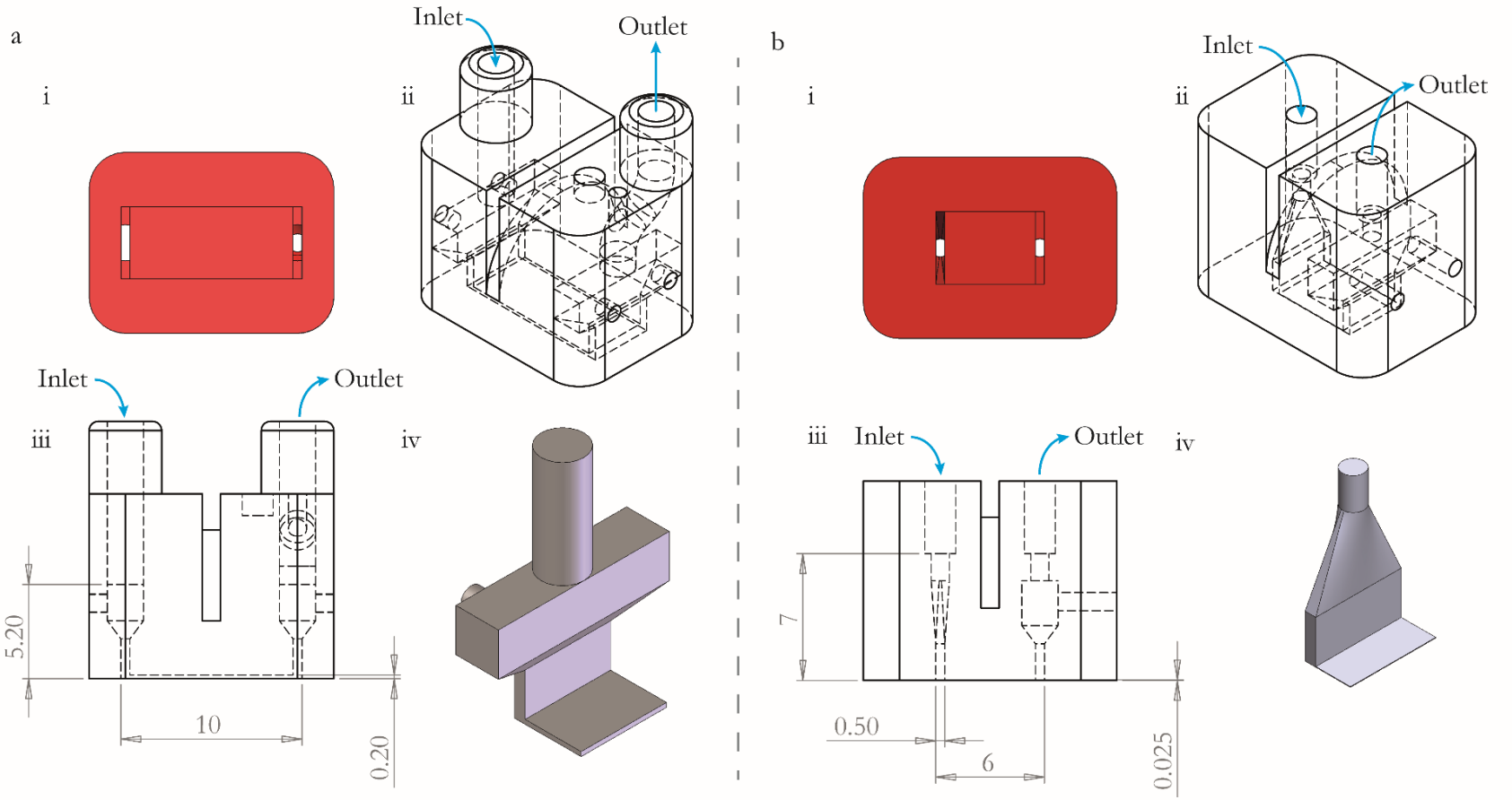

Figure 4.5: Design of MSL flow cells, a) previous design for FIA and b) updated design for FIA used in this thesis, with i) a projection of the channel ii) a 3D wireframe model, iii) a cross section through the cell to show the flow path and iv) an illustration of the flow cell inlet up the channel. All projections are to scale and all lengths are listed in mm.[1,2]

For consistency, the tubing between the injector and flow cell will henceforth be referred to as the 'injection tubing' and the region of the flow cell between the injection tubing and the channel as the 'flow cell inlet'.

This cell was adapted for FIA[2] by Sansuk *et al.,* as shown in Figure 4.5b (FIA-EC 2). We note the following important design adaptations. Firstly, the flow cell inlet is reduced both in terms of length (7 *vs* 14 mm) and volume (11.8 *vs* 73.6 μL), compared to the previous design. Secondly, the passage of flow in the flow cell inlet (Figure 4.5 a-iv *vs* b iv) is significantly smoother, featuring less steep changes in geometry and no inlet chamber (Figure 4.5a-iv) - with an expected reduction in dead volumes and thus dispersion compared to the previous design.[21] Finally, the channel height is reduced (*2h* = 50 *vs* 200 μm) in order to increase the sensitivity (equation 1.44). The same flow cell was used for the detection of hydrogen sulphide.[48] This design involved an Ag/AgCl quasi-reference and Pt counter electrode in the outlet of the flow cell. Note, ohmic drop effects (*i*R, section 1.3.1.1) can be prevalent in micrometer-sized channels and are exacerbated by small cross-sectional areas and large distances between the working and reference electrodes.[52] However, these can be offset by increasing the electrolyte concentration or by reduction of the working-reference separation (e.g. using reference and counter band electrodes in-line with a band working electrode), which is a subject of ongoing research in the field.[23]

It is also noteworthy to evaluate the *i-t* traces performed in this work during FIA-EC analysis,[2] using FIA-EC-2, as shown in Figure 4.6. The FIA capabilities were tested through the injection of a common electrochemical outer sphere mediator; $FcTMA^+$, which undergoes a one electron oxidation at $E_{1/2}$ = 0.2 V *vs* Ag/AgCl, with a $D = 6 \times 10^{-6}$ cm^2 s^{-1}.[53] For a series of 50 μL injections of 10 – 1000 nM $FcTMA^+$, D_c was found to be 0.9 - 1.05. Recall D_c is calculated from;

$$D_c = \frac{i_{\text{lim}}}{i_{\text{p}}} \tag{4.1}$$

where i_{lim} is the theoretical maximum steady state current and i_{p} is the peak current.

Also, as shown, the current did not decay to a baseline value, even after ~ 50 s when the injection head was switched back to the loading setting, in preparation for the next injection (Figure 4.6 inset). This not-complete decay indicates significant dead volumes are present in the system, causing the back end of the plug to be particularly drawn out. This is in contrast to the reasonable quoted D_c values which imply minimal dispersion is present.

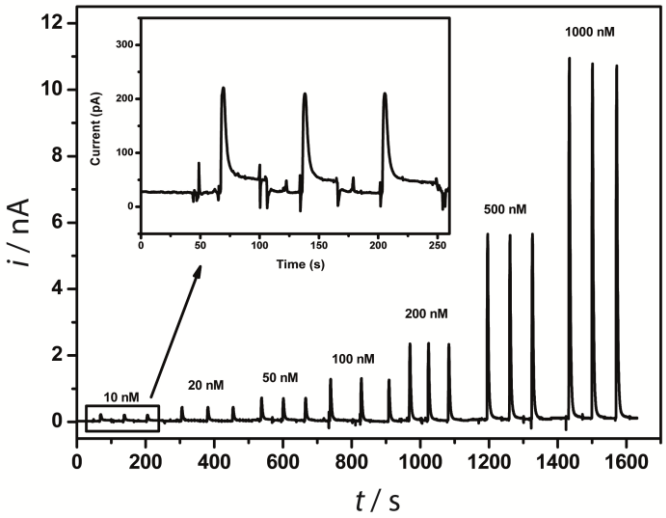

Figure 4.6: FIA *i-t* traces at V_f = 1 ml min^{-1}, with 50 μL injections of FcTMA$^+$ in 10 mM KNO_3 (10 – 1000 nM), inset; zoom in of the lowest concentration trace (10 nM), *2h* = 50 μm, 0.5 mm width SWNT network electrode.[2]

4.2.1 Final Flow Cell Design

In light of the previous studies and recognizing general approaches for minimising dispersion i.e. thinner tubing, shorted injection-detection length and larger sample volume,[54] the following flow cell (FIA-EC 3) was designed as shown in Figure 4.7b in comparison to the previous design (Figure 4.7a, FIA-EC 2):

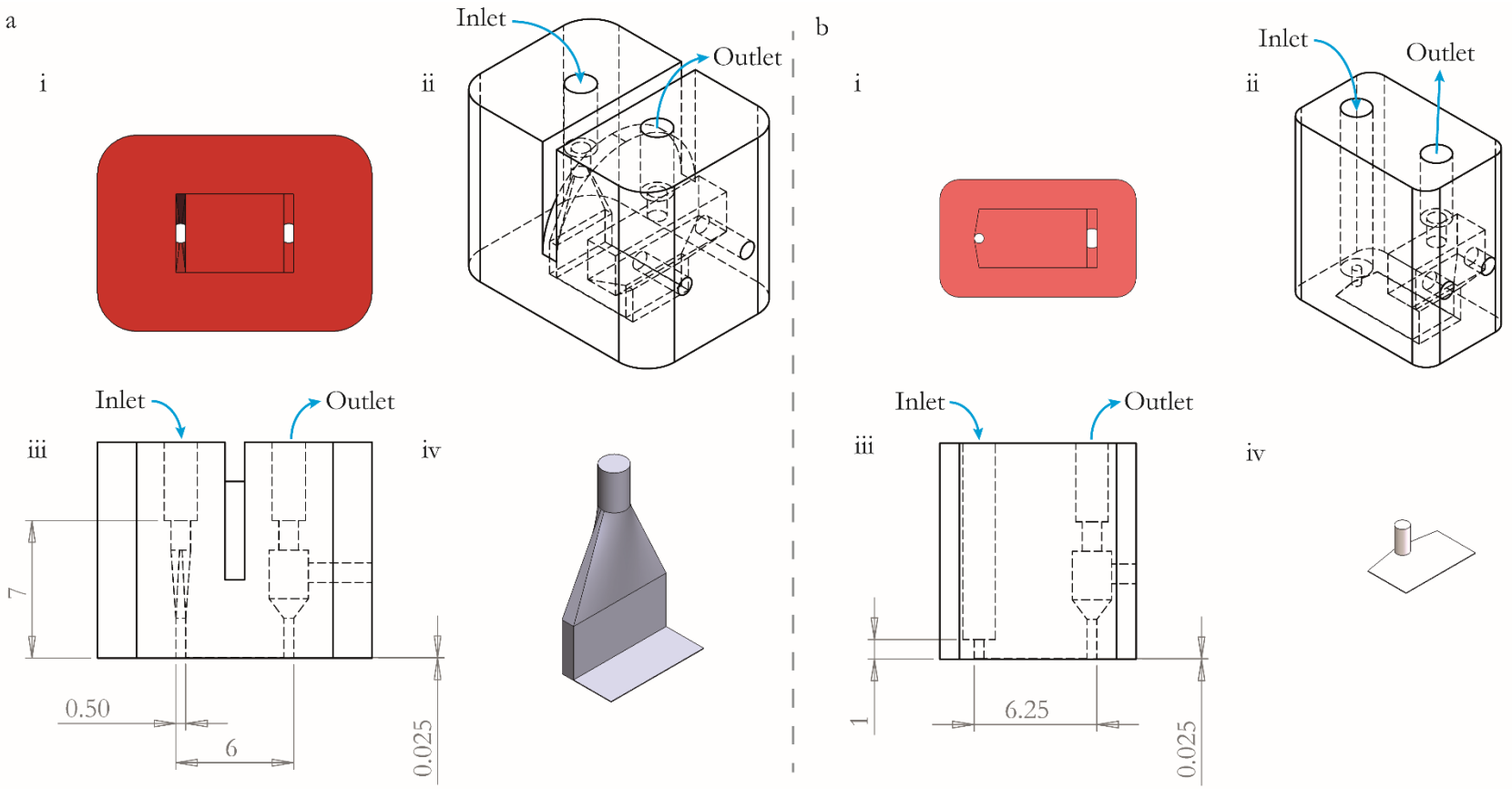

Figure 4.7: Design of MSL flow cells, a) previous design for FIA and b) updated design for FIA used in this thesis, with i) a projection of the channel ii) a 3D wireframe model, iii) a cross section through the cell to show the flow path and iv) an illustration of the flow cell inlet up the channel. All projections are to scale and all lengths are listed in mm.[2]

We can again note the following design adaptations: Firstly, a fan style opening to the channel has been adopted (Figure 4.7b-i,iv) in order to smooth the inlet-channel flow transition compared to the previous design (Figure 4.7a-i,iv). Secondly, the flow cell inlet length (1 *vs* 7 mm) and volume (0.19 *vs* 11.8 μL) have been minimised (Figure 4.7b-iv) compared to the previous design (Figure 4.7a-iv), FIA-EC 2. This, coupled with the shorter and smaller inner diameter injection tubing (l = 12.5 cm by 0.18 mm ID *vs* l = 15 cm by 0.5 mm ID) should lead to a reduction in flow cell internal volume, dispersion and residence time (t_r – time between injection and maximum signal). Furthermore, the reduction in geometry changes should reduce the amount of dead volumes in the flow cell,[21] though this is difficult to quantify accurately from the amperometric response and would require finite element modelling to properly elucidate. Thirdly the overall flow cell is smaller (5.5 by 10 by 11 mm for FIA-EC 3) than previous designs (9 by 11 by 11 mm for FIA-EC 2), therefore more devices can be fabricated in the same MSL build (4-6 devices), and shorter length bands are required (flow cell width 5.5 *vs* 9 mm). Finally, as with the previous design (FIA-EC 2), 0.5 mm ID Teflon tubing is used for the flow cell outlet, to provide a path of minimal resistance and to prevent leaks at the reference and counter electrode ports.

The full FIA system (flow cell and electrode) is shown below in Figure 4.8. The inlet and outlet tubes were glued into the flow cell with epoxy glue and the Ag/AgCl reference (1 mm OD) and Pt counter (1 mm OD) electrodes were slotted into the outlet chamber and held in place with Teflon tape. The flow cell and working electrode substrate were held together by a clamp utilizing minimal force so as to prevent leakage, without deforming the flow cell,[55] as previously described by Bitziou *et al.,*[48] and as shown in Figure 4.9.[48]

The all-diamond microband electrode is also shown (Figure 4.8b). The small black spots on the insulating diamond are micro-fractal defects (~ nm in size).[56] These may contain small amounts of non-diamond-carbon, but as they are electrically isolated from the BDD they will not contribute to the electrochemical response of the band electrode.

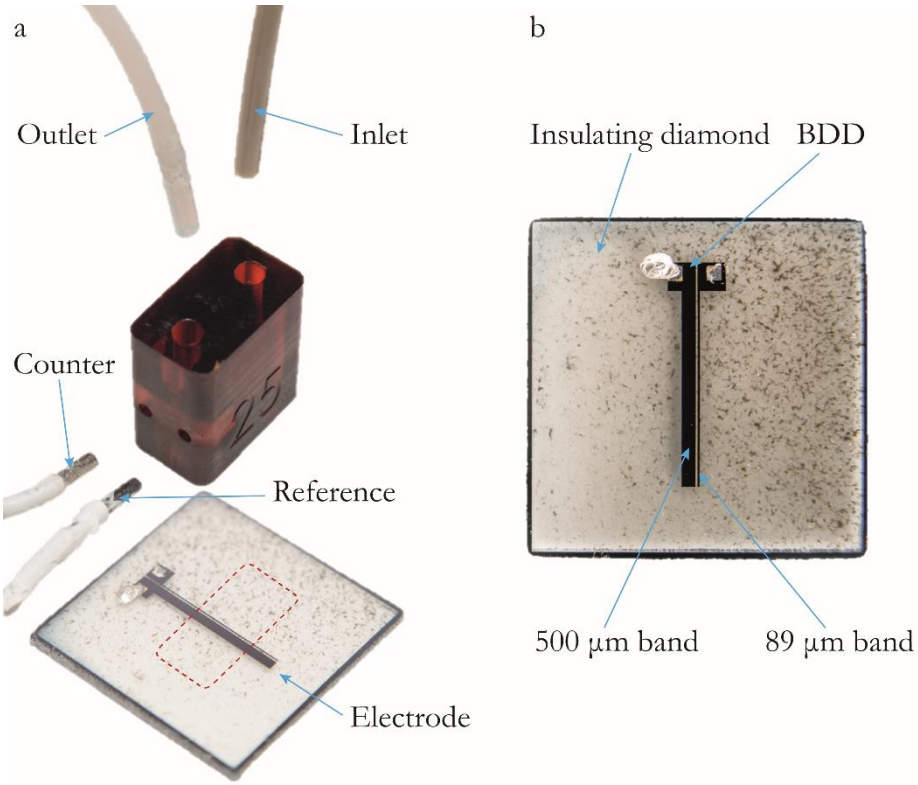

Figure 4.8: Illustration of a) the full FIA setup and b) the all-diamond microband electrode.

A series of different channel height flow cells (nominal $2h$ = 25, 50, 100 and 200 µm) were fabricated in the same build, although the 25 µm was chosen for this study in order to maximize the analytical signal (equation 1.44). In order to confirm the channel height, the cell was clamped with the same force as that used to hold the flow cell and electrode together for solution work, and the internal structure mapped using interferometry (in air) to determine the actual channel height. As shown in Figure 4.9, channel dimensions of w = 3 mm and $2h$ = 22.5 µm were discerned which are reasonable based on the design geometries and the resolution of the MSL build process (x-y resolution ~ 38 µm, z resolution ~ 25 µm). Also, it is worth noting the clamp design, such that the flow cell is held in place against the flat top and bottom sections (Figure

4.9c-ii) with a large gap in the top for the inlet and outlet tubing (Figure 4.9c-i) and a slit in the bottom for interferometry imaging of the channel (Figure 4.9c-iii).

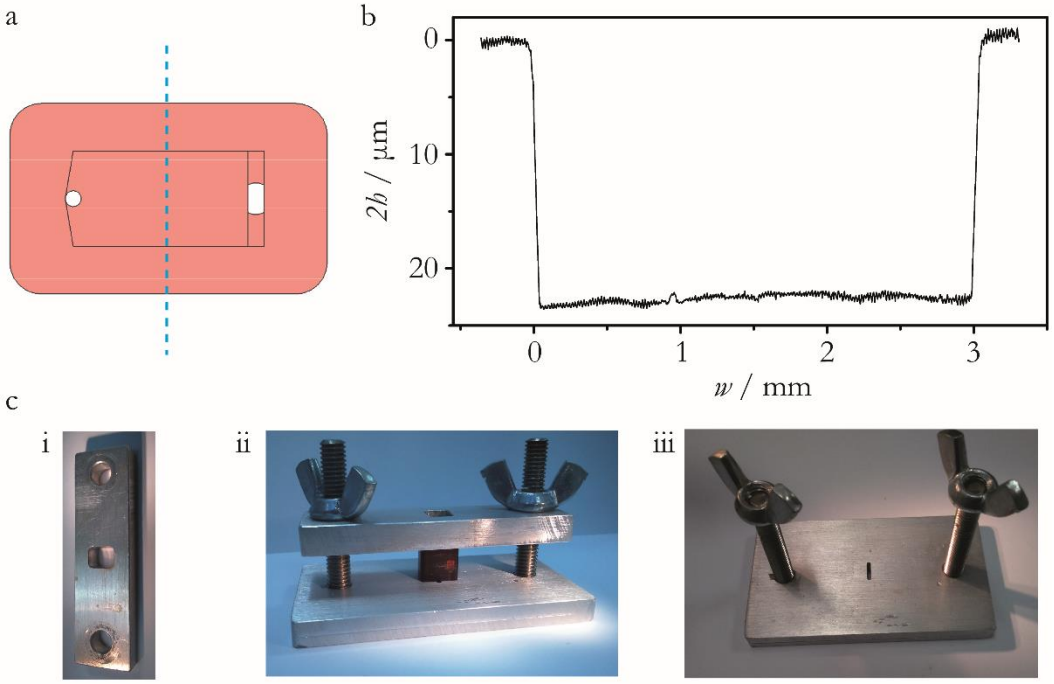

Figure 4.9: Interferometry of flow cell to show channel geometry, a) horizontal cross section studied by interferometry, b) interferogram across channel, average height $2h$ = 22.5 µm, c) clamp for interferometry with i) top section, ii) clamped flow cell and iii) bottom section.

4.2.2 Characterization of the Device

The all-diamond BDD microband electrode shown in Figure 4.8b, was characterised by FE-SEM to determine the exact electrode geometry (Figure 4.10). The two bands were found to have an x_e = 89 µm and 530 µm with a separation of 58 µm. Note that the different polycrystalline grains on the intrinsic diamond and BDD are visible. For the remainder of this thesis only the 89 µm band electrode is employed in order to achieve the highest mass transport rates and thus the lowest limit of detection (LOD). The BDD is essentially co-planar with the insulating diamond substrate; AFM reveals the BDD is recessed by only 1.69 nm ± 0.75 (n = 3) compared to the insulating surround. This contrasts with other common flow cell electrode designs such as SWNT covered by a

photoresist, whereby the recession is around 1 μm,[49] or Au bands, where the height is typically around 100 nm.[2]

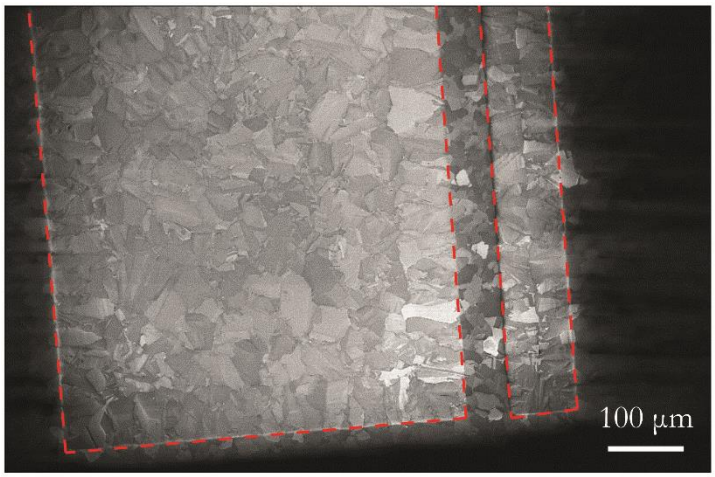

Figure 4.10: SEM of the all-diamond microbands with an in-lens detector, 2 kV accelerating voltage and 4 mm working distance, bands are outlined with red-dashed line for clarity.

To confirm the electrochemical quality of the BDD grown into the all diamond substrate, a solvent window was run as shown in Figure 4.11. In this case, the solvent window was found to be 3.63 V (between ± 0.4 mA cm^{-3}) , which compares favourably other electrodes of the same material quality (*ca* 3.41 V for 1 mm macrodisk BDD electrode as shown in section 1.3.2).[57]

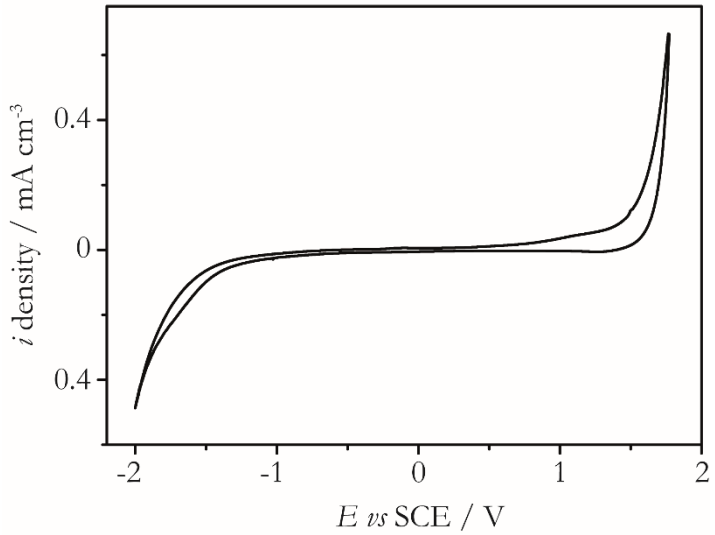

Figure 4.11: Solvent window for the 89 μm BDD microband electrode in 0.1 M KNO_3, scan rate = 0.1 V s^{-1}.

In order to characterize the complete experimental set-up, CVs recorded under continuous flow at a potential scan rate of 0.1 V s^{-1} were recorded for the fast outer sphere electron transfer couple $FcTMA^+$ (10 μM in 0.1 M KNO_3, Figure 4.12) as a function of volume flow rate, over the range V_f = 0.1 – 1.5 ml min^{-1}. Transport in the channel was characterized by a Reynolds number, *Re* = 22.0 (from equation 1.42, V_f = 1 ml min^{-1}), corresponding to laminar flow. Furthermore, we can estimate the distance required to establish poiseuille in the channel by the following equation:[58]

$$l_e = 0.1hRe \tag{4.2}$$

l_e is found to be 24.8 μm implying that laminar flow is well developed before the flow reaches the electrode, around half way down the channel (~ 3 mm).

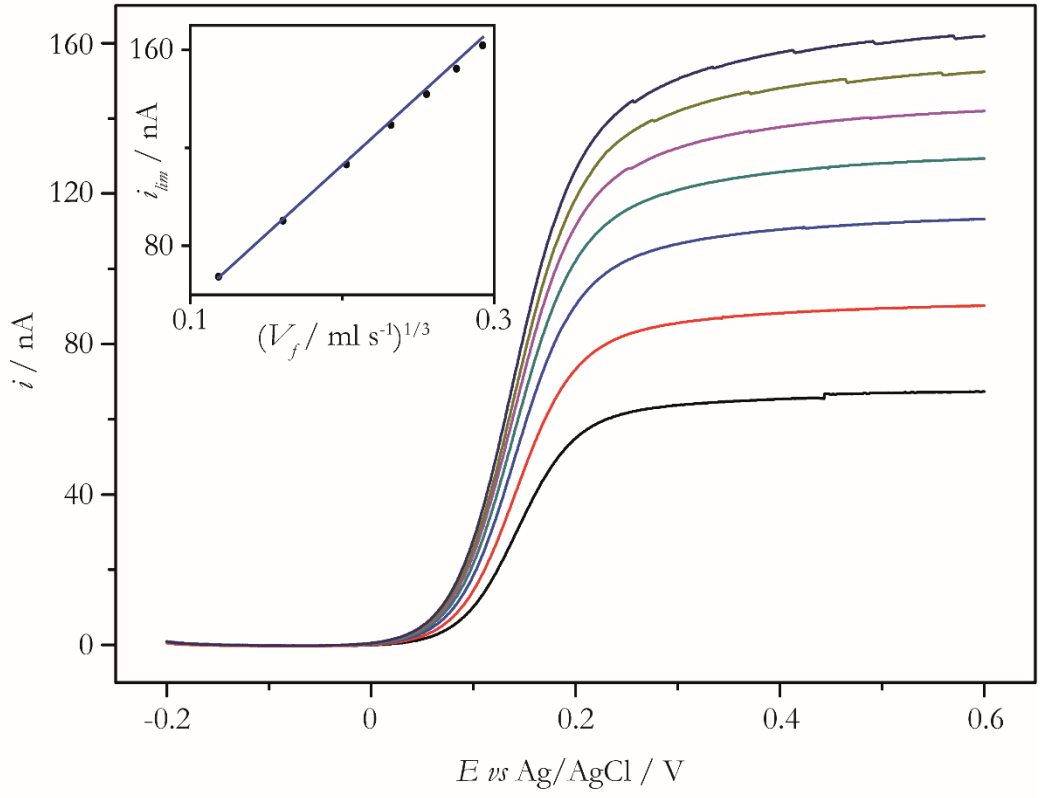

Figure 4.12: Background subtracted CVs recorded under continuous flow with 10 μM $FcTMA^+$ in 0.1 M KNO_3, at 0.1 V s^{-1} with V_f of 0.1 (lower), 0.25, 0.5, 0.75, 1, 1.25 and 1.5 (upper) ml min^{-1}. Inset: Experimentally recorded i_{lim} vs $V_f^{1/3}$ plotted against the Levich theory line (equation 1.39), for the cell and electrode dimensions defined (w = 3 mm, $2h$ = 22.5 μm, x_e = 89 μm).

Based on a D_{FcTMA+} = 6.71 × 10^{-6} cm^2 s^{-1} (determined by CV with a 14.5 μm radius Pt ultramicroelectrode in a solution containing 1 mM $FcTMA^+$ and 0.1 M KNO_3), there is a very good fit of the experimental i_{lim} data (•) and the theoretical i_{lim} as predicted by equation 1.44 (▬), confirming the flow characteristics of the cell, for the given electrode and cell dimensions described. As previously discussed, minimisation of channel dimensions increases the analytical signals and should reduce dispersion. However it is worth bearing in mind the increase in solution resistance through reduction of channel geometries is given by,[59]

$$R_s = \frac{l}{\kappa A'} \tag{4.3}$$

where κ is the solution conductivity (= 5 $\Omega^{-1}m^{-1}$) and A' is the cross sectional area (channel = 0.075 mm^2, outlet of channel = 1.5 mm^2, ref and counter chamber = 9 mm^2). Between the working and reference electrodes inside the flow cell, R_s = 8366 Ω, which should not result in ohmic drop (*i*R) effects for moderate concentrations of faradaic species.[57] Hence this flow cell is ideal for trace detection of species (low concentrations), but not suited for the determination of higher molarity species, where ohmic effects may occur.

It is interesting at this point to consider mass transport in the channel, as this effects the electrochemical signal recorded, under the flow conditions described. The transport in the centre of the channel will be dominated by convective mass transport where the velocity is greatest (33.3 cm s^{-1} for V_f = 1 ml min^{-1}). However at the edges against the band electrode, the velocity effectively drops to zero (equation 1.39) and diffusive mass transport dominates.[59] The size of the diffusive layer under laminar flow, perpendicular to a band electrode is given by,[49]

$$\delta = \frac{1}{0.67} \times \left(\frac{2hDx}{3\bar{U}}\right)^{1/3} \quad (4.4)$$

where x is the width along the electrode. This is easier to appreciate visually, as shown in Figure 4.13 for flow within the flow cell at V_f = 1 ml min^{-1} (typical of flow rates employed in these studies) for the 89 μm band. δ = 1.39 μm at the middle of the band and δ = 1.75 μm at the downstream edge of the band (with respect to $2h$ = 22.5 μm). This shows that even with the relatively small channel height employed, the vast majority of the plug (~ 90%) does not pass close enough to interact with the electrode at V_f = 1 ml min^{-1}.

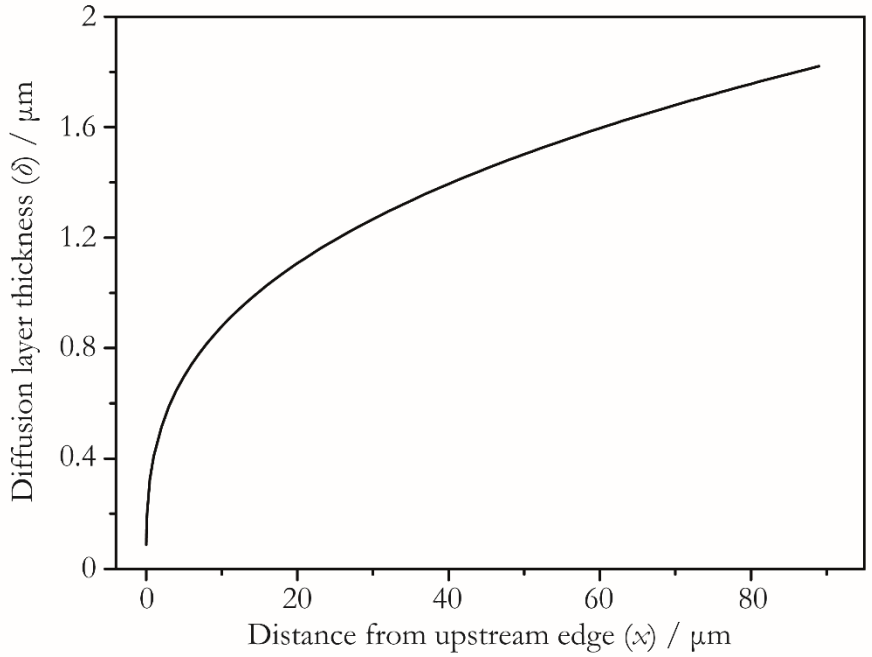

Figure 4.13: Size of diffusive layer aside band electrode, from equation 4.3, V_f = 1 ml min^{-1}.

4.2.3 Flow Injection Analysis of FcTMA$^+$

The FIA capabilities were studied via the injection of FcTMA$^+$ (50 μL injection of 10 μM in 0.1 M KNO_3) into a carrier stream containing 0.1 M KNO_3 at a V_f of 1 ml min^{-1}, as shown in Figure 4.14. The peak height i_p = 138.5 nA, which matches very closely with the theoretical maximum i_{lim} for continuous flow (and consequently the Levich equation 1.44 predicted value), yielding a D_c = 1.00 (from equation 1.46). t_r was determined as

1.83 s and the peak tailing was found to be significantly reduced compared to that of previous MSL flow cell design, FIA-EC 2 (Figure 4.6).[2,48]

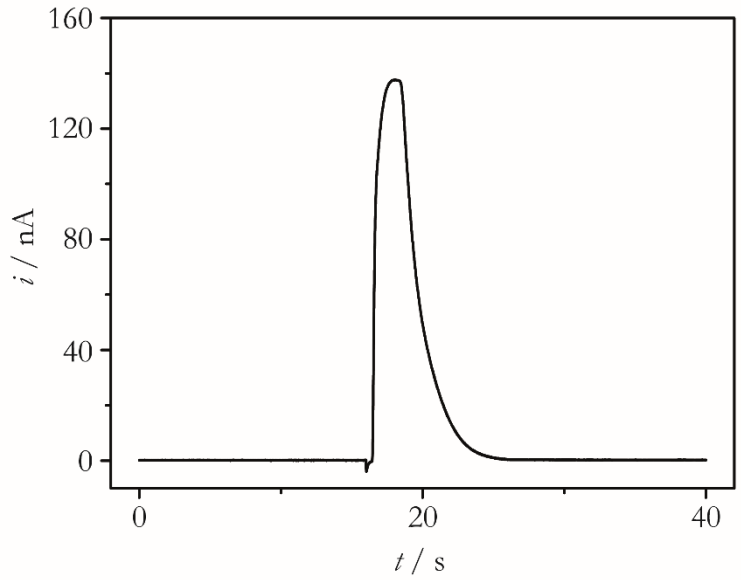

Figure 4.14: FIA-EC detection for 50 μL injection of 10 μM FcTMA$^+$ in 0.1 M KNO_3 at V_f = 1 ml min^{-1}, electrode held under transport limited conditions at +0.6 V vs Ag/AgCl.

As eluded to above, for the type of system employed herein (small internal volume, small t_r), D_c alone does not give a full description of dispersion in the system: So long as any dispersive process (e.g. dead volumes, secondary flows, radial and axial dispersion, convection) do not significantly disperse the injected plug, D_c = 1.00 will still be measured, as long as enough material passes over the electrode at the injected initial concentration to reach the steady state current i_{lim} (i.e. dispersion occurs at edges of plug but does not affect detector peak response). Although this is not ideal in that elucidation of dispersion in the system from the detector response is difficult, this does bode well for trace detection as the intention is to achieve the largest signal (i.e. $i_p = i_{lim}$, D_c = 1.00, large V_f, small $2h$) for the smallest concentration and volume of injected sample.

Conversely, for Taylor type systems (large internal volume, large t_r, small V_f), D_c is a very good indicator of dispersion as dispersion will increase the overall plug volume

leading to a general reduction in concentration between injection and detection (Figure 1.22). The Taylor condition states that Taylor dispersion occurs provided;[60]

$$\frac{(2h)^2}{4\pi^2 D} \ll \frac{l}{\bar{U}} \tag{4.5}$$

For our system, as the left hand side equates to 0.754 and the right, 0.662, the Taylor condition is not met and dispersion from radial diffusion is expected to be minimal. Experimentally, the maximum possible sampling frequency depends not only on t_r, but also on the time taken for the peak to return to a baseline ready for the next injection to avoid overlapping signals. A surprisingly wide range of sampling frequencies are found in FIA literature;[12,61] e.g. from one every 500 seconds,[62] up to one every 18 seconds.[63]

The Peclet number, P_e (equation 1.48), and dimensionless time, τ_d (equation 1.49) are 5.52×10^6 and 0.0572 respectively. This indicates a relatively short time between injection and detection compared to the majority of FIA investigations, as shown in Figure 4.15. Similarly, the large P_e indicates the mass transport is primarily convective rather than diffusive. Aside from the methods discussed Figure 4.15,[64-68] there are various more complex approaches to modelling dispersion such as; the black box,[68] tanks in series,[69] least squares[70] and random walk methods.[71] However, none of these approaches are perfect and crucially; do not fully assess dispersion in different segments of the flow system, particularly from injection.[4] This is crucial for the flow system employed herein, as the material at the back of the sample loop has to travel a much greater relative distance under Poiseuille flow than the front of the plug (23.4 cm vs 16.4 cm), leading to exacerbated dispersion at the back of the plug.[14] Some approaches link the D_e to the V_f, length and tube radii, although these only really apply to a single manifold straight tube.[68]

There are also approaches which quantify the response based on the peak width,[72] peak variance[73] and some which model the peak as an exponential modified Gaussian

distribution.[74] One approach of elegant simplicity is that of Davey et al,[75] who assess the peak tailing via the response time (from initial rise to peak signal), as well as the decay to 50 % and 95% loss in signal after the peak. For the peak response described in Figure 4.15, the times are 1.44 s (50% decay) and 4.78 s (95 %) respectively.

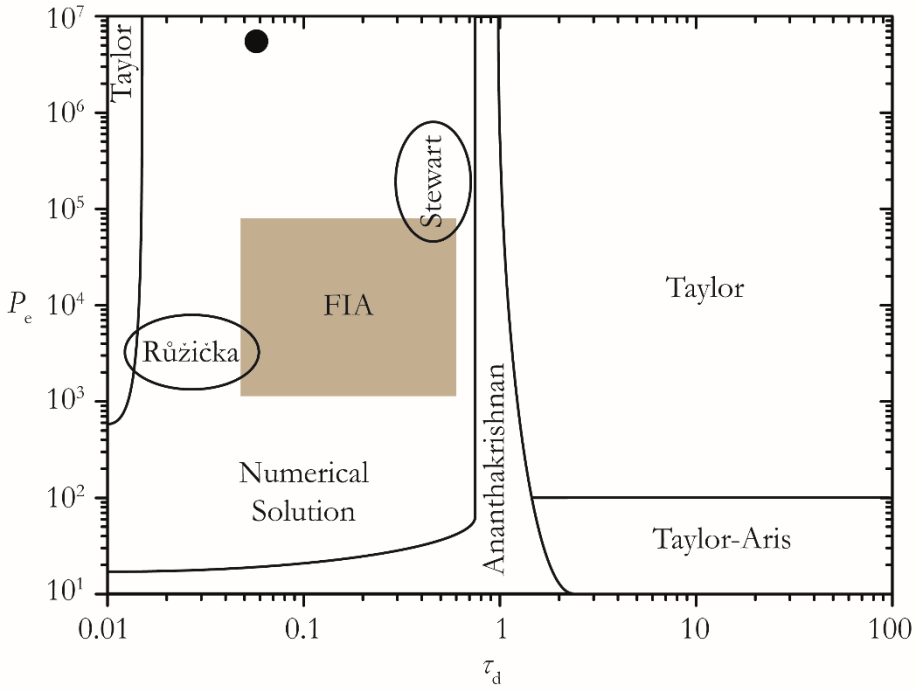

Figure 4.15: Schematic of solutions to the diffusion-convection equation (equation 1.42), with common experimental systems in segmented sections and typical FIA experiments in the brown shaded region and the experimental result of Figure 4.14 shown (●).[74,76]

We can summarise the improvements in MSL generations as shown in Table 4.1 below. The flow system employed compares favourably with most FIA system in literature, although direct comparison is difficult without the original data and testing in the same fashion. In order to check the applicability of this flow system for trace detection, 10-1000 nM plugs (50 μL) of $FcTMA^+$ were injected, as shown in Figure 4.16. The LOD for this system is 2.69 nM, which is promising towards the use of this system for different trace detection applications such as toxic impurities and neurochemicals.[2,77] This value could also be reduced through a smaller channel height, a thinner band electrode, faster flow rate and a more advanced injection unit.

MSL design:	FIA-EC 1 (Snowden *et al.*)[1]	FIA-EC 2 (Sansuk *et al.*)[2]	FIA-EC 3 (3rd generation)
Internal volume[a]	73.6 µL	11.8 µL	0.19 µL
$2h$ / µm	250	50	22.5
D_c	-	0.9 – 1.05[d]	1.00
t_r / s	-	9.8	1.83
50% decay[b] / s	-	2	1.44
95% decay[c] / s	-	9.29	4.78
FcTMA$^+$ LOD	-	20 pM[e]	2.69 nM
P_e	5.55×10^6	2.08×10^6	5.52×10^6
τ_d	-	0.0923	0.0572

Table 4.1: Comparison of different generation MSL flow cells. [a]The volume of flow cell between injection tubing up and half way down channel. [b,c]The time to decay from the peak signal to 50 and 95 % of the value towards baseline respectively. [d]Calculated from a range of concentration injections. [e]Calculated via a different LOD method (see discussion below).

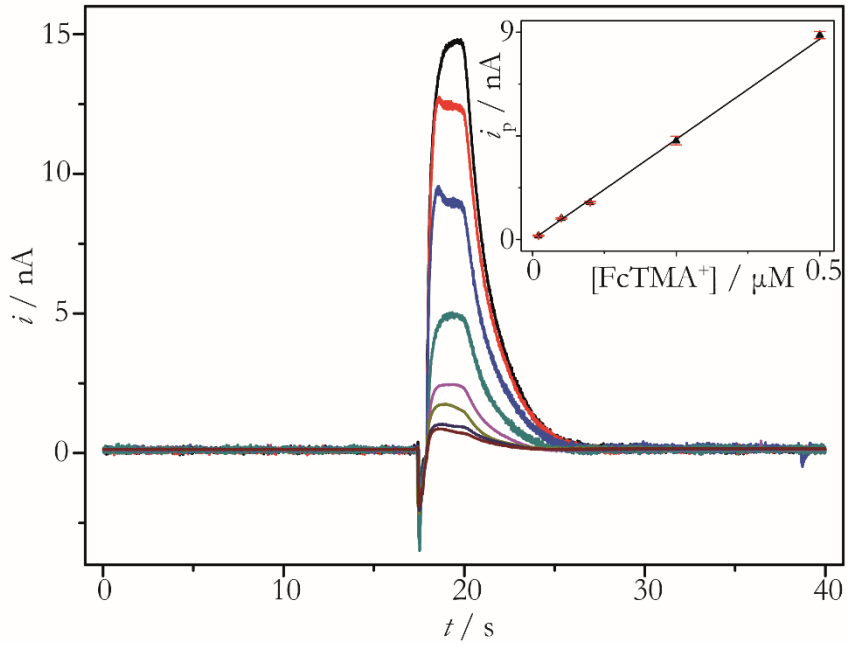

Figure 4.16: FIA of 50 µL injections of 0, 10, 50, 100, 250, 500, 750 and 1000 nM FcTMA$^+$ into 0.1 M KNO_3 at 1 ml min^{-1}. Inset; background subtracted LOD plot for 5 lowest concentrations, R^2 = 0.999, sensitivity = 17.4 nA µM^{-1}, LOD = 2.69 nM. Note, when a plateau is not reached, i_p is taken as the highest current.

It is worth noting at this point that various authors propose different methods for calculating the LOD. For example Sansuk *et al.*[2] use the standard deviation of the baseline (SD_{baseline}) as a blank injection, i.e.

$$LOD = \left(\frac{3SD_{baseline}}{i_{\text{p}}}\right) c_{\text{b}} \tag{4.6}$$

This method is particularly useful when no blank is recorded (as in reference 20) as the LOD can then be estimated from the lowest concentration recorded. However, the variation of a blank injection for the systems employed herein is typically ~ six times larger than that of the baseline, thus this approach tends to underestimate the LOD. Therefore a similar method is employed to chapter 3,[78] i.e.

$$LOD = \bar{\mu} + 3\sigma \tag{4.7}$$

where $\bar{\mu}$ is the mean peak current from several blank injections and σ is the standard deviation of the blank injection response (n=5). This value is converted from current to concentration by dividing by the sensitivity (i.e. the slope of the LOD plot – Figure 4.16 inset).

It is also important to understand the effect of injection volume on the analytical signals, particularly towards applications with only very small quantities of sample. Therefore 5, 10, 25, 50, 100 and 200 μL aliquots of 10 μM $FcTMA^+$ were tested as shown in Figure 4.17.

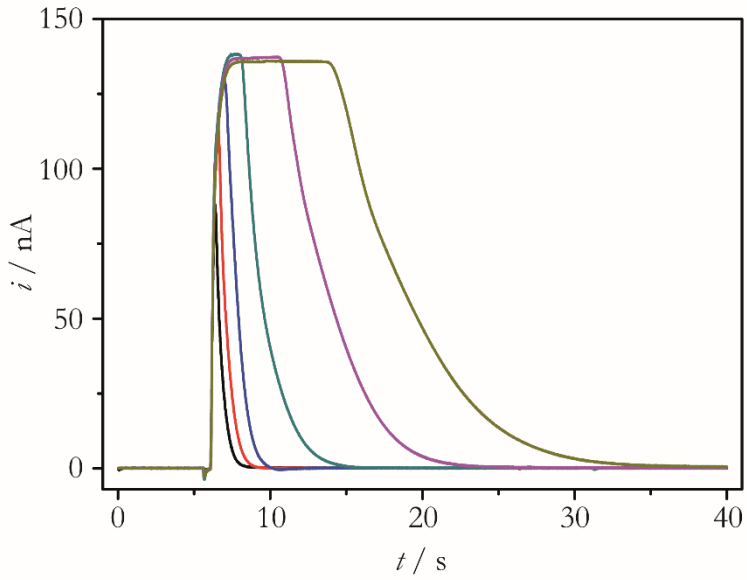

Figure 4.17: FIA of 5, 10, 25, 50, 100 and 200 μL of 10 μM $FcTMA^+$ into 0.1 M KNO_3 at 1 ml min^{-1}.

Clearly the front part of the curve is the same with all loop sizes, but the smaller loops (5, 10, 25 μL) sharply decay away before reaching the steady state value (i_{lim}, in agreement with the values from continuous flow analysis and the Levich equation 1.44). This effect has been previously observed in literature,[17] although in this study a 282 μL injection was required to hit the steady state value. We can analyse these results in more detail; with respect to the D_c and t_r, given in Table 4.2 below.

Loop size / μL	i_p / nA	t_r / s	D_c
5	88.0	0.77	1.57
10	113.9	0.98	1.21
25	129.3	1.39	1.07
50	138.3	1.83	1.00
100	137.3	4.85	1.01
200	136.1	4.86	1.02

Table 4.2: FIA of $FcTMA^+$ with different injection loop volumes, from Figure 4.18.

As expected, smaller loops result in greater D_c although it is unclear if this is due to dispersion in the system, or the Poiseuille flow profile in the channel not allowing enough material over the electrode for long enough to reach the steady state current. Ideally, all plug volumes would reach i_{lim} for ease of quantitation, however, the signal can be corrected for plug size, provided i_p and D_c are consistent between multiple injections of the same concentration.[79] Another approach could be to reduce the channel height (*2h*), as this would partially negate the second (Poiseuille) effect. Similarly, reduction in injection-detection length, internal volume and dead volumes would negate the former effect (lower D_c from dispersive effects). Another advantage of smaller injection volumes is smaller t_r and quicker decay to baseline currents, resulting in higher possible sampling frequencies.

As most models for dispersion do not apply to the employed system (Figure 4.15) and most numerical methods give only an indication of the fluid dynamics of the system in terms of dispersion and sampling frequency, 3D finite element modelling should be undertaken of the flow system employed herein. This would allow separation and quantitation of dispersion from different factors (dead volumes, secondary flows, diffusion and convection) as well as infer on further improvements to the design for future studies. Furthermore, this should allow the elucidation of the FIA-EC response in relation to these factors, for example simulation should explain the i_p for different sample volumes. 2D finite element modelling has previous been undertaken for the modelling of continuous flow analysis[1] and FIA,[21,80] although in one of these cases the FIA system was through gravity driven flow under Taylor dispersion,[80] and though the other considers dispersion through dead volumes,[21] only the channel geometry in considered.

4.3 Conclusions

In this chapter a new flow cell is designed and tested via continuous flow CV and FIA. A segmented approach is undertaken to understand and improve the setup through optimisation of the geometries from injection, fluid transport and detection, in relation to previous designs. The two part cell, with the bottom component comprising a co-planar BDD microband electrode, insulated in an insulating diamond platform is simple to assemble and disassemble repeatedly. Moreover, the diamond based substrate means the electrode never changes its geometry through repeated use.

Through minimisation of internal flow cell volume and smoothing of flow geometries, dead volumes and dispersion are minimised and high possible sampling frequency is demonstrated in comparison to previous designs. Furthermore, the possibility of trace detection down to ~ nM levels is demonstrated as well as the use of reduced sample volumes whilst maintaining high analytical signals. Work is currently being undertaken concerning the 3D finite element modelling of this flow system, to characterise the effect of dead volumes and secondary flows on FIA-EC analytical signals.

4.4 References

(1) Snowden, M. E.; King, P. H.; Covington, J. A.; Macpherson, J. V.; Unwin, P. R. *Anal. Chem.* **2010**, *82*, 3124-3131.

(2) Sansuk, S.; Bitziou, E.; Joseph, M. B.; Covington, J. A.; Boutelle, M. G.; Unwin, P. R.; Macpherson, J. V. *Anal. Chem.* **2013**, *85*, 163-169.

(3) Stewart, K. K. *Talanta* **1981**, *28*, 789-797.

(4) Trojanowicz, M. *Advances in flow analysis*; John Wiley & Sons: Germany, 2008, p 702.

(5) Barceló, D. *Advances in flow injection analysis and related techniques*; Elsevier: UK, 2008, p 783.

(6) Fernandez, M.; Clavijo, S.; Forteza, R.; Cerda, V. *Talanta* **2015**, *138*, 190-195.

(7) Amornthammarong, N.; Ortner, P. B.; Zhang, J.-Z. *Talanta* **2010**, *81*, 1472-1476.

(8) Vida, A. C. F.; Sasaki, M. K.; Gomes, T. F.; Silva, C. R.; Feres, M. A.; Zagatto, E. A. G. *Talanta* **2011**, *85*, 259-263.

(9) Sansuk, S.; Bitziou, E.; Covington, J. A.; Joseph, M. B.; Boutelle, M. G.; Unwin, P. R.; Macpherson, J. V. *Anal Chem* **2013**, *85*, 163-169.

(10) Reijn, J. M.; Van Der Linden, W. E.; Poppe, H. *Anal. Chim. Acta* **1981**, *126*, 1-13.

(11) Reijn, J. M.; Van Der Linden, W. E.; Poppe, H. *Anal. Chim. Acta* **1980**, *114*, 105-118.

(12) Růžička, J.; Hansen, E. H. *Flow injection analysis*, 2nd ed.; J. Wiley: New York, 1988, p 498.

(13) Product Bulletin 209: Models 7725/7725i and 9725/9725i Sample Injectors for HPLC https://www.idex-hs.com/support/literature-downloads/operation-manuals [accessed 04/09/15].

(14) Johnson, B. F.; Malick, R. E.; Dorsey, J. G. *Talanta* **1992**, *39*, 35-44.

(15) Coq, B.; Cretier, G.; Rocca, J. L.; Porthault, M. *J. Chromatogr. Sci.* **1981**, *19*, 1-12.

(16) Li, Y. H.; Ma, H. C. *Talanta* **1995**, *42*, 2033-2038.

(17) Stone, D. C.; Tyson, J. F. *Analyst* **1987**, *112*, 515-521.

(18) Vannecke, C.; Baré, S.; Bloomfield, M.; Massart, D. L. *J Pharmaceut Biomed* **1999**, *18*, 963-973.

(19) Leach, A. M.; Wheeler, A. R.; Zare, R. N. *Anal Chem* **2003**, *75*, 967-972.

(20) Balasubramanian, V.; Jayaraman, G.; Iyengar, S. R. K. *Zeitschrift Fur Angewandte Mathematik Und Mechanik* **1999**, *79*, 335-352.

(21) Pike, D.; Kapur, N.; Millner, P.; Stewart, D. *Sensors* **2012**, *13*, 58.

(22) Liu, C.; Wei, X.; Tu, Y. *Talanta* **2013**, *111*, 156-162.

(23) Newland, J. C. *The Fabrication and application of diamond sensors for electrochemical analysis in single and multiple phase systems*. PhD, Warwick, 2014.

(24) Hutton, L. A.; Vidotti, M.; Iacobini, J. G.; Kelly, C.; Newton, M. E.; Unwin, P. R.; Macpherson, J. V. *Anal Chem* **2011**, *83*, 5804-5808.

(25) Abad-Villar, E. M.; Fernandez-Abedul, M. T.; Costa-Garcia, A. *Anal. Chim. Acta* **2002**, *453*, 63-69.

(26) Babula, P.; Huska, D.; Hanustiak, P.; Baloun, J.; Krizkova, S.; Adam, V.; Hubalek, J.; Havel, L.; Zemlicka, M.; Horna, A.; Beklova, M.; Kizek, R. *Sensors* **2006**, *6*, 1466-1482.

(27) Gimenes, D. T.; de Freitas, J. M.; Munoz, R. A. A.; Richter, E. M. *Electroanal.* **2011**, *23*, 2521-2525.

(28) Joseph, M. B.; Bitziou, E.; Read, T. L.; Meng, L.; Palmer, N. L.; Mollart, T. P.; Newton, M. E.; Macpherson, J. V. *Anal. Chem.* **2014**, *86*, 5238-5244.

(29) Lee, W.; Kwon, D.; Choi, W.; Jung, G. Y.; Jeon, S. *Scientific Reports* **2015**, *5*, 6.

(30) Toda, K.; Oguni, S.; Takamatsu, Y.; Sanemasa, I. *Journal of Electroanalytical Chemistry* **1999**, *479*, 57-63.

(31) Waldbaur, A.; Rapp, H.; Lange, K.; Rapp, B. E. *Analytical Methods* **2011**, *3*, 2681-2716.

(32) Santos, J. R.; Rangel, A. O. S. S. *Anal. Chim. Acta* **2012**, *715*, 57-63.

(33) Santos, J. R.; Rangel, A. O. S. S. *Food Chemistry* **2015**, *187*, 152-158.

(34) Zhang, Y.; Asahina, S.; Suzuki, M.; Yoshihara, S.; Shirakashi, T. *Surface and Coatings Technology* **2003**, *169–170*, 303-306.

(35) Kurzawa, J. *Anal. Chim. Acta* **1985**, *173*, 343-348.

(36) Mika, J.; Moreira, J.; Nemeckova, A.; Zima, J.; Barek, J.; Dejmkova, H. *Monatsh Chem* **2015**, *146*, 1211-1215.

(37) Junsomboon, J.; Jakmunee, J. *Talanta* **2008**, *76*, 365-368.

(38) Chi, Y.; Duan, J.; Lin, S.; Chen, G. *Anal Chem* **2006**, *78*, 1568-1573.

(39) Macpherson, J. V.; Jones, C. E.; Unwin, P. R. *The Journal of Physical Chemistry B* **1998**, *102*, 9891-9897.

(40) Macpherson, J. V.; Unwin, P. R. *Anal Chem* **1999**, *71*, 2939-2944.

(41) Kai, T.; Chen, S.; Monterroso, E.; Hailu, A.; Zhou, F. *Anal Chem* **2014**, *86*, 8037-8041.

(42) Melville, J. L.; Simjee, N.; Unwin, P. R.; Coles, B. A.; Compton, R. G. *The Journal of Physical Chemistry B* **2002**, *106*, 10424-10431.

(43) Mozo, J. D.; Carbajo, J.; Sturm, J. C.; Núñez-Vergara, L. J.; Salgado, P.; Squella, J. A. *Electroanal* **2012**, *24*, 676-682.

(44) Radulescu, M.-C.; Bucur, B.; Bucur, M.-P.; Radu, G. L. *Sensors (Basel, Switzerland)* **2014**, *14*, 1028-1038.

(45) Samphao, A.; Butmee, P.; Jitcharoen, J.; Švorc, Ľ.; Raber, G.; Kalcher, K. *Talanta* **2015**, *142*, 35-42.

(46) Vishnu, N.; Kumar, A. S.; Pillai, K. C. *Analyst* **2013**, *138*, 6296-6300.

(47) Anzalone, A.; Lizardi-Ortiz, J. E.; Ramos, M.; De Mei, C.; Hopf, F. W.; Iaccarino, C.; Halbout, B.; Jacobsen, J.; Kinoshita, C.; Welter, M.; Caron, M. G.; Bonci, A.; Sulzer, D.; Borrelli, E. *The Journal of Neuroscience* **2012**, *32*, 9023-9034.

(48) Bitziou, E.; Joseph, M. B.; Read, T. L.; Palmer, N.; Mollart, T.; Newton, M. E.; Macpherson, J. V. *Anal Chem* **2014**, *86*, 10834-10840.

(49) Snowden, M. E.; Unwin, P. R.; Macpherson, J. V. *Electrochemistry Communications* **2011**, *13*, 186-189.

(50) Bitziou, E.; Snowden, M. E.; Joseph, M. B.; Leigh, S. J.; Covington, J. A.; Macpherson, J. V.; Unwin, P. R. *Journal of Electroanalytical Chemistry* **2013**, *692*, 72-79.

(51) Mbogoro, M. M.; Snowden, M. E.; Edwards, M. A.; Peruffo, M.; Unwin, P. R. *The Journal of Physical Chemistry C* **2011**, *115*, 10147-10154.

(52) Myland, J. C.; Oldham, K. B. *Anal Chem* **2000**, *72*, 3972-3980.

(53) Bertoncello, P.; Ciani, I.; Li, F.; Unwin, P. R. *Langmuir* **2006**, *22*, 10380-10388.

(54) Müller, H.; Frey, B.; Böhme, W. *Fresenius J Anal Chem* **1991**, *341*, 647-649.

(55) Stefano, J. S.; Montes, R. H. O.; Richter, E. M.; Muñoz, R. A. A. *Journal of the Brazilian Chemical Society* **2014**, *25*, 484-491.

(56) Pickles, C. S. J. *Diamond and Related Materials* **2002**, *11*, 1913-1922.

(57) Hutton, L. A.; Iacobini, J. G.; Bitziou, E.; Channon, R. B.; Newton, M. E.; Macpherson, J. V. *Anal. Chem.* **2013**, *85*, 7230-7240.

(58) Compton, R. G.; Banks, C. E. *Understanding Voltammetry*, 2nd ed.; Imperial College Press: London, 2011.

(59) Bard, A. J.; Faulkner, L. R. *Electrochemical Methods: Fundamentals and Applications*, 2nd ed.; John Wiley & Sons: New York, 1980.

(60) Bae, A. J.; Beta, C.; Bodenschatz, E. *Lab Chip* **2009**, *9*, 3059-3065.

(61) Karlberg, B.; Pacey, G. E. *Flow Injection Analysis: A Practical Guide*; Elsevier Science, 1989.

(62) Bishop, G. W.; Satterwhite, J. E.; Bhakta, S.; Kadimisetty, K.; Gillette, K. M.; Chen, E.; Rusling, J. F. *Anal Chem* **2015**, *87*, 5437-5443.

(63) Cerda, V.; Ferrer, L.; Avivar, J.; Cerda, A. *Flow Analysis: A Practical Guide*; Elsevier Science, 2014.

(64) Taylor, G. *Dispersion of Soluble Matter in Solvent Flowing Slowly through a Tube*, 1953; Vol. 219, p 186-203.

(65) Aris, R. *On the Dispersion of a Solute in a Fluid Flowing through a Tube*, 1956; Vol. 235, p 67-77.

(66) Ananthakrishnan, V.; Gill, W. N.; Barduhn, A. J. *AIChE Journal* **1965**, *11*, 1063-1072.

(67) Stewart, K. K.; Beecher, G. R.; Hare, P. E. *Analytical Biochemistry* **1976**, *70*, 167-173.

(68) Růžička, J.; Hansen, E. H. *Anal. Chim. Acta* **1978**, *99*, 37-76.

(69) Kolev, S. D. *Anal. Chim. Acta* **1995**, *308*, 36-66.

(70) Reijn, J. M.; Poppe, H.; Van der Linden, W. E. *Anal Chem* **1984**, *56*, 943-948.

(71) Wentzell, P. D.; Bowdridge, M. R.; Taylor, E. L.; MacDonald, C. *Anal. Chim. Acta* **1993**, *278*, 293-306.

(72) Painton, C. C.; Mottola, H. A. *Anal. Chim. Acta* **1983**, *154*, 1-16.

(73) Brooks, S. H.; Leff, D. V.; Hernandez Torres, M. A.; Dorsey, J. G. *Anal Chem* **1988**, *60*, 2737-2744.

(74) DeLon Hull, R.; Malick, R. E.; Dorsey, J. G. *Anal. Chim. Acta* **1992**, *267*, 1-24.

(75) Davey, D. E.; Mulcahy, D. E.; O'Connell, G. R. *Electroanal* **1993**, *5*, 581-588.

(76) van der Linden, W. E. *TrAC Trends in Analytical Chemistry* **1987**, *6*, 37-40.

(77) Chan, C.-Y.; Guo, J.; Sun, C.; Tsang, M.-K.; Tian, F.; Hao, J.; Chen, S.; Yang, M. *Sensors and Actuators B: Chemical* **2015**, *220*, 131-137.

(78) Miller, J. N.; Miller, J. C. *Statistics and Chemometrics for Analytical Chemistry*, 5th ed.; Pearson Education Limited: London, 2005.

(79) van der Linden, W. E. *TrAC Trends in Analytical Chemistry* **1982**, *1*, 188-191.

(80) Wu, Z.-Q.; Du, W.-B.; Li, J.-Y.; Xia, X.-H.; Fang, Q. *Talanta* **2015**, *140*, 176-182.

Chapter 5 Electrochemical Flow Injection Analysis of Hydrazine in an Excess of an Active Pharmaceutical Ingredient

Despite the critical importance of monitoring genotoxic impurities (GIs) in the pharmaceutical industry, many of the current approaches are time consuming and costly in terms of both staff and instrument resource. In this work we employ a Pt nanoparticle (NP) functionalised, boron doped diamond (BDD) microband electrode, inlaid into insulating diamond as a surround. This sensor is combined with a flow injection analysis (FIA) flow cell, designed specifically for trace analyte detection. We demonstrate the determination of the genotoxic impurity, hydrazine (HZ), down to 0.274 parts per millions (ppm) with respect to 50 mM acetaminophen (ACM) – an electrochemically active pharmaceutical ingredient (API), surpassing the required safe guidelines set by the pharmaceutical industry for the quantitation of genotoxic impurities.

5.1 Introduction

The determination of GIs is of critical importance to the pharmaceutical industry in order to uphold the safety and quality of drug substances.[1] Due to their carcinogenicity and mutagenicity, they must be quantified and ultimately removed down to 'safe levels' in the presence of the API.[2] This corresponds to 1.5 μg/day exposure or 1 ppm of GI with respect to the mass of the API.[3] Of the wide variety of GIs, HZ is particularly troublesome,

as aside from being a useful pharmaceutical reagent, HZ and HZ-derivatives are class 1 GIs (known mutagens and carcinogens)[3] and are difficult to quantify due to their high volatility, high polarity, low molecular weight and lack of chromophore.[4]

Therefore, a wide variety of techniques have been evaluated for HZ quantitation[1,4] (Table 1.2) and derivatization is often employed in the analysis process, whereby HZ is reacted with a species such as acetone[5] or benzaldehyde[6-8] to enable detection. Furthermore, some approaches also utilize a pre-concentration step, for example liquid-liquid extraction (LLE) to facilitate detection.[6] Many of these methods require long analysis times, high cost of instrumentation and are difficult to operate in-line, adding to the overall cost of drug development. Furthermore, whilst the required detection limits are sometimes less stringent for shorter periods of exposure to the GI, many approaches do not reach the required LOD (~1 ppm), compared to the amount of API, as stipulated by pharmaceutical guidelines.[3]

Herein, an insulating diamond sealed BDD microband electrode, functionalised with Pt NP, is employed for the trace determination of HZ in the presence of a large excess of ACM – an electrochemically active API. Functionalisation with Pt NP is shown to shift the electrochemical signatures of HZ and ACM to separate their responses, as discussed in chapter 3. This electrode is used for FIA with electrochemical detection (FIA-EC), using an optimised system designed specifically for trace detection, as discussed in chapter 4. This combined approach importantly does not require derivatization or LLE of the GI, as in e.g. HPLC or GC-MS analysis. We also report on the stability of the metal NPs under FIA-EC conditions and show that through optimization of the flow cell and the electrode geometry, HZ can be quantified down to sub-ppm levels, with respect to ACM, present in excess (50 mM). This approach holds considerable promise for on-line analysis and is applicable to a wide range of electroactive GIs, in the presence of excess API.

5.2 Results and Discussion

The FIA system used within this chapter is that characterised in the previous chapter (chapter 4). As a reminder, the flow cell has a channel height ($2h$) = 22.5 μm, width (w) = 3 mm and the inlaid BDD band electrode has a width (x_e) of 89 μm, as shown in Figure 5.1.

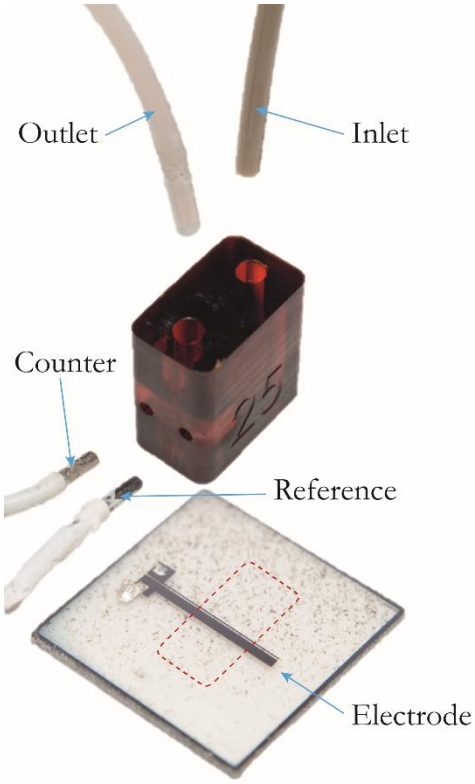

Figure 5.1 Illustration of flow cell and BDD microband electrode – adapted from Figure 4.8.

5.2.1 Hydrazine Detection on Boron Doped Diamond

Before assessing the FIA response with the Pt NP modified electrode, it is worth first considering this functionalisation. Electrode modification usually increases the complexity and cost of the system, therefore it is prudent to ask; why not use un-functionalised BDD? This is especially significant as recent studies in the last twelve months have shown the use of BDD with FIA to determine for example; hydrogen sulphide,[9] niacin,[10] hydroquinone,[11] yohimbine,[12] norepinphrine,[13] Zn and Pb.[14] HZ has also been determined by Sun *et al.*

using FIA with a BDD electrode, achieving a limit of detection (LOD) of 0.999 μM.[15] Linear sweep voltammetry (LSV) of HZ (0, 0.5 and 1 mM) in stationary solution on an 89 μm wide all diamond microband BDD electrode *vs* an Ag/AgCl reference electrode is shown in Figure 5.2 below.

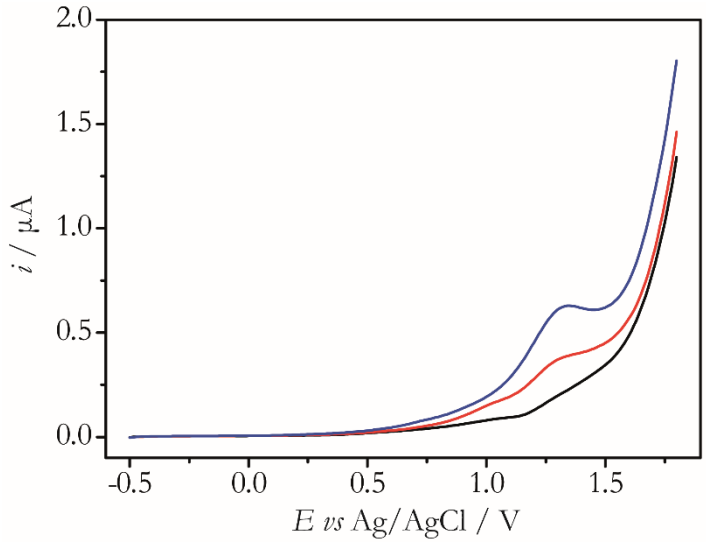

Figure 5.2: LSV of 0 (—), 0.5 (—) and 1 mM HZ (—), on an 89 μm width BDD microband electrode in 0.1 M phosphate buffer solution (PBS, pH 6.9), scan rate = 0.1 V s^{-1}.

Note that the voltammetry is conducted in stationary solution inside the FIA flow cell to define the electrode area. The HZ occurs as expected at 1.3 V *vs* SCE. In order to investigate this further under hydrodynamic conditions, 50 μL injection of 0 - 100 μM HZ were studied via FIA in this same flow cell as shown in Figure 5.3. This results in a LOD (equation 3.1, mean of blank response + three times standard deviation of the background response peak current)[16] of 0.97 μM. This implies that trace HZ quantitation in the presence of a large excess of ACM (the API) should be possible on plain BDD.

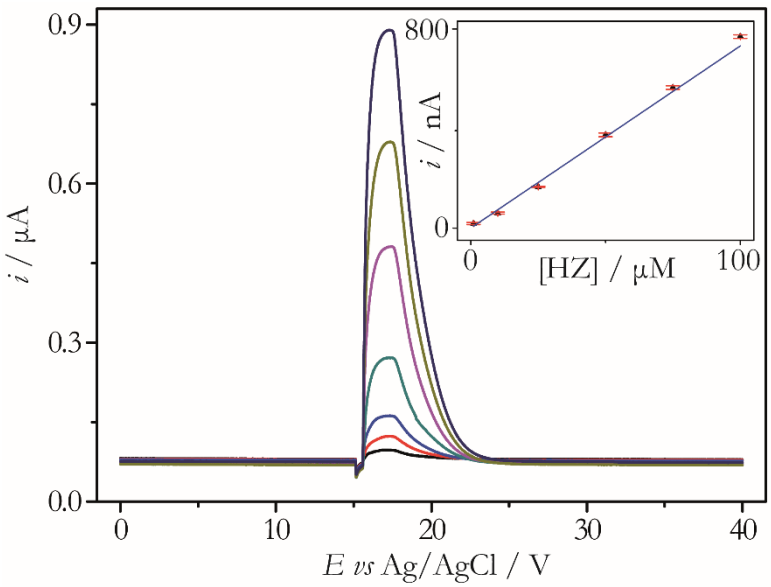

Figure 5.3: FIA of 0, 1, 10, 25, 50, 75 and 100 μm HZ in 0.1 M PBS (pH 6.9), on an 89 μm width BDD microband electrode held at 1.4 V *vs* SCE, V_f = 1 ml min^{-1}.

However, even in the absence of matrix effects (other species in solution such as the API effecting the GI electrochemical response – section 3.2.4.1), the API will complicate HZ determination as i) when the API signature occurs before or near that of the GI (E_p ACM = +0.74 V *vs* SCE – Figure 3.9) the background variance and hence LOD will increase, also ii) when an excess of API is present, the GI signature can be engulfed by that of the API.

This last point is corroborated by cyclic voltammetry (CV) with 50 mM ACM at 1 ml min^{-1} as shown in Figure 5.4. Due to the large currents passing through a small cross-sectional area channel (0.075 mm^2) between the working and reference electrodes (1 mm diameter Pt wire placed in the flow cell outlet – Figure 5.1), ohmic behaviour is observed (resistance in solution R_s = 8366 Ω) above the onset potential for ACM oxidation *ca* ~ 0.5 V. This effect could be reduced by increasing background electrolyte concentration or using a larger flow cell channel height (equation 4.3), though this would act detrimentally on the analytical signals (Levich equation 1.44) and thus trace detection ability of the

system. Hence plain (un-functionalised) BDD cannot be employed for HZ determination in the presence of ACM with the system employed herein.

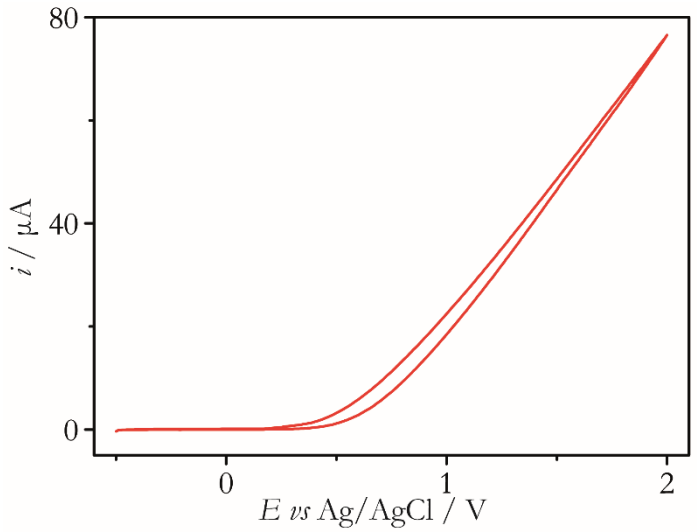

Figure 5.4: CV of 50 mM ACM in 0.2 M PBS (pH 6.9), on an 89 μm width BDD microband, V_f = 1 ml min^{-1}.

5.2.2 Hydrazine and Acetaminophen Voltammetry at Pt Nanoparticle Functionalised Boron Doped Diamond

Based on these results, BDD electrodes alone cannot be used to electrochemically resolve the two species. Hence to differentiate the electrochemical oxidation signatures for HZ and ACM, it is thus important that the significantly smaller HZ electrochemical signal is found at a potential less positive than that of ACM. E_p for HZ and ACM oxidation are observed at -0.16 V and +0.42 V *vs* SCE respectively on Pt (Figure 3.4, 3.9). Hence by changing the identity of the electrode, it should be possible to shift $E_{1/2}$ such that the HZ signature occurs well before that of ACM. To achieve the required LOD it is preferable to work with Pt NP modified BDD electrodes rather than Pt electrodes, due to the inherently higher background signals of the latter.

To verify electrochemical resolution of the HZ and ACM EC signals, linear sweep voltammograms (LSVs) were recorded at 0.1 V s^{-1} in a stationary solution (housed within

the flow cell) containing 1 mM HZ in 0.2 M PBS (—) and 50 mM ACM in 0.2 M PBS (—), as shown in Figure 5.5. Deposition of Pt NPs was achieved by holding the BDD electrode at -1 V *vs* Ag/AgCl for 1.5 s in a solution of 1 mM PtK_2Cl_6 in 0.1 M H_2SO_4. For HZ oxidation, the current reaches a steady state at ~ 0.2 V, whilst a current does not begin flowing for ACM oxidation, present in much higher concentration, until ~ 0.15 V.

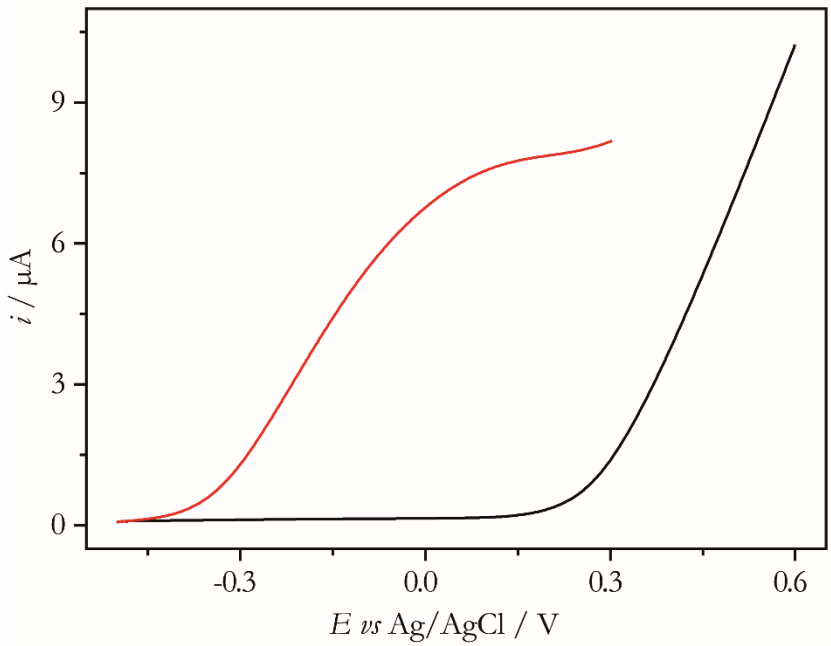

Figure 5.5: LSV of 1 mM HZ (black line) and 50 mM ACM (dotted black line), both in 0.2 M PBS at 0.1 V s^{-1}, recorded at a Pt NP-BDD microband electrode in stationary solution (confined within the microfluidic flow cell).

5.2.2 Stability of Nanoparticles in Flow

It is essential that under the flow conditions utilized, the electrochemically deposited NPs are stable and not prone to detachment, as this could lead to decreasing signals and erroneous analysis with extended use.[17] Some researchers have claimed a weak attachment between a BDD surface and metal NPs,[18] however it is essential to take into account surface morphology and wettability. For example, on hydrophilic polished microcrystalline surfaces of the type employed here, Pt NPs on BDD have been found to be extremely stable in quiescent solutions.[19] To explore NP stability on the BDD microband electrode

under the relatively high V_f conditions of the microfluidic flow cell and over reasonable experimental timescales (1 - 2 hours), CVs were recorded in 0.1 M H_2SO_4 at V_f = 1 ml min^{-1} and 10 V s^{-1}, every 10 minutes for 2 hours. Figure 5.6 shows the first CV recorded.

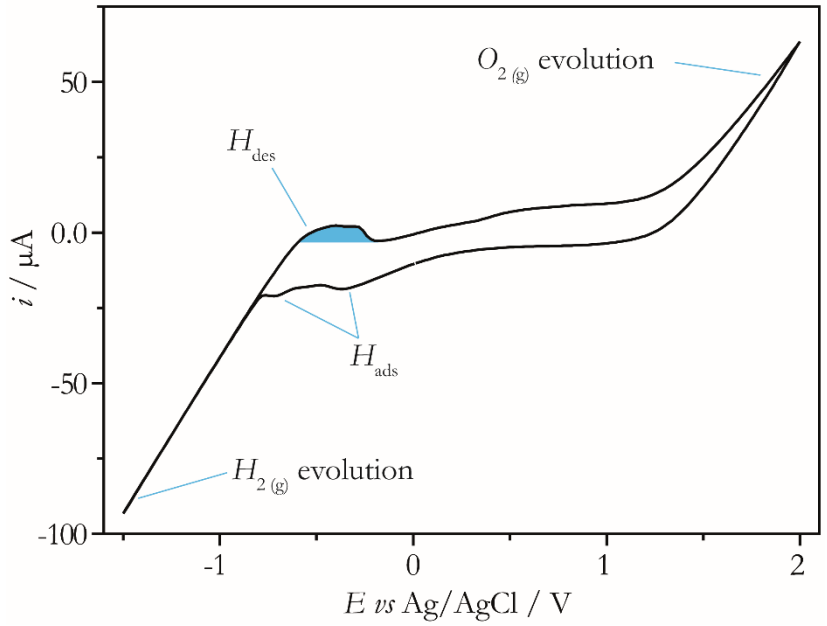

Figure 5.6. CV of the Pt NP-BDD microband electrode recorded in 0.1 M H_2SO_4 at 10 V s^{-1} and V_f = 1 ml min^{-1}.

Clearly evident are two typical hydrogen adsorption peaks (H_{ads}) at -0.4 and -0.7 V *vs.* Ag/AgCl, as well as a broad hydrogen desorption peak (H_{des}) at *ca.* -0.5 V (blue shaded region). As has previously been shown, these features can be used to characterize the surface, as the area under these peaks corresponds to the absorption/desorption of a monolayer of hydrogen atoms.[17] Note that at the potential extremes, resistive current signatures for both hydrogen evolution (< -0.8 V) and oxygen evolution (> 1.2 V) are seen, due to a combination of the high currents passed in conjunction with the placement of the counter and reference within the flow cell outlet and the small cross sectional area of the channel. For the eleven subsequent CVs recorded over 2 hours, the area under the H_{des} peak was found to remain relatively constant, 0.208 ± 0.014 μC, suggesting that the Pt NPs were stable under flow. Additionally, assuming that one hydrogen atom adsorbs on one atom of the Pt surface and that the density of atoms on a Pt surface is 1.31 × 10^{-}

^{15} atom cm^{-2}, the charge per unit area is 210 μC cm^{-2}.^{20} Therefore, based on an average NP geometry of a 14 nm radii hemisphere (calculated by AFM – not shown), the density of Pt NP on the surface of the BDD band electrode is 301 ± 20 NP μm^{-2}, which is reasonable considering previous studies of Pt NP-BDD under similar deposition conditions (130 NP μm^{-2} - 340 NP μm^{-2} between more and less active grains of BDD).^{19} To further verify Pt NP stability under channel flow, FE-SEM was employed to characterize the electrode surface before and after continuous flow.

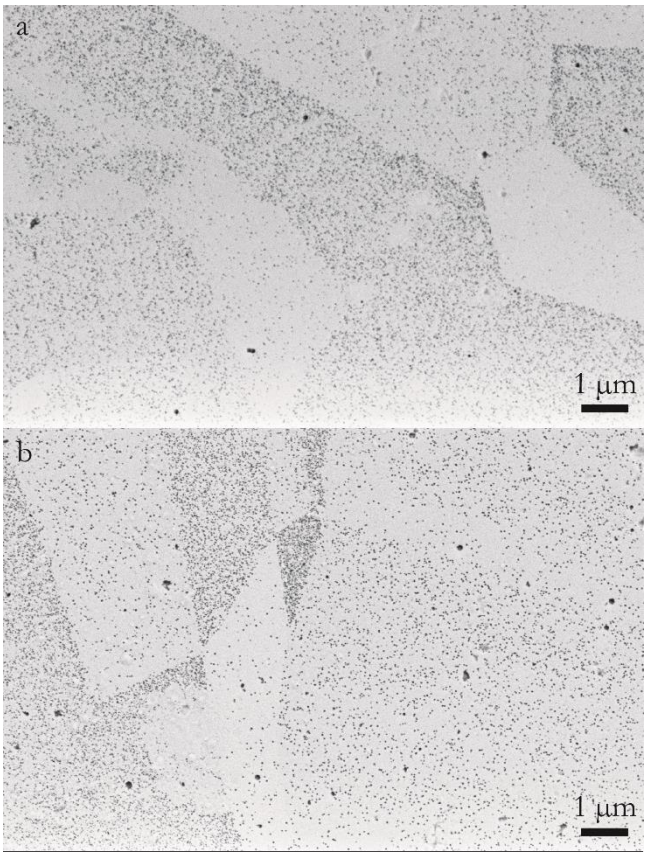

Figure 5.7: Representative FE-SEM images of the Pt NP-BDD band electrode with a secondary electron detector a) immediately after electrochemical deposition, under stationary conditions and b) after one hour of flowing continuously over the electrode at V_f = 1 ml min^{-1} with 0.2 M PBS. Note the images have been reverse colour contrasted to enhance visualization of the Pt NPs (black spots).

EC was carried out using a droplet (15 μL) of 1 mM PtK_2Cl_6 in 0.1 M H_2SO_4, placed on top of the BDD band electrode. The electrode was then prepared for FE-SEM by

washing gently with water and drying in air. A typical (n = 4) 9 μm × 6 μm image of the surface area prior to solution flow is shown in Figure 5.7a. After imaging, the electrode was placed in the flow cell and 0.2 M PBS flown over at V_f = 1 ml min^{-1} for one hour, before repeat FE-SEM imaging using the same magnification. A representative image (n = 4) after flow is shown in Figure 5.7b.

It is interesting to note that in both images slightly different densities of Pt NP are observed across different areas of the BDD surface, as has been observed previously.[19,21] This is due to the differently doped regions of the polycrystalline surface, where slightly higher densities of NPs are observed at the more highly doped grains.[22] The FE-SEM images clearly show that a significant number of NPs are still present after being subject to hydrodynamic flow. The FE-SEM images were analyzed in MATLAB using a circle finding script ('imfindcircles'), in order to obtain NP density for each image.

Quantitatively, it was found that the NP density does not change after flow (*i.e.* before 54.9 ± 3.7 NP μm^{-2}, n = 4 and after flow 55.6 ± 3.6 NP μm^{-2}, n = 4). Both the CV and microscopic data indicate that the NPs are stable under the flow conditions used in this study. It is interesting to note that this method determines a lower NP density in comparison to the CV approach. This is most likely due to the circle finding script not being able to identify the smallest NPs, which are difficult to resolve using FE-SEM.

5.2.3 Hydrazine Quantitation in the Presence of Acetaminophen by Flow Injection Analysis

From the LSV data in Figure 5.5, for FIA-EC detection of HZ in the presence of ACM, an electrode potential of +0.10 V versus Ag/AgCl was chosen to maximize the signal HZ signal, whist avoiding any current contributions from ACM oxidation. As recently discussed,[23] HZ oxidation on Pt is sensitive to electrode pre-treatment and the presence of residual oxides on the electrode surface. In order to improve the reproducibility of the

HZ oxidative wave when repeat measurements are made, cleaning steps are often employed, for example sweeping between positive and negative potentials[24,25] or holding the surface at a constant potential.[26,27] Here, a CV was used whereby immediately after each injection, a CV was run at 0.5 V s^{-1} in the carrier stream between -0.40 V and +1.20 as shown in Figure 5.8 (initial and final potential = 0.1 V). This approach was found to give minimal change in HZ signal between repeat measurements and was thus adopted for HZ determination in the presence of ACM.

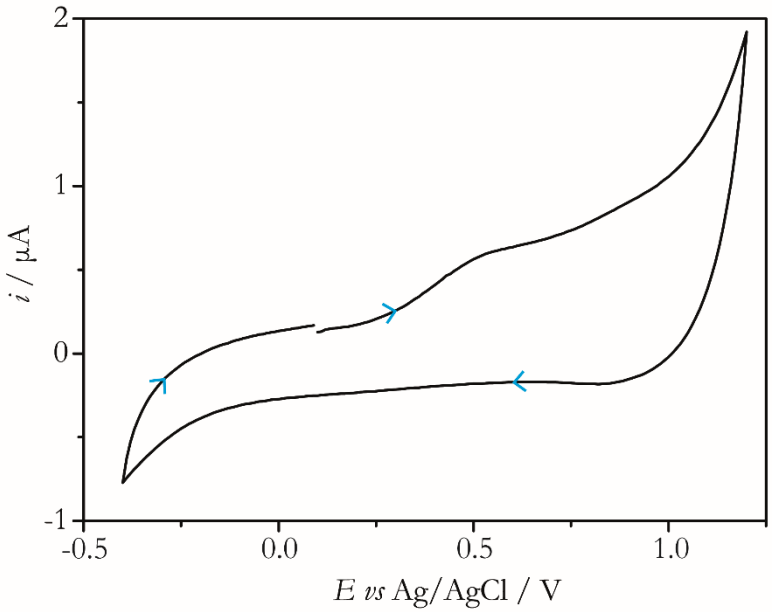

Figure 5.8: Cyclic voltammetry cleaning step at 0.5 V s^{-1} in the carrier stream (0.2 M PBS, pH 6.9, V_f = 1 ml min^{-1}) at a Pt NP-BDD microband electrode, the blue arrows show the scan direction.

HZ concentrations in the range 0 – 100 μM in the presence of 50 mM ACM were injected (50 μL, n = 6 per concentration) into the continuous phase flow stream (0.2 M PBS pH 6.9, V_f = 1 ml min^{-1}) as shown in Figure 5.9. The peak current varies linearly with HZ concentration in the range 1 - 100 μM (Figure 5.9 inset), with a corresponding sensitivity of 0.337 μA $μM^{-1}$.

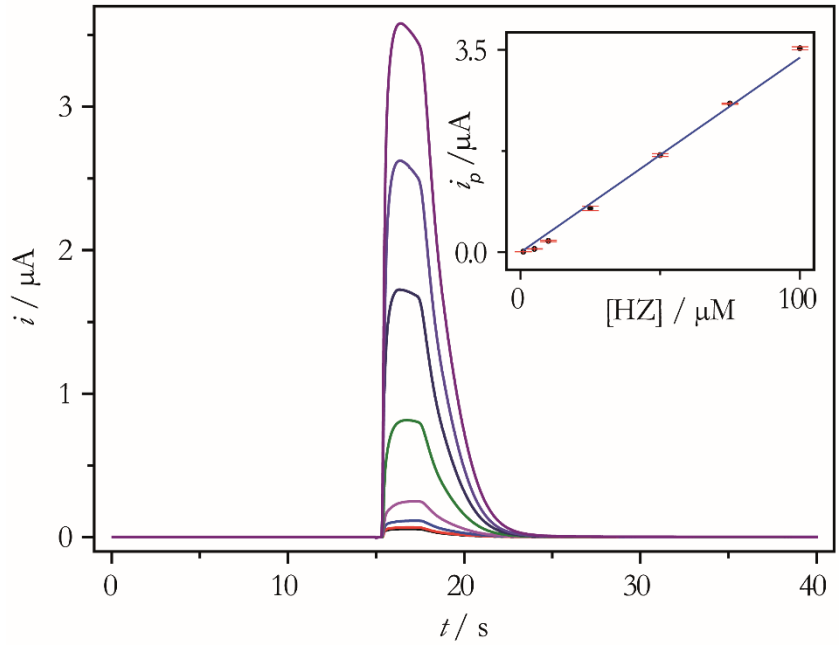

Figure 5.9: FIA-EC with an analyte solution containing 50 mM ACM and 0, 1, 5, 10, 25, 50, 75 and 100 μM of HZ. The Pt NP-BDD microband electrode was held at a potential of +0.1 V versus Ag/AgCl, and 50 μL volumes were injected into a 0.2 M PBS solution flowing at V_f = 1 ml min^{-1}, (n = 6). Inset plot of i_p against concentration, R^2 = 0.993, sensitivity = 0.337 μA μM^{-1}, LOD = 64.5 nM (0.274 ppm).

This resulted in an LOD of 64.5 nM, which equates to 0.274 ppm (equation 1.1) of HZ with respect to the mass of ACM, well within the most stringent pharmaceutical guidelines for long term GI exposure.[3] Furthermore, this result compares favourably with alternate methods for HZ detection in the presence of APIs as depicted in Table 1.2, particularly as the approach utilized in this study does not require derivatization or liquid-liquid extraction. This LOD is also significantly smaller than that of differential pulse voltammetry (DPV, 11.01 μM, 2352 ppm) given in chapter 3, as expected due to the increased mass transport from convection. There is scope for reducing the LOD further by simply moving to higher V_f's, smaller height flow channels, thinner bands and more basic pH's[28] *etc.*

5.2.4 Future Studies

It is prudent to consider the progress made towards the thesis aims and highlight further areas of investigation, which result from the work presented. The electrochemical response of HZ has been studied in detail in the presence of electrochemically active drugs, present in excess. The first used CV in stationary solutions, whilst the second implemented FIA-EC analysis to achieve pharmaceutical relevant detection levels i.e. down to ppm levels in the presence of the API. The remaining challenges are investigation of other electrochemically active GIs (in the presence of excess APIs), electrochemical detection of GIs in non-aqueous solvents and on-line quantitation of a GI during a synthetic reaction in real time.

5.2.4.1 Other Genotoxic Impurities and Active Pharmaceutical Ingredients

This thesis focussed on one particular GI – HZ and two APIs – ACM and PZ. However, the approaches discussed are applicable to any GIs (and APIs) that are electrochemically active. Of the GI structural alerts listed in Figure 1.1, several of these groups are known to be electrochemically active, such as hydrazine's, alkyl halides,[29] sulfonate esters,[30] epoxides,[31] *N*-nitrosamines,[32] aminophenols,[33] aldehydes,[34] urethanes,[35] N-methylols[36] and N-mustards.[37] Furthermore, many APIs are known to be electroactive,[38,39] including many of the world's top selling drugs such as sildenafil,[40] vardenafil,[41] haloperidol,[42] fexofenadine,[43] erythromycin[44] and methotrexate.[45]

A major remaining challenge will be determination when the GI and API are similar in structure and thus quite likely similar in electrochemical detection potential. For example, the API isoniazid is a tuberculosis agent which contains a hydrazine functional group, as shown in Figure 5.10. It undergoes an irreversible two electron oxidation at around 0.85 V *vs* Ag/AgCl on a multiwalled carbon nanotube modified carbon paste

electrode.[46] Isoniazid is also important in the context of this work as HZ is a known degradation species from the drug.[47]

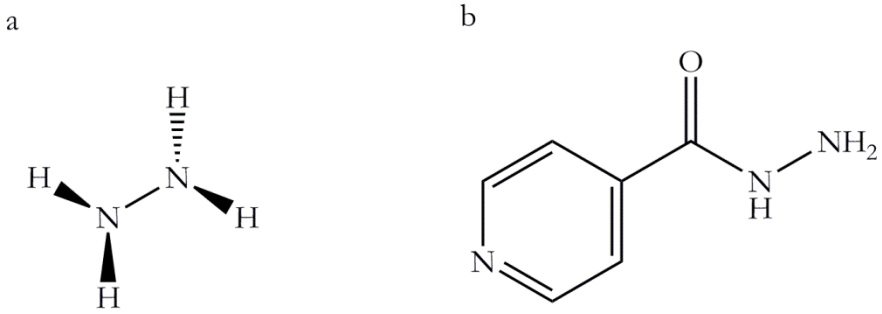

Figure 5.10: Structure of a) HZ and b) isoniazid

5.2.4.2 Electrochemistry in Non-Aqueous Solvents

One important factor not currently considered within this thesis is that of solvent. Whilst the vast majority of electrochemical studies are conducted in aqueous solution, organic syntheses operate in a wide range of solvents. This will complicate electrochemical analysis in two distinct ways. Firstly, the viscosity and diffusion coefficient will likely change, affecting the electrochemical response. Additionally, pharmaceutical mixtures may not contain an excess of ionic species (the background electrolyte in our systems) leading to migratory effects. Though common background electrolytes show poor solubility in many non-aqueous solvents, there are a range of salts designed for use in non-aqueous solvents such as tetrabutylammonium perchlorate.[48,49] It is interesting to note at this point that HZ has previously been quantified electrochemically in acetonitrile[48] dimtheylsulfoxide,[49] and methanol.[50]

Secondly, it is important that the electrodes and materials used e.g. the flow cell, are stable to the solvent. For example, any change in flow cell dimensions for the type of cell used in this chapter, through material instability (e.g. swelling), will change the dynamic response (equation 1.44). Therefore, with a view towards online detection, we propose two possible strategies for further investigation:

5.2.4.3 Electrochemical Detection in the Non-Aqueous Solvent

The first strategy is electrochemical detection in the non-aqueous solvent. One simple approach is to use the current microsteriolithography (MSL) flow cells with non-aqueous solvents. These flow cells are built by MSL from a methacrylate based photoactive resin (R11, EnvisionTec, UK). Whilst this material is known to be stable in aqueous solvents, its stability in other solvents is unknown. Therefore, this material, as well as an alternate material used for MSL design, known as 'high temperature resin' (HTM140, EnvisionTec, UK), were tested with a variety of common solvents as shown in Figure 5.11 below. Note that data for some of the tested solvents are not shown as they caused cracks or complete dissolution of the material (e.g. tetrahydrofuran and acetone).

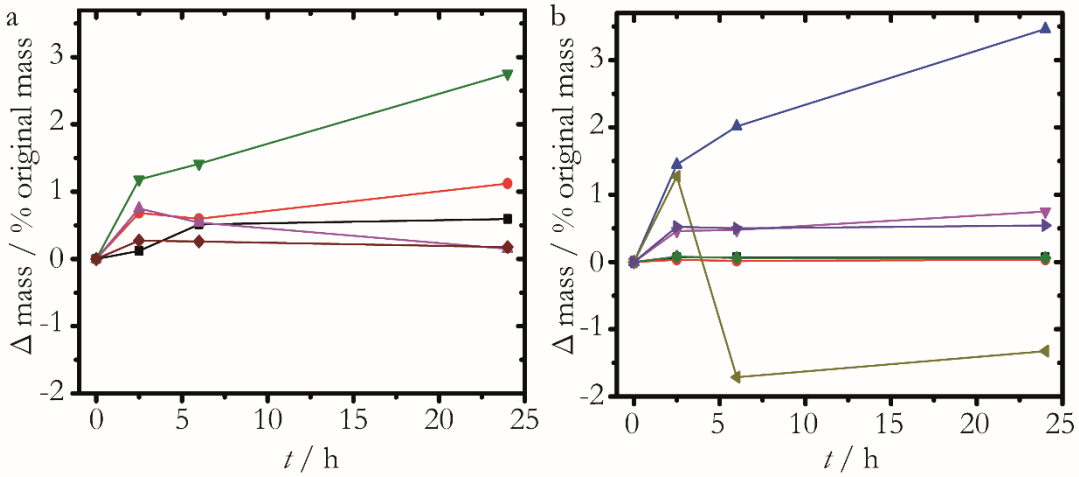

Figure 5.11 Material stability tests at 2.5, 6 and 24 hours, with a) methacrylate resin used for FIA flow cells within this thesis and b) high temperature resin compatible with the same fabrication procedure. Solvents are (—) water, (—) paraffin oil, (—) ethanol, (—) dodecane, (—) toluene, (—) acetonitrile, (—) dimethyl sulfoxide and (—) butan-1-ol.

The solvent stability was judged based on submerging a piece of manufactured flow cell into the solvent and testing the mass change initially, then after 2.5, 6 and 24 hours. The material was deemed to be 'stable' if a less than 3% loss/gain in mass was observed (through the material adsorbing solvent or dissolving into the solvent). The final results are summarized in Table 5.1 below.

Solvent	Methacrylate resin % change in mass	High temperature resin % change in mass
acetone	-[a]	6.568
acetonitrile	-[a]	3.463
ethanol	2.751	0.750
butan-1-ol	-[a]	0.544
Water	0.592	0.068
dodecane	0.177	0.060
paraffin oil	0.150	0.032
dimethyl sulfoxide	-[a]	-1.325
toluene	1.122	-9.493
tetrahydrofuran	-[a]	-30.030

Table 5.1: Summary of solvent stability tests with resins for FIA flow cells, a) material infested with cracks such that cell broken into multiple pieces or complete dissolution of the material.

In conclusion; water, dodecane, paraffin oil and toluene could be used with the current FIA flow cells and possibly ethanol. Moving to the new flow cell material would open up experiments with butan-1-ol, dimethyl sulfoxide and possibly acetonitrile. Of course, moving to other manufacturing approaches aside from MSL would open up the use of a wider range of materials, for example glass, Teflon, steel or diamond which would likely have greater solvent stability, but would lose the MSL advantage of a simple bespoke design.

5.2.4.4 Detection Through Partitioning / Extraction

As previously mentioned (Table 1.2), several current strategies for GI detection in the presence of APIs in the pharmaceutical industry utilise liquid-liquid extraction (LLE) to facilitate detection.[6] In short, this involves partitioning of the GI from the initial solvent to an immiscible one for detection, as shown in Figure 5.12.

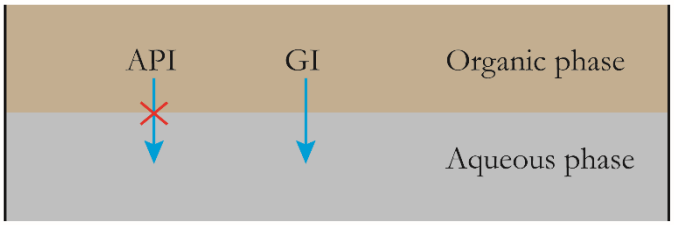

Figure 5.12: Illustration of liquid-liquid extraction of a GI from an organic to aqueous solvent.

Based on the solubilities of the GI, API and other species in the two solvents, one can then separate the GI into the new solvent for detection. Ideally, the API will not be soluble in the aqueous solvent, but even in the event of partial solubility; so long as the GI ratio of solubilities is greater than that of the API, detection will be enhanced. Though this process is often operated off-line (i.e. by synthetic chemists with a separating funnel or HPLC column), it can easily be adapted for on-line analysis using e.g. microfluidics.

One approach to achieving analyte partitioning between two immiscible solutions is illustrated in Figure 5.13. Organic and aqueous streams are passed alongside each other in a channel (Figure 5.13a). The solvents are immiscible and the flow is laminar, such that the streams stay separate (do not mix). In fact, even when the solvents are miscible (e.g. water and acetonitrile), extraction can still be carried out across a stable liquid-liquid boundary due to the well-defined hydrodynamics and increased insolubility from the high background electrolyte concentrations in the water phase.[51,52] Partitioning of the GI occurs at the interface between the solvents and is detected downstream at a gold band electrode as shown in Figure 5.13b. One major advantage of this approach is that the aqueous phase can contain background electrolyte and buffer, such that the organic solvent does not need to be modified to enable GI detection (section 5.2.4.2). Depending on the entrance length, cell geometry and flow rate, measurement of small concentrations of analyte partitioning across should be possible. This approach is promising in that one can imagine recirculation of a reaction mixture whilst analysing and subsequently removing a GI in real time.

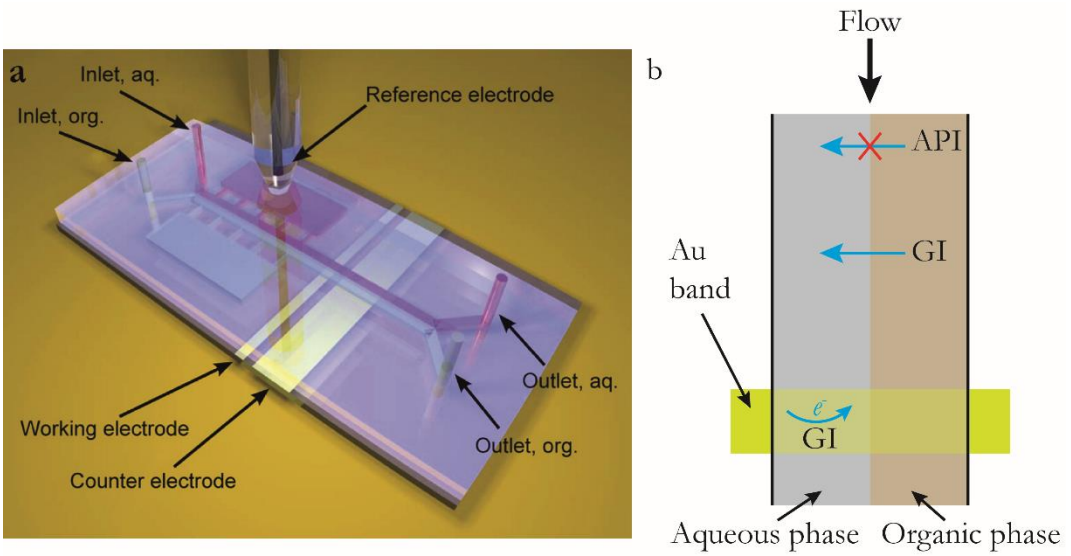

Figure 5.13: Two phase microfluidic partition system with a) schematic of typical setup[53] and b) illustration of GI partition from an organic to an aqueous phase and subsequent oxidation downstream.

Another approach is that of microfluidics droplets (also known as two phase segmented flow).[54] There are various droplet generation methods[55] and one of the most basic and common is via a T-junction,[56,57] as shown in Figure 5.14 for water droplet generation in an oil continuous phase. The general principle is as follows: one phase (in this case oil) is flowed down a channel at a relatively fast flow rate and another phase (in this case water) is flowed perpendicularly into this channel at a slower flow rate, as shown in Figure 5.14a. Due to the partial pressures between the phases, the water phase pushes out into the channel, then is pinched off as the pressure from the oil phase becomes too great (and to minimise the surface tension).

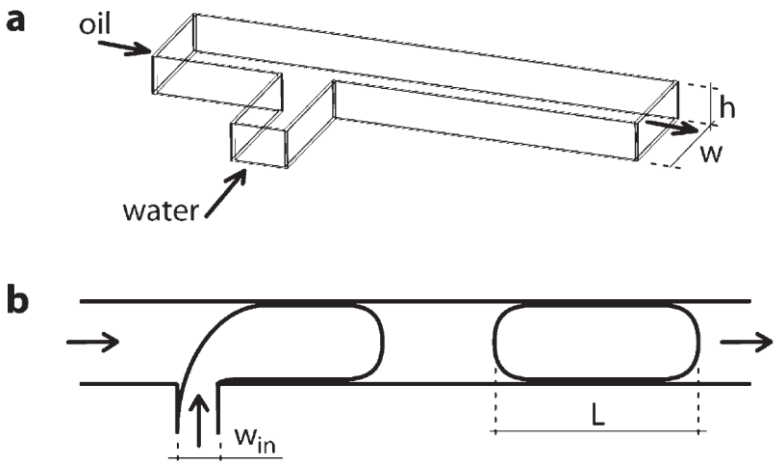

Figure 5.14: Formation of droplets in a microfluidic T-junction, a) illustration of geometry and b) illustration of droplet formation, the electrode will be located downstream e.g. as in Figure 5.12a.[57]

Depending on the droplet size and inter-droplet separation, extra convective transport (a turnover effect) is observed inside the droplets and in the other phase between droplets, such that partition between the phases is enhanced.[58] This is shown schematically in Figure 5.15, with GI partition from an organic droplet into an aqueous stream. Additionally, depending on the specifics of the system; water droplets with an organic continuous phase or vice versa could be operated to facilitate detection.

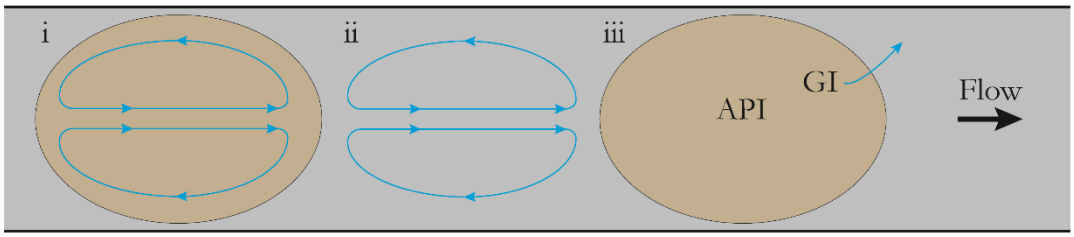

Figure 5.15: Convective 'turnover' i) inside droplets and ii) between droplets leading to iii) enhanced extraction between the solvents, determined by a band electrode located downstream.[58]

Initial tests along this avenue investigated HZ partitioning from paraffin oil droplets into an aqueous phase containing 0.1 M phosphate buffer solution (PBS, pH 6.9) with 0.2 M KNO_3. These were generated using flow rates of V_f = 1 μL min^{-1} and V_f = 1 μL min^{-1} for the aqueous and paraffin oil inlets respectively, with a syringe pump (Kd Scientific,

USA). A PDMS channel (200 μm width by 150 μm height) was fabricated as described in section 2.2.4 and shown below in Figure 5.16. A T-junction injection system was used (Figure 5.16a,b) with an 80 μm width Au band reference electrode, a 40 μm width Au band working electrode and a 400 μm width Au band counter electrode located (in this order) downstream in the channel (Figure 5.16c).

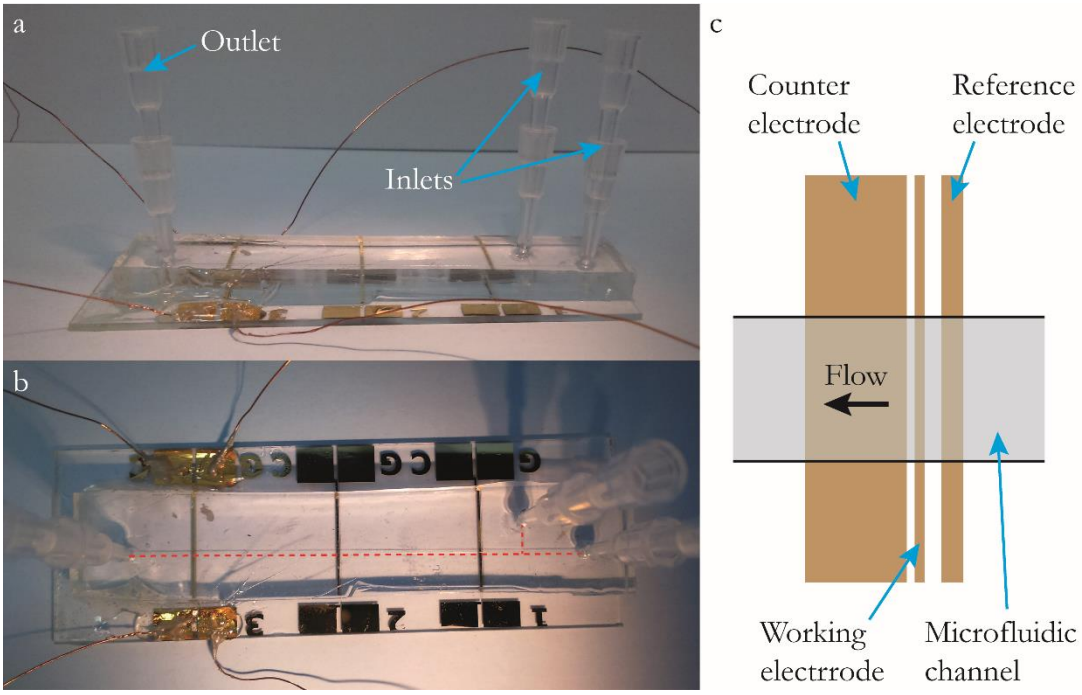

Figure 5.16: A droplet-microfluidic cell, using a T-junction droplet generation method, channel dimensions are 200 μm width by 150 μm height. a) and b) show the side and top view respectively, note the channel is highlighted with a dashed red line in b, c) shows a schematic of the Au band working (w = 40 μm), reference (w = 80 μm) and counter (w = 400 μm) electrodes.

Initial experiments with this setup for HZ hydrate partitioning from paraffin oil droplets into an aqueous phase are shown in Figure 5.17. The Au working electrode was held at 0.8 V *vs* Au to oxidise any extracted HZ. Note HZ hydrate is used rather than sulphate as it was found to be more soluble in the paraffin oil.

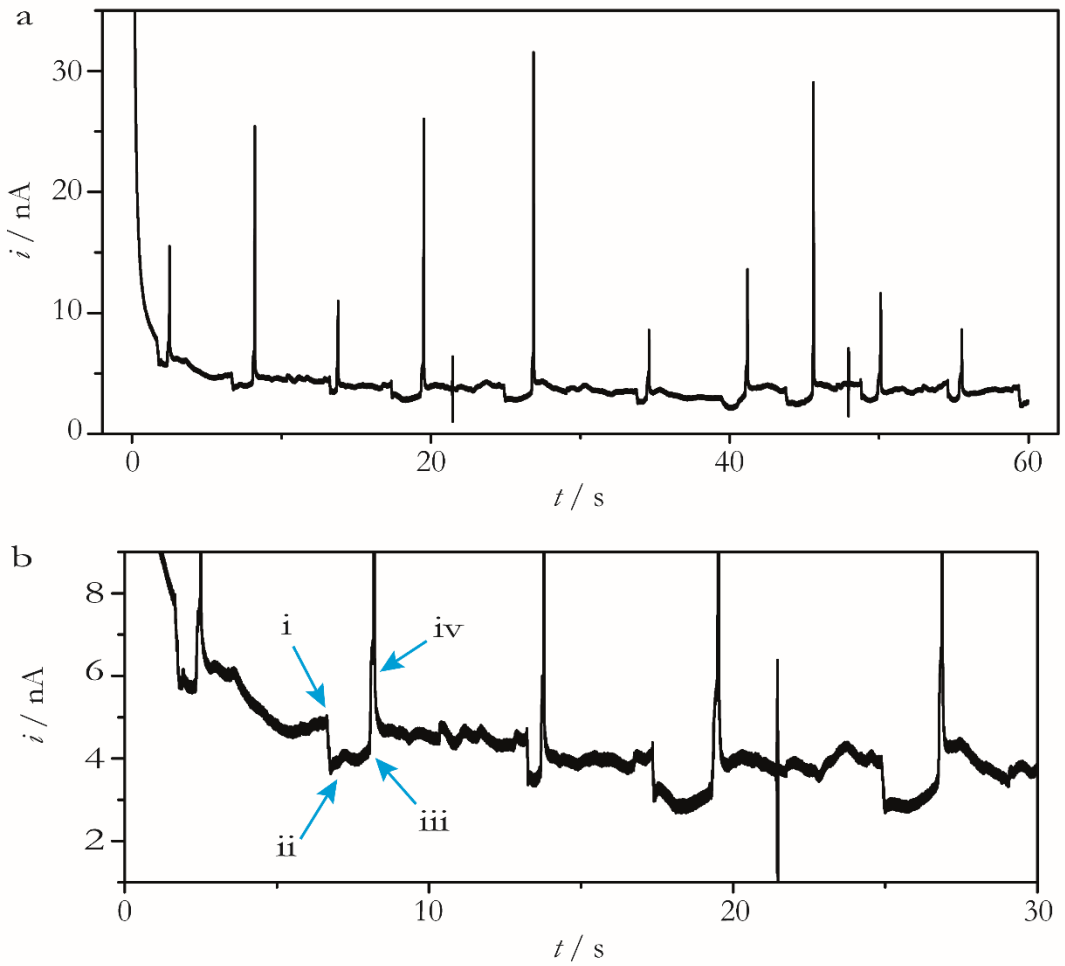

Figure 5.17: Current traces for partition of 1 mM HZ from paraffin oil droplets to an aqueous stream of 0.1 M phosphate buffer solution (PBS, pH 6.9) with 0.2 M KNO_3, the Au microband electrode was held at 0.8 V *vs* Au, b) shows a zoom in of the trace in a), the front of the droplet reaches the electrode at i) then passes at iv).

From these results, it is clear that the droplets cause a noticeable effect on the *i-t* traces (Figure 5.17b, i-iv). However, without further experimentation, an exact explanation of the current trace is not possible. We can, though, speculate that the initial drop in current as the droplet reaches the electrode (i) is due to either charging of the double layer or blocking of the electrode (as the oil phase contains no background electrolyte). At ii) the current starts to increase as HZ partitions out and is turned over. Finally, at iii) the droplet passes such that the double layer reforms and a capacitive spike is seen decaying to a baseline value (iv). Further experiments would seek to investigate partitioning with

different sized droplets and droplet-droplet gaps, different flow rates and partition with varying HZ concentrations (including zero), before applying this system for the trace detection of HZ, perhaps in the presence of isoniazid (section 5.2.4.1).

In these investigations, the partitioning of a species between two solvents can be estimated from the solubility constants in the different species. It can also be calculated by simply mixing equal volumes of the two solvents in a separating funnel. By starting with the species of interest in one phase and measuring the final concentration in the new phase (by for example LSV with a Pt ultramicroelectrode), the partitioning can be quantified. Whilst this infers on the thermodynamics of partitioning, it does not explain the kinetics of this process i.e. how fast is partitioning across the liquid-liquid interface?

Microelectrochemical measurements at expanding droplets (MEMED), is a technique for studying the kinetics of interfacial transfer between two immiscible liquids and is ideal for quantifying LLE processes before implementation in a fluidic device.[59-61] In short, a capillary is positioned opposite an ultramicroelectrode (UME), in an aqueous solution. An immiscible solvent (with respect to water), containing the analyte of interest, is passed out of the capillary, forming a droplet which expands towards the UME, operated in amperometric or potentiometric modes. Through measurement of the current (in amperometric mode) and the droplet electrode distance via a video camera, it is possible to calculate both partitioning of the analyte between the solvents and the kinetics of interfacial transfer. A typical experimental setup is shown in Figure 5.18. Future work would look to implement MEMED as a screening technique for useful liquid-liquid / analyte extraction systems.

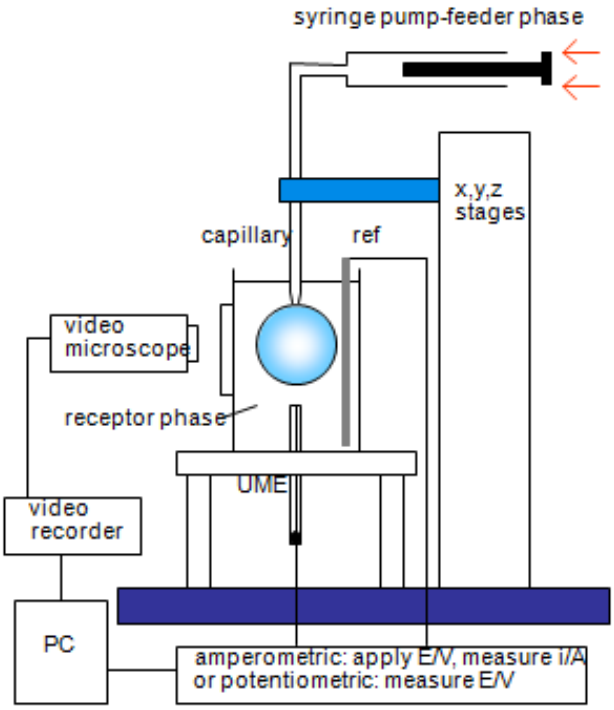

Figure 5.18: Schematic of the experimental setup for MEMED, with a droplet phase denser than the receptor phase.[59]

5.3 Conclusions

In this work we have demonstrated for the first time an electrochemical approach for the quantitation of a GI (HZ) in the presence of excess API (ACM) in aqueous solvents, which is of key interest to the pharmaceutical industry. This approach paves the way for on-line analysis in both aqueous and organic solvents, as extraction or derivatization procedures which take place off-line, are no longer required. The experimental flow system allows for FIA-EC detection of species with minimal dispersion of the analyte in the carrier stream. The two part cell, with the bottom component comprising a co-planar BDD microband electrode, insulated in insulating diamond platform is also easy to assemble and disassemble repeatedly. Moreover, the diamond based substrate means the electrode never changes its geometry through repeated use.

Using metal NP BDD electrodes, which offer higher signal to noise ratios that metal electrodes, it is also possible to resolve the electrochemical signatures for the HZ and the

ACM simply through choice of the most appropriate metal (Pt was found appropriate in this study); this is not possible using BDD alone. It was also shown that the Pt NPs were stable under the flow conditions used herein, over the timescale of typical experiments, when electrochemically deposited onto a ~ nm flat BDD microcrystalline surface. No evidence of NP detachment was observed using either FE-SEM or adsorption/desorption of hydrogen electrochemistry. The proposed approach allows HZ detection down to sub-ppm levels with respect to the API in accordance with pharmaceutical guidelines and represents a fast, cost effective alternative to current methods for GI detection in the pharmaceutical industry.

Finally, subsequent areas of study are proposed to expand on this work and demonstrate detection in non-aqueous solvents, including a proof of concept study of on-line LLE of HZ from paraffin oil via droplet-microfluidics.

5.4 References

(1) Teasdale, A. *Genotoxic Impurities Stratagies for Identification and Control*; John Wiley & Sons: New Jersey, 2010, p 428.

(2) Robinson, D. I. *Org. Process Res. Dev.* **2010**, *14*, 946-959.

(3) Müller, L.; Mauthe, R. J.; Riley, C. M.; Andino, M. M.; Antonis, D. D.; Beels, C.; DeGeorge, J.; De Knaep, A. G. M.; Ellison, D.; Fagerland, J. A.; Frank, R.; Fritschel, B.; Galloway, S.; Harpur, E.; Humfrey, C. D. N.; Jacks, A. S.; Jagota, N.; Mackinnon, J.; Mohan, G.; Ness, D. K.; O'Donovan, M. R.; Smith, M. D.; Vudathala, G.; Yotti, L. *Regul. Toxicol. Pharmacol.* **2006**, *44*, 198-211.

(4) Elder, D. P.; Snodin, D.; Teasdale, A. *J. Pharm. Biomed. Anal.* **2011**, *54*, 900-910.

(5) Sun, M. J.; Bai, L.; Liu, D. Q. *J. Pharm. Biomed. Anal.* **2009**, *49*, 529-533.

(6) Kean, T.; Miller, J. H. M.; Skellern, G. C.; Snodin, D. *Pharmeuropa scientific notes* **2006**, *2*, 23-33.

(7) Gyllenhaal, O.; Grönberg, L.; Vessman, J. *J. Chromatogr. A* **1990**, *511*, 303-315.

(8) Matsui, F.; Robertson, D. L.; Lovering, E. G. *J. Pharm. Sci.* **1983**, *72*, 948-951.

(9) Bitziou, E.; Joseph, M. B.; Read, T. L.; Palmer, N.; Mollart, T.; Newton, M. E.; Macpherson, J. V. *Anal Chem* **2014**, *86*, 10834-10840.

(10) Santos, J. R.; Rangel, A. O. S. S. *Food Chemistry* **2015**, *187*, 152-158.

(11) Lewis, G. E. M.; Gross, A. J.; Kasprzyk-Hordern, B.; Lubben, A. T.; Marken, F. *Electrophoresis* **2015**, *36*, 1866-1871.

(12) Švorc, Ľ.; Kalcher, K. *Sensors and Actuators B: Chemical* **2014**, *205*, 215-218.

(13) Hamblin, D. N.; Qiu, J.; Haubold, L.; Swain, G. M. *Analytical Methods* **2015**, *7*, 4481-4485.

(14) dos Santos, V. B.; Fava, E. L.; Pessoa-Neto, O. D.; Bianchi, S. R.; Faria, R. C.; Fatibello, O. *Analytical Methods* **2014**, *6*, 8526-8534.

(15) Sun, H.; Dong, L.; Yu, H.; Huo, M. *Russ. J. Electrochem.* **2013**, *49*, 883-887.

(16) Miller, J. N.; Miller, J. C. *Statistics and Chemometrics for Analytical Chemistry*, 5th ed.; Pearson Education Limited: London, 2005.

(17) Kleijn, S. E. F.; Lai, S. C. S.; Koper, M. T. M.; Unwin, P. R. *Angew. Chem., Int. Ed.* **2014**, *53*, 3558-3586.

(18) Wang, J.; Swain, G. M. *J. Electrochem. Soc.* **2003**, *150*, E24-E32.

(19) Hutton, L.; Newton, M. E.; Unwin, P. R.; Macpherson, J. V. *Anal. Chem.* **2009**, *81*, 1023-1032.

(20) Biegler, T.; Rand, D. A. J.; Woods, R. *Journal of Electroanalytical Chemistry and Interfacial Electrochemistry* **1971**, *29*, 269-277.

(21) Hu, J.; Lu, X.; Foord, J. S. *Electrochem. Commun.* **2010**, *12*, 676-679.

(22) Janssen, G.; van Enckevort, W. J. P.; Vollenberg, W.; Giling, L. J. *Diamond Relat. Mater.* **1992**, *1*, 789-800.

(23) Aldous, L.; Compton, R. G. *Phys Chem Chem Phys* **2011**, *13*, 5279-5287.

(24) Dias, F. X.; Jaselskis, B. *Analyst* **1983**, *108*, 76-80.

(25) Jannakoudakis, A. D.; Kokkinidis, G. *J. Electroanal. Chem. Interfacial Electrochem.* **1982**, *134*, 311-324.

(26) Nishihara, C.; Raspini, I. A.; Kondoh, H.; Shindo, H.; Kaise, M.; Nozoye, H. *J. Electroanal. Chem.* **1992**, *338*, 299-316.

(27) Bard, A. J. *Anal. Chem.* **1963**, *35*, 1602-1607.

(28) Golabi, S. M.; Zare, H. R. *Electroanal* **1999**, *11*, 1293-1300.

(29) Lin, C. Y.; Coote, M. L.; Gennaro, A.; Matyjaszewski, K. *J Am Chem Soc* **2008**, *130*, 12762-12774.

(30) Senboku, H.; Takahashi, M.; Fukuhara, T.; Hara, S. *Chemistry Letters* **2007**, *36*, 228-229.

(31) Nikitin, O. M.; Magdesieva, T. V. *Mendeleev Communications* **2011**, *21*, 194-195.

(32) Collyer, S. D.; Bradbury, S.; Davis, F.; Hatfield, J. V.; Stirling, C. J. M.; Higson, S. P. J. *Electroanal* **2004**, *16*, 324-327.

(33) Ratiu, C.; Lazau, C.; Orha, C.; Grozescu, I.; Pop, A.; Sonea, D.; Manea, F.; Burtica, G.; Schoonman, J. *Environ. Eng. Manag. J.* **2009**, *8*, 825-830.

(34) Marzuki, N. I.; Abu Bakar, F.; Salleh, A.; Heng, L. Y.; Yusof, N. A.; Siddiquee, S. *Int J Electrochem Sc* **2012**, *7*, 6070-6083.

(35) Avci, A.; Şirin, K. *Journal of Macromolecular Science, Part A* **2014**, *51*, 488-498.

(36) Kolzunova, L. G.; Kovarskii, N. Y.; Novichkova, L. M. *Vysokomolekulyarnye Soedineniya Seriya A* **1985**, *27*, 2370-2375.

(37) Arduini, F.; Scognamiglio, V.; Covaia, C.; Amine, A.; Moscone, D.; Palleschi, G. *Sensors* **2015**, *15*, 4353-4367.

(38) Ozkan, S. A. *Electroanalytical Methods in Pharmaceutical Analysis and Their Validation*; HNB publishing: New York, USA, 2012, p 350.

(39) Gupta, V. K.; Jain, R.; Radhapyari, K.; Jadon, N.; Agarwal, S. *Anal. Biochem.* **2011**, *408*, 179-196.

(40) Farghali, R. A.; Ahmed, R. A. *Int J Electrochem Sc* **2012**, *7*, 13008-13019.

(41) Uslu, B.; Dogan, B.; Ozkan, S. A.; Aboul-Enein, H. Y. *Anal. Chim. Acta* **2005**, *552*, 127-134.

(42) Aravagiri, M.; Marder, S. R.; Vanputten, T.; Marshall, B. D. *J. Chromatogr. B-Biomed. Appl.* **1994**, *656*, 373-381.

(43) Golcu, A.; Dogan, B.; Ozkan, S. A. *Anal. Lett.* **2005**, *38*, 1913-1931.

(44) Ammida, N. H. S.; Volpe, G.; Draisci, R.; delli Quadri, F.; Palleschi, L.; Palleschi, G. *Analyst* **2004**, *129*, 15-19.

(45) Šelešovská, R.; Janíková-Bandžuchová, L.; Chýlková, J. *Electroanal* **2014**, n/a-n/a.

(46) Shahrokhian, S.; Amiri, M. *Microchim Acta* **2007**, *157*, 149-158.

(47) Carlin, A.; Gregory, N.; Simmons, J. *J. Pharm. Biomed. Anal.* **1998**, *17*, 885-890.

(48) Cao, X. Q.; Wang, B. C.; Su, Q. *J. Electroanal. Chem.* **1993**, *361*, 211-214.

(49) Michlmayr, M.; Sawyer, D. T. *J. Electroanal. Chem.* **1969**, *23*, 375-385.

(50) Antoniadou, S.; Jannakoudakis, A. D.; Theodoridou, E. *Synth. Met.* **1989**, *30*, 295-304.

(51) MacDonald, S. M.; Watkins, J. D.; Bull, S. D.; Davies, I. R.; Gu, Y.; Yunus, K.; Fisher, A. C.; Page, P. C. B.; Chan, Y.; Elliott, C.; Marken, F. *Journal of Physical Organic Chemistry* **2009**, *22*, 52-58.

(52) Watkins, J. D.; MacDonald, S. M.; Fordred, P. S.; Bull, S. D.; Gu, Y.; Yunus, K.; Fisher, A. C.; Bulman-Page, P. C.; Marken, F. *Electrochim Acta* **2009**, *54*, 6908-6912.

(53) Kaluza, D.; Adamiak, W.; Kalwarczyk, T.; Sozanski, K.; Opallo, M.; Jönsson-Niedziolka, M. *Langmuir* **2013**, *29*, 16034-16039.

(54) Ralf, S.; Martin, B.; Thomas, P.; Stephan, H. *Reports on Progress in Physics* **2012**, *75*, 016601.

(55) Teh, S.-Y.; Lin, R.; Hung, L.-H.; Lee, A. P. *Lab Chip* **2008**, *8*, 198-220.

(56) Rogers, M.; Leong, C.; Niu, X. Z.; de Mello, A.; Parker, K. H.; Boutelle, M. G. *Phys Chem Chem Phys* **2011**, *13*, 5298-5303.

(57) Garstecki, P.; Fuerstman, M. J.; Stone, H. A.; Whitesides, G. M. *Lab Chip* **2006**, *6*, 437-446.

(58) Song, H.; Chen, D. L.; Ismagilov, R. F. *Angewandte Chemie International Edition* **2006**, *45*, 7336-7356.

(59) Slevin, C. J.; Unwin, P. R. *Langmuir* **1999**, *15*, 7361-7371.

(60) Zhang, J.; Unwin, P. R. *Phys Chem Chem Phys* **2000**, *2*, 1267-1271.

(61) Zhang, J.; Atherton, J. H.; Unwin, P. R. *Langmuir* **2004**, *20*, 1864-1870.

Chapter 6 Conclusions

The quantification of trace levels of genotoxic impurities (GIs) in the presence of active pharmaceutical ingredients (APIs) is of critical importance in the pharmaceutical industry to uphold drug quality and safety.[1] This is complicated by the wide range of GIs, varied GI-API systems and varied solvents/matrices available, reflected in the wide range of techniques applied for their determination.[2] Investigations herein have focussed on hydrazine, a particularly challenging GI[3] often quantified off-line, involving extraction or derivatization procedures in order to quantify it at the required safe limits, in the presence of an excess of an API.[2]

Work in this thesis has attempted to overcome these challenges through various electrochemical analysis methodologies. Initial work in chapter 3 demonstrates the quantification of hydrazine (HZ) in the presence of two electrochemically active APIs; acetaminophen (ACM) and promazine (PZ). Au and Pt nanoparticle (NP) functionalised boron doped diamond (BDD) were investigated as electrode materials and the electrodes were characterised by atomic force microscopy. Linear sweep voltammetry and differential pulse voltammetry were used for HZ determination and it was shown that the API signal can be effectively "screened out" from the much smaller GI signal, by simply changing the chemical identity of the metal NP on the BDD electrode. This results in a shifting of the overpotential of the GI-HZ. However, the detection limits from these methods (2352 and 693 ppm), in the presence of an API (1 mM PZ ACm and PZ respectively), did not achieve the safe levels for GI determination (1 ppm).[4]

A hydrodynamic approach was next adopted to move towards on-line detection and reach the stipulated safe limits. A new flow injection analysis (FIA) system was

developed based on both an inlaid all diamond BDD microband electrode and an optimised flow cell as discussed in chapter 4. The all-diamond device represents a durable, long lasting co-planar electrode which simplifies characterisation and reduces the occurrence of leaks in the flow cell. The microstereolithographically fabricated flow cell was designed to avoid dispersion and dead volumes in the FIA manifold and was first characterised prior to use through continuous flow cyclic voltammetry (CV) and FIA. The electrochemical responses were analysed numerically and against various models of dispersion to assess the flow dynamics in the system. The employed FIA-EC cell was shown to give smaller dispersion, reduced dead volumes, higher sampling frequency and smaller sample requirement compared to previous employed FIA systems.

3D finite element modelling of this FIA system is currently in progress, in order to investigate the effect of dead volumes and dispersion on the FIA-EC response. This work is important as the vast majority of dispersion models do not apply to the hydrodynamics of many FIA systems.[5] This means commonly used dispersion variables such as the dispersion coefficient (D_c) and the residence time (t_r) do not offer a complete description of dispersion. Furthermore, very few studies consider the effect of dead volumes (a critical factor in FIA systems) on the FIA response[6]

The developed FIA-EC system was employed for the trace detection of HZ in the presence of an excess of ACM (50 mM) as discussed in chapter 5. The all-diamond microband electrode was functionalised with Pt NP and the NP stability investigated via field emission scanning electron microscopy (FE-SEM) and CV. No evidence of NP detachment was observed using either FE-SEM or adsorption/desorption of hydrogen electrochemistry from cyclic voltammetry. The proposed approach yielded HZ detection down to sub-ppm levels (0.274 ppm) with respect to the API, in accordance with

pharmaceutical guidelines. This approach represents a fast, cost effective alternative to current methods for GI detection in the pharmaceutical industry.

Finally, subsequent areas of study are proposed to expand on this work and demonstrate detection in non-aqueous solvents. Detection in non-aqueous solvents is examined through testing of the solvent compatibility of the flow cells utilised in chapters 4 and 5, with promising results. Also, detection via droplet microfluidics is discussed, proposing an on-line liquid-liquid extraction from a droplet of organic solvent to an aqueous stream in flow. These investigations represent exciting possibilities for future work in the field of electrochemical analysis of pharmaceuticals.

6.1 References

(1) Robinson, D. I. *Org. Process Res. Dev.* **2010**, *14*, 946-959.
(2) Teasdale, A. *Genotoxic Impurities Stratagies for Identification and Control*; John Wiley & Sons: New Jersey, 2010, p 428.
(3) Elder, D. P.; Snodin, D.; Teasdale, A. *J. Pharm. Biomed. Anal.* **2011**, *54*, 900-910.
(4) Müller, L.; Mauthe, R. J.; Riley, C. M.; Andino, M. M.; Antonis, D. D.; Beels, C.; DeGeorge, J.; De Knaep, A. G. M.; Ellison, D.; Fagerland, J. A.; Frank, R.; Fritschel, B.; Galloway, S.; Harpur, E.; Humfrey, C. D. N.; Jacks, A. S.; Jagota, N.; Mackinnon, J.; Mohan, G.; Ness, D. K.; O'Donovan, M. R.; Smith, M. D.; Vudathala, G.; Yotti, L. *Regul. Toxicol. Pharmacol.* **2006**, *44*, 198-211.
(5) Vanderslice, J. T.; Stewart, K. K.; Rosenfeld, A. G.; Higgs, D. J. *Talanta* **1981**, *28*, 11-18.
(6) Pike, D.; Kapur, N.; Millner, P.; Stewart, D. *Sensors* **2012**, *13*, 58.